

UC San Diego

UC San Diego Electronic Theses and Dissertations

Title

Hyperbolic hydro-mechanical model for seismic compression prediction of unsaturated soils in the funicular regime

Permalink

<https://escholarship.org/uc/item/84g2j6tg>

Author

Kinikles, Dellena

Publication Date

2022

Peer reviewed|Thesis/dissertation

UNIVERSITY OF CALIFORNIA SAN DIEGO

Hyperbolic hydro-mechanical model for seismic compression prediction of unsaturated soils in
the funicular regime

A thesis submitted in partial satisfaction of the requirements for the degree
Master of Science

in

Geotechnical Engineering

by

Dellena Kinikles

Committee in charge:

Professor John Scott McCartney, Chair
Professor Tara Hutchinson
Professor Ingrid Tomac

2022

Copyright

Dellena Kinikles, 2022

All rights reserved.

The thesis of Dellena Kinikles is approved, and it is acceptable in quality and form for publication on microfilm and electronically.

University of California San Diego

2022

iii

DEDICATION

To my loving family, thank you for always supporting my dreams.

TABLE OF CONTENTS

THESIS APPROVAL PAGE	iii
DEDICATION	iv
TABLE OF CONTENTS	v
LIST OF FIGURES	viii
LIST OF TABLES	xv
LIST OF SYMBOLS	xvi
ACKNOWLEDGEMENTS.....	xix
ABSTRACT OF THE THESIS	xx
1 Introduction.....	1
1.1 Research Motivation	1
1.2 Research Objectives	3
1.3 Research Approach	4
1.4 Thesis Organization	5
2 Background	7
2.1 Introduction to Unsaturated Soils	7
2.2 Effective Stress in Unsaturated Soils	10
2.3 Cyclic Response of Soils	15
2.4 Seismic Compression of Unsaturated Soils in Literature	20
3 Model	24
3.1 Stresses and Strains during Cyclic Simple Shear Testing.....	24
3.2 Prediction of the Volumetric Strain during Cyclic Shearing	28
3.3 Changes in Degree of Saturation during Undrained Shearing.....	34

3.4 Estimation of Changes in Pore Air Pressure during Undrained Shearing.....	35
3.5 Estimation of Changes in Pore Water Pressure during Undrained Shearing	36
3.6 Calculation of Effective Stress Changes during Cyclic Shearing	38
3.7 Predicting the Evolution in Hydro-Mechanical Variables during Undrained Shearing .	38
4 Data.....	40
4.1 Sand Specimen.....	40
4.2 Drained Monotonic Simple Shear Data	43
4.3 Undrained Cyclic Simple Shear Data.....	44
5 Model Calibration....	58
5.1 Calibration of Backbone Curve from Drained Shearing of Unsaturated Sand.....	58
5.2 Calibration of Pore Water Pressure Generation Model.....	61
6 Analysis.....	67
6.1 Evolution in Hydro-Mechanical Variables during Undrained Cyclic Shearing.....	67
6.2 Evaluation of the Effects of Initial Degree of Saturation on Seismic Compression.....	69
6.3 Evaluation of Reasons behind Discrepancy between Model and Experiments.....	74
6.3.1 Pore Air Generation.....	74
6.3.2 Pore Water Generation.....	76
7 Conclusions.....	79
8 Recommendations for Future Research.....	81
Appendix.....	82
A1. Hyperbolic Fitting for Cyclic Shearing.....	82
A2: Pore Air Pressure Derivation	84
A3: Relationship between Degree of Saturation and Volumetric Strain.....	92

A4: Transient Scanning Curve Equation 94
A5: Volume Compression Equations 94
A6: Graphical Results of Model for all Specimens..... 97
References..... 102

LIST OF FIGURES

Figure 2.1.1 Typical near-surface unsaturated soil profile with hydrostatic conditions (after Lu and Likos 2004).	8
Figure 2.1.2 Typical shape of the soil-water retention curve partitioned into the capillary, funicular and pendular regimes (after Lu and Likos 2004).	9
Figure 2.2.1 Schematic of a hysteretic SWRC showing typical shapes of the primary drying and wetting paths in blue and orange, respectively.	13
Figure 2.2.2 SSCCs representative of sands, silts, and clays (Lu et al. 2010)	15
Figure 2.3.1 Example of a hyperbolic shear stress-shear strain curve with a definition of the small strain shear modulus G_i	16
Figure 2.3.2 Example of a shear modulus reduction curve	17
Figure 2.3.3 Example of shear stress-strain hysteresis of soils during loading, unloading and reloading (Hardin and Drnevich 1972)	20
Figure 2.3.4 Comparison between seismic compression results from centrifuge tests and the empirical model of Ghayoomi et al. (2013)	21
Figure 3.1.1 Key variables in a cyclic simple shear test on a soil specimen after vertical loading and during bi-directional cyclic simple shearing	24
Figure 3.1.2 Schematic of the changes in stress state during cyclic simple shear testing of a soil specimen showing the directions of the stresses during applied shear strain testing	25
Figure 3.1.3 Backbone curve shape from the hyperbolic model: (a) Shear stress-strain curve; (b) Shear stress ratio-shear strain curve	26

Figure 3.1.4 Hysteretic loop showing the hyperbolic shear stress strain reversals along with the hyperbolic backbone curve.	28
Figure 3.2.1 Schematic of soil particle rearrangement before and after cyclic shearing showing initial and final heights of specimen and changes in degree of saturation.	29
Figure 3.2.2 UBCSAND model hyperbolic stress-strain relationship (Byrne and Park 2003)	30
Figure 3.2.3 Hysteretic shear stress-shear strain showing plastic load/reload and elastic unload, with the corresponding plastic/elastic cyclic shear strain and cumulative plastic volumetric strain	33
Figure 3.5.1 Schematic of the transient scanning path of the SWRC for a sand specimen initially on the primary drying path.	37
Figure 3.7.1 Flow chart for the semi-empirical hyperbolic model with hydro-mechanical coupling for seismic compression in the funicular regime	39
Figure 4.1.1 Particle size distribution curve for the SW sand (Rong and McCartney 2020b).	40
Figure 4.1.2 SWRC for the sand specimen at $D_r = 0.45$ (Rong and McCartney 2020b)	41
Figure 4.1.3 Schematic view of the specimen housing in the modified NGI simple shear device used for drained and undrained experiments (dimensions in mm) (Rong and McCartney 2021a).	42
Figure 4.2.1 Backbone curves for drained sand ($D_r = 0.45$) at various constant suctions (4 kPa, 6 kPa, 10 kPa) and different shear strain amplitudes (1%, 3%) (Rong and McCartney 2020a)	44

- Figure 4.3.1 Data Set 1 $S_o=0.56$ Time series of (a) Shear strain (b) shear stress (c) Degree of saturation (d) Volume change (e) Pore air pressure change (f) Pore water pressure change (g) Matric suction change (h) Mean effective stress change (i) Cyclic shear stress and cyclic shear strain 46
- Figure 4.3.2 Data Set 2 $S_o=0.56$ Time series of (a) Shear strain (b) shear stress (c) Degree of saturation (d) Volume change (e) Pore air pressure change (f) Pore water pressure change (g) Matric suction change (h) Mean effective stress change (i) Cyclic shear stress and cyclic shear strain 47
- Figure 4.3.3 Data Set 1 $S_o=0.4$ Time series of (a) Shear strain (b) shear stress (c) Degree of saturation (d) Volume change (e) Pore air pressure change (f) Pore water pressure change (g) Matric suction change (h) Mean effective stress change (i) Cyclic shear stress and cyclic shear strain 48
- Figure 4.3.4 Data Set 2 $S_o=0.4$ Time series of (a) Shear strain (b) shear stress (c) Degree of saturation (d) Volume change (e) Pore air pressure change (f) Pore water pressure change (g) Matric suction change (h) Mean effective stress change (i) Cyclic shear stress and cyclic shear strain 49
- Figure 4.3.5 Data Set 1 $S_o=0.3$ Time series of (a) Shear strain (b) shear stress (c) Degree of saturation (d) Volume change (e) Pore air pressure change (f) Pore water pressure change (g) Matric suction change (h) Mean effective stress change (i) Cyclic shear stress and cyclic shear strain 50
- Figure 4.3.6 Data Set 2 $S_o=0.3$ Time series of (a) Shear strain (b) shear stress (c) Degree of saturation (d) Volume change (e) Pore air pressure change (f) Pore water

	pressure change (g) Matric suction change (h) Mean effective stress change (i) Cyclic shear stress and cyclic shear strain	
Figure 4.3.7 Data Set 1* $S_o=0.2$	Time series of (a) Shear strain (b) shear stress (c) Degree of saturation (d) Volume change (e) Pore air pressure change (f) Pore water pressure change (g) Matric suction change (h) Mean effective stress change (i) Cyclic shear stress and cyclic shear strain	52
Figure 4.3.8 Data Set 2 $S_o=0.2$	Time series of (a) Shear strain (b) shear stress (c) Degree of saturation (d) Volume change (e) Pore air pressure change (f) Pore water pressure change (g) Matric suction change (h) Mean effective stress change (i) Cyclic shear stress and cyclic shear strain	53
Figure 4.3.9 Data Set 1 $S_o=0.118$	Time series of (a) Shear strain (b) shear stress (c) Degree of saturation (d) Volume change (e) Pore air pressure change (f) Pore water pressure change (g) Matric suction change (h) Mean effective stress change (i) Cyclic shear stress and cyclic shear strain	54
Figure 4.3.10 Data Set 2 $S_o=0.117$	Time series of (a) Shear strain (b) shear stress (c) Degree of saturation (d) Volume change (e) Pore air pressure change (f) Pore water pressure change (g) Matric suction change (h) Mean effective stress change (i) Cyclic shear stress and cyclic shear strain	55
Figure 4.3.11 Data Set 1* $S_o=0$ DRY	(a) Shear strain time series (b) shear stress time series (c) Volume change time series (d) Pore air pressure change time series (e) Mean effective stress change time series (f) Cyclic shear stress and cyclic shear strain time series	56

Figure 4.3.12 Data Set 2* $S_0=0$ DRY (a) Shear strain time series (b) shear stress time series (c) Volume change time series (d) Pore air pressure change time series (e) Mean effective stress change time series (f) Cyclic shear stress and cyclic shear strain time series	57
Figure 5.1.1 Linear transformation of hyperbolic shear stress-strain relationship	58
Figure 5.1.2 Hyperbolic fitting of drained CSS data at 1% shear strain: (a) Monotonic loading at 1% shear strain (b) Linearization of curve to find hyperbolic parameters	59
Figure 5.1.3 Hyperbolic fitting of drained CSS data at 3% shear strain: (a) Monotonic loading at 3% shear strain; (b) Linearization of curve to find hyperbolic parameters	60
Figure 5.1.4 Comparison of the calibrated backbone and hysteretic shear stress-strain curves with the experimental data for $S_0 = 0.3$ and $\sigma_v = 50$ kPa from Rong and McCartney (2020a)	61
Figure 5.2.1 Transient SWRC wetting paths of undrained cyclic shear data set 1 after 200 cycles.	62
Figure 5.2.2 Slopes of transient SWRC wetting paths of data after 1.25 cycles of undrained cyclic simple shear.	64
Figure 5.2.3 (a) Slopes of the transient SWRC scanning curve with averages at 1.25 cycles and 200 cycles (b) Empirical prediction of the slope of the transient SWRC scanning curve with degree of saturation in the funicular regime for 200 cycles	66
Figure 6.1.1 Comparison between cyclic simple shear results for a specimen with $S_0 = 0.3$ and model results after 200 cycles: (a) Volume compression (b) Mean	68

effective stress changes (c) Pore air pressure (d) Pore water pressure (e) Suction stress (f) Transient scanning path	
Figure 6.2.1 Data Set 1 vs. Model: (a) Volume vs. Cycles; (b) Model: Volume vs. Cycles; (c) Matric suction vs. Cycles; (d) Saturation vs. Cycles; (e) Data: Mean Stress vs. Cycle; (f) Model: Mean Stress vs. Cycle	70
Figure 6.2.2 Comparison of trends between key hydro-mechanical variables after 15 cycles of undrained cyclic shearing and the initial degree of saturation obtained from the experiments of Rong and McCartney (2020b) and the model: (a) $\Delta\psi$ vs. S_o ; (b) Δu_a vs. S_o ; (c) Δu_w vs. S_o ; (d) ΔV vs. S_o ; (e) $\Delta\sigma'_m$ vs. S_o	72
Figure 6.2.3 Comparison between the model predictions and experimental results after 200 cycles of undrained shearing: (a) $\Delta\psi$ vs. S_o (b) Δu_a vs. S_o (c) Δu_w vs. S_o (d) ΔV vs. S_o (e) $\Delta\sigma'_m$ vs. S_o	73
Figure 6.2.4 Transient SWRC scanning paths and predict transient SWRC paths from the model and experimental results from Data set 1.	74
Figure 6.3.1.1 Model's prediction of pore air pressure generation by initial saturation at (a) 15 cycles (b) 200 cycles	75
Figure 6.3.2.1 Variation in results between Data Set 1 transient SWRC: (a) $S=0.3$ $\psi=4$ kPa model calibrated to 1.25 cycles b) $S=0.3$ $\psi=4$ kPa model calibrated to 200 cycles.	78
Figure 6.3.2.2 Variation in results between Data Set 1 matric suction vs. N cycles (a) $S=0.3$ $\psi=4$ kPa model calibrated to 1.25 cycles, (b) $S=0.3$ $\psi=4$ kPa model calibrated to 200 cycles	78

Figure 8.1 Shear stress-shear strain undrained Data Set 2: $\psi_o = 6kPa, S_o = 0.2$ at 1% applied cyclic shear strain 81

LIST OF TABLES

Table 1: Summary of initial testing conditions and final shear strain	44
Table 2: Summary of initial conditions of undrained cyclic simple shear experiments of Rong and McCartney (2020) that were modeled in this study	45
Table 3: Summary of initial testing conditions and final shear strain for the undrained cyclic simple shear experiments (after Rong and McCartney 2020b).	45
Table 4: Calibrated hyperbolic model parameters for drained tests to 1% and 3% shear strain	60
Table 5: Initial conditions of saturation and matric suction from the undrained CSS data set.	63
Table 6: Initial conditions of the saturation, matric suction, and average slope for the transient SWRC rewetting path of the undrained data.	64
Table 7: Averaged transient SWRC slope over entire 200 cycles of undrained CSS data for funicular regime saturations.	65
Table 8: Predicted transient SWRC slope of undrained CSS data set 01 for funicular regime saturations.	66

LIST OF SYMBOLS

τ	Shear stress
τ_{ult}	Ultimate shear stress
τ_f	Failure shear stress
τ_c	Maximum applied cyclic shear stress
η_d	Developed stress ratio
σ_v	Vertical total stress
σ_v'	Vertical effective stress
σ_m	Mean stress
σ_m'	Mean effective stress
σ_s	Suction stress
e	Void ratio
S	Degree of saturation
S_e	Effective degree of saturation
ψ	Matric suction
D_r	Relative density
u_a	Pore air pressure
u_{a0}	Initial pore air pressure
u_{af}	Final pore air pressure
u_w	Pore water pressure
α_{vG}	Inverse of air-entry pressure parameter in SWRC model of van Genuchten (1980)
N_{vG}	Pore size distribution parameter in SWRC model of van Genuchten 1980
ϕ_{cv}	Constant volume friction angle
ϕ_f	Peak friction angle
η_f	Failure stress ratio
ψ	Dilation angle
ϕ_d	Developed friction angle
ν	Poisson's ratio

G_i	Elastic shear modulus
K^e_G	Elastic bulk modulus
n_e	Shear modulus exponent
G_i^P	Initial plastic shear modulus
G_p	Plastic shear modulus
γ_e	Elastic shear strain
γ_p	Plastic shear strain
γ	Total shear strain
γ_c	Maximum applied cyclic shear strain
γ_{applied}	Applied shear strain
ε_v^e	Elastic volumetric strain
ε_v^P	Plastic volumetric strain
ε_v	Total volumetric strain
P_a	Atmospheric pressure
R_f	Failure ratio
n_{ao}	Initial number of moles of air
n_{af}	Final number of moles of air
n_{ao(FA)}	Initial number of moles of air – free air
n_{ao(DA)}	Initial number of moles of air – dissolved air
h	Henry's Constant
h_o	Initial height of sand specimen
Δh	Change in height of sand specimen
K_a	Bulk modulus of air
K_o	Coefficient of lateral earth pressure at rest
V_a	Volume of air
V_{ao}	Initial volume of air
V_{af}	Final volume of air
V_w	Volume of water

V_{wo}	Initial volume of water
V_{wf}	Final volume of water
V_T	Total volume of sand specimen
V_{ao}	Initial volume of air
V_{af}	Final volume of air
ρ_a	Density of air
ρ_w	Density of water
T	Temperature
SL	Stress level
b	Intercept of transient SWRC scanning path
m	Slope of transient SWRC scanning path

ACKNOWLEDGEMENTS

I would like to thank Dr. McCartney for his guidance and mentorship throughout my time as a student at UCSD. It has been an invaluable experience working on research with Dr. McCartney and I am forever grateful for the opportunity.

I would also like to thank Dr. Tomac for introducing me to the world of research in my second quarter at UCSD. If it weren't for this experience, I would not have pursued a master's thesis.

The contents of multiple chapters use experimental research from Dr. McCartney's past students. I would like to thank Dr. Wenyong Rong for his help in preparing his data for this report.

ABSTRACT OF THE THESIS

Hyperbolic hydro-mechanical model for seismic compression prediction of unsaturated soils in
the funicular regime

by

Dellena Kinikles

Master of Science in Geotechnical Engineering

University of California San Diego, 2022

Professor John Scott McCartney, Chair

A semi-empirical elasto-plastic model with a hyperbolic stress-strain curve was developed with the goal of predicting the seismic compression of unsaturated sands in the funicular regime during undrained cyclic shearing. Using a flow rule derived from energy considerations, the evolution in plastic volumetric strain (seismic compression) is predicted from the plastic shear strains of the hysteretic hyperbolic stress-strain curve. The plastic volumetric strains are used to predict the changes in degree of saturation from phase relationships and changes in pore air pressure from Boyle's and Henry's laws. The degree of saturation is used to estimate changes in matric suction from the transient scanning paths of the soil-water retention curve. Changes in small-strain shear modulus estimated from changes in mean effective stress computed from constant total stress and changes in pore air pressure, degree of saturation and matric suction, in turn affect the hyperbolic stress-strain curve's shape. The model was validated using experimental data from undrained cyclic simple shear tests on unsaturated sand specimens with different initial degrees of saturation in the funicular regime. While the model captured trends in hydromechanical variables as a function shearing cycles well, it underestimated the measured volumetric strain and degree of saturation changes at large numbers of cycles in some tests. A linear decreasing trend between seismic compression and initial degree of saturation was predicted from the model while a nonlinear increasing-decreasing trend was observed in the experiments, which may be due to not considering post-shearing reconsolidation or experimental variations in cyclic shear strain amplitudes.

1 Introduction

1.1 Research Motivation

This study is focused on contributing to the understanding of the volume change response of unsaturated soils during cyclic or seismic shearing, a phenomenon referred to as seismic compression (Stewart et al. 2004). Unsaturated soil profiles are encountered near the earth's surface in both natural and engineered settings. Natural unsaturated soil profiles are encountered when the water table is below the ground surface. The depth of the water table may vary with time due to infiltration, evaporation or groundwater flow. In addition to founding structures in natural unsaturated soil profiles, they are encountered when making cuts into the subsurface to form excavations or changes in grade. Engineered unsaturated soil profiles are encountered in fill-type geotechnical structures like embankments and retaining walls constructed above the ground surface and the water table. Although they may be affected by infiltration and evaporation, drainage systems are typically included in fill-type geotechnical structures to help ensure that they remain in unsaturated conditions. Embankments and retaining walls are encountered often in transportation infrastructures like pavements, railways, and bridge abutments to help ensure that they remain above the water table.

Unsaturated soils contain air, water, and solids. The amount of water in unsaturated soils can be represented by the degree of saturation (volume of water per volume of voids), the volumetric water content (volume of water per total volume), or the gravimetric water content (mass of water per mass of solids). These variables can be used interchangeably and are related through phase relationships. The energy state in the pore water of unsaturated soils with respect to free water is typically represented by the matric suction, which is equal to the difference between the pore water and air pressures in the soil. A difference between the pore water and air pressures

forms due to the curvature of the air-water interface (referred to as a meniscus) associated with the surface tension of water and the water-solid contact angle. The degree of saturation, matric suction, and pore air pressure are important variables that can have effects on the effective stress in the unsaturated soil profile. The shear strength and stiffness of the unsaturated soil are both closely tied with the effective stress, indicating that the mechanical response of the unsaturated soil profile is coupled with the hydraulic conditions in the soil.

During cyclic or seismic shearing of unsaturated soils, rearrangement of soil particles may occur, leading to a reduction in total volume of the soil as the particles rearrange into a tighter arrangement and the void space is decreased (Youd 1972; Rong and McCartney 2020a, 2020b). Although it is well known that loose soils contract and dense soils dilate during monotonic shearing, both loose and dense sands will experience seismic compression during cyclic or seismic shearing (Youd 1972). Drainage conditions for the pore fluids in a soil is known to have a major effect on the seismic shearing response. The pore air and water pressures may change during this process during undrained shearing, which may occur in a soil layer with no drainage boundaries or when the rate of shearing is faster than the rate of pore fluid drainage (Okamura and Soga 2006; Unno et al. 2008; Okamura and Noguchi 2009; Rong and McCartney 2020b). Regardless of the drainage conditions, the degree of saturation is expected to increase as the volume of voids decreases (Rong and McCartney 2020a, 2020b). The changes in pore fluid pressures and degree of saturation will lead to changes in the effective stress state in the soil, which controls the shear strength and stiffness of the soil. In engineered unsaturated soil profiles in particular, it is imperative to understand the changes in volume for soils having different initial degrees of saturation because changes in volume and associated changes in hydro-mechanical variables will result in settlements of the soil layer and a reduction in effective stress. Settlements and changes

in effective stress may have significant impacts on the performance of overlying structures supported by the unsaturated soil layer.

Seismic compression is defined as the accrual of permanent contractive volumetric strains in soils during earthquakes and has been recognized as a major cause of seismically-induced damage in earth structures (Stewart et al. 2001, 2004). A report on the effects of the Northridge earthquake by Stewart et al. (1995) found that seismic compression of fills caused damages on the order of \$50,000 to \$100,000 per lot over 2,000 sites. Seismic compression has been recognized as a major cause of seismically induced damage in earth structures. Konagai et al. (2013) reported surface settlement of fill soils along the northeastern shorelines of Tokyo Bay during the 2011 Tohoku earthquake. Surface settlements measured at locations 12-20 m away from the pile were 300-400 mm and gradually increased to approximately 870 mm alongside the base wall. It was verified that the backfill, which primarily experienced seismic compression, was in unsaturated state as the ground water level was found to be at a depth of 25 m. Although backfill soils in fill-type geotechnical structures are typically in an initially dense state and are expected to have minimal settlement under static or traffic loading, they may still experience volumetric contraction during earthquakes. Even small backfill settlements can have a negative impact on the functionality of transportation systems and can lead to high repair costs. Accordingly, it is critical to have a constitutive model that can be used to predict the seismic compression of unsaturated soils and consider the hydro-mechanical coupling mentioned in the previous paragraph.

1.2 Research Objectives

The current state of the practice in prediction of seismic compression during earthquakes is to empirically relate vertical strain profiles with depth to the shear strain induced in a soil layer as part of a site response analysis (Yee and Stewart 2011). This is a practical approach as it builds

upon analyses performed for the earthquake site response but does not necessarily consider hydro-mechanically coupling observed in laboratory experiments. While complex elasto-plastic models have been developed to simulate the cyclic response of unsaturated soils, many do not consider hydro-mechanical coupling (e.g., Khalili et al. 2005). Alternatively, empirical models have been developed to predict the seismic compression of unsaturated soils by separately considering collapse of air voids and post-shaking reconsolidation (e.g., Ghayoomi et al. 2013; Ghayoomi and McCartney 2016). However, it can be difficult to objectively define the parameters for these models. Accordingly, based on this gap in the literature, the objective of this study is to develop a constitutive model that can represent the hydro-mechanical coupling expected in unsaturated soils undergoing seismic compression during cyclic or seismic shearing. This constitutive model is intended to be simple so that properties can be calibrated with non-specialized laboratory tests and to facilitate implementation into software packages typically used to perform geotechnical earthquake engineering simulations (OpenSees, FLAC, etc.).

1.3 Research Approach

The research approach in this thesis is to develop a semi-empirical constitutive model that links the plastic volume changes during undrained cyclic shearing of an unsaturated soil to the changes in degree of saturation and pore fluid pressures, then use these to update the effective stress and shear modulus that control the further evolution in plastic volume changes. Specifically, an elasto-plastic model with a hyperbolic stress-strain curve is used to capture the hysteretic response of the soil to cyclic shearing, and a flow rule derived from energy considerations is used to predict the evolution in plastic volumetric strain. The plastic volumetric strains are then used to estimate changes in pore air pressure from Boyle's Law, the Ideal Gas Law and Henry's Law during undrained cyclic simple shear. Assuming undrained conditions, the degree of saturation

calculated from the plastic volumetric strain is also used to estimate changes in matric suction using the transient scanning curves of the soil-water retention curve for the soil. Changes in the small-strain shear modulus of the soil are then estimated using the mean effective stress computed from the constant total stress and the varying pore air pressure, degree of saturation and matric suction. The parameters of the elasto-plastic model were calibrated from triaxial tests on dry sand and the backbone curve from a cyclic simple shear test. The model was then validated using experimental data from a series of undrained cyclic simple shear tests on unsaturated sand specimens with a relative density of 45%, a constant vertical normal stress of 50 kPa, and different initial degrees of saturation in the funicular regime.

1.4 Thesis Organization

Following this introduction, Chapter Two presents an introductory section to the mechanics of unsaturated sands. In particular, a literature review is presented to illustrate the historical understanding of unsaturated soil mechanics from inception to present day design practices. The model and results illustrate the difficulties in developing predictive earthquake designs for unsaturated sands due to the complexities in soil skeleton pore network relationships. Chapter Two also presents the different static mathematical derivations for the effective stress equation of unsaturated sands. Chapter Two includes the dynamic analysis of unsaturated sands during seismic compression in literature and derivation of a sand specimen's backbone curve. Chapter Three presents a model to predict multiple cycles of applied shear strain cyclic shearing of undrained unsaturated sand using semi-empirical equations derived from initial cycling data. Chapter Four provides a brief description of the collected drained and undrained CSS data collected from experiments performed by Rong and McCartney (2020b). Chapter Five focuses on the calibration of the model, including the hyperbolic stress-strain curve model parameters, the failure model

parameters, and the pore water pressure generation model parameters. While the pore air pressure generation model does not require soil-specific calibration as it is based solely on the predicted plastic volumetric strain and initial soil conditions, the pore water pressure generation model calibration required the definition of a slope of the transient SWRC scanning curve paths that depends on the initial degree of saturation of the sand.

A comparison between the model prediction and a set of experimental data from Rong and McCartney (2020b) is presented in Chapter 6. Specifically, this includes a comparison of the evolution of the key hydro-mechanical variables during cyclic shearing for sands having the same initial relative density of 45% with different initial degrees of saturation under a cyclic shear strain amplitude of 1% and a frequency of 1 Hz for 200 cycles. Chapter 6 also includes comparisons of the trends in the hydro-mechanical variables as a function of the initial degrees of saturation obtained after 15 and 200 cycles to demonstrate how the trends evolve with cycles. The conclusions from the model development and the observations from the comparison between the model and experiments are summarized in Chapter 7. Chapter 8 includes a summary of developments which may help improve the model predictions and recommendations to guide future experiments. This thesis also includes several appendices that include detailed derivations of key equations used in the model along with the full time series for all model results compared against the undrained cyclic simple shear data from Rong and McCartney (2020b).

2 Background

2.1 Introduction to Unsaturated Soils

In most settlement methods used in soil mechanics designs, soils are typically assumed to be in either dry or saturated conditions. This assumption is partly due to simplicity, and partly due to the belief that these two extremes in the degree of saturation (0 for dry soils and 1 for saturated soils) will yield worst-case scenarios for design as the air-water menisci in unsaturated soils will provide increased interparticle connections. A saturated soil is a two-phase system composed of soil solids with void spaces totally occupied by fluid water. A dry soil is also a two-phase system composing of a soil solid with all void spaces occupied by fluid air. Although fully saturated soils are encountered below the water table or in soils beneath lakes or oceans, it is rare to encounter fully dry soils because soil layers usually are continuously interacting with the atmosphere. In general, soils above the capillary fringe overlying the water table can be characterized as a three-phase system consisting of soil solids and two fluids: air and water.

In nature, the hydrologic cycle of water on earth will have various movements in and out of the superficial ground soil through precipitation, infiltration, and evaporation processes. Since the movement of water will continue throughout seasonal periods, the ground soil can anticipate degrees of saturation ranging from $0 < S < 1$. The zone above the water table is referred to as the vadose zone. An illustration of the vadose zone is shown in Figure 2.1.1 along with typical profiles of degree of saturation (S), pore water pressure (u), total stress (σ), and effective and horizontal vertical stresses representative of hydrostatic conditions (i.e., no infiltration or evaporation). It is possible for soils to be saturated above the water table within the capillary fringe designated by the dashed red line in Figure 2.1.1.

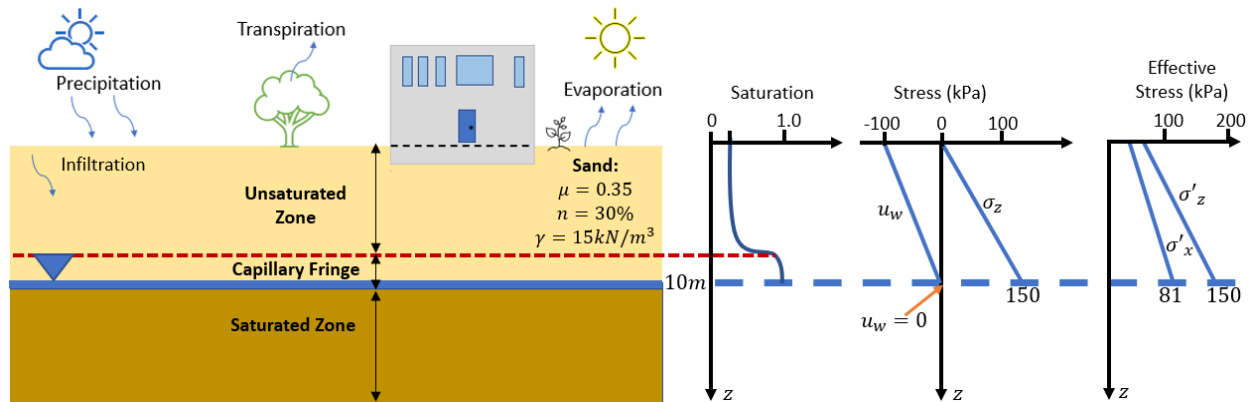


Figure 2.1.1 Typical near-surface unsaturated soil profile with hydrostatic conditions (after Lu and Likos 2004)

The vadose zone can be subdivided into three regimes: capillary fringe, funicular and pendular. The capillary fringe regime is the zone located immediately above the water table source and is saturated or nearly saturated. If air is present in the capillary regime, it is in the form of occluded bubbles that may have become trapped during fluctuations in the water table depth. The height of the capillary fringe is related to the air entry suction for the soil, which will be introduced later. The funicular regime represents the zone where pore air can enter the void spaces between the water and soil particles. As the air enters the pores, desaturation commences, and the pore water exists in menisci at soil particle contacts. The air and water phases in the soil are typically continuous in the funicular regime. In the pendular regime at heights well above the water table, the pore water is discontinuous and is only present in thin films around the soil particles while the air phase is continuous throughout the voids of the soil skeleton.

The depth of the water table is defined as the location where the pore water pressure is zero (in gage pressure). Below the water table, the water is continuous (no curvature or interfacial tension due to the lack of air) throughout the soil skeleton and is under positive pore water pressures. Above the water table, the pore water is under negative pore water pressures. Negative water pressures arise from capillary forces at the curved air-water interface. Although it is common

to assume that pore air pressures are equal to zero (in gage pressure) or equal to the atmospheric pressure (in absolute pressure), the air pressure may not be zero if the air is occluded in the water phase or if void collapse causes compression of air-filled voids. Regardless, as a result of the negative pore water pressures, positive matric suction is exhibited in the soil above the water table. Different soils such as clays and sands will have different distributions of degree of saturation above the water table, which are governed by the soil-water retention curve (SWRC) as shown in Figure 2.1.2. The shape of the SWRC is related to the pore size distribution and soil particle mineralogy, which will lead to different interactions between the pore water and the soil solids that can be referred to as adsorption. For granular soils like sands and gravel, the SWRC is mainly related to the pore size distribution and capillarity caused by air-water menisci at the particle contacts. The SWRC is path dependent and will have different shapes depending on whether the soil is being wetted or dried, a phenomenon referred to as hydraulic hysteresis.

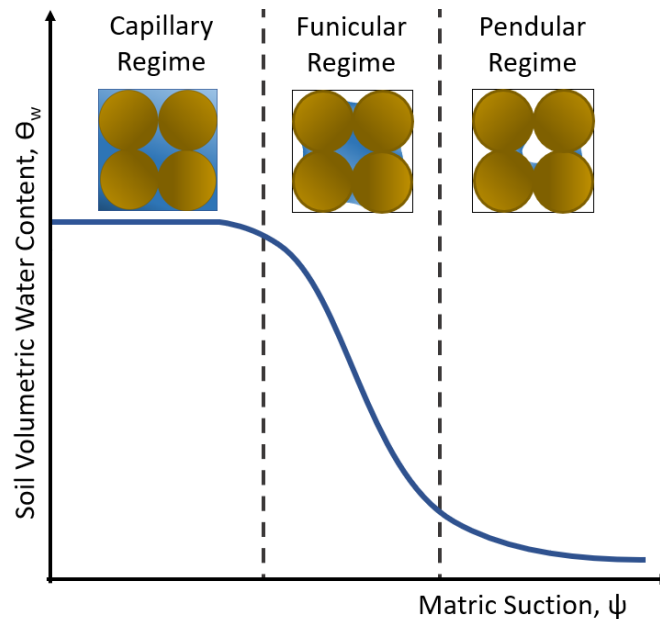


Figure 2.1.2 Typical shape of the soil-water retention curve (SWRC) partitioned into the capillary, funicular and pendular regimes (after Lu and Likos 2004).

Seasonal water movement either due to infiltration or evaporation from the ground surface or due to water table fluctuations will not only change the distribution in water within the soil layer and the pore air and water pressures, but the presence of water in the soil may change the total unit weight of the soil. Water movement or fluctuating ground water tables could present issues with slope instability due to increases in pore fluid pressures or deformation changes related to effective stress changes, which are described in the next section. As water is superficially evaporated due to earthen heating cycles, this change in degree of saturation could lead to shrinkage of the soil skeleton due to the changes to the effective stress state. This study assumes that there is no water movement in an unsaturated soil layer due to infiltration or evaporation or water table fluctuations, and that changes in pore air and water pressures or degree of saturation are only caused by cyclic or seismic shearing of the soil layer.

2.2 Effective Stress in Unsaturated Soils

Terzaghi (1936) defined the effective stress in a fully saturated soil as the total stress state in a three-dimensional cartesian coordinate minus the neutral orthogonal pressures (also called the pore water pressures). For example, the vertical effective stress σ'_v can be defined as follows:

$$\sigma'_v = (\sigma_v - u_w) \quad (2.2.1)$$

where σ'_v is the total stress and u_w is the pore water pressure. In a free-field condition with hydrostatic conditions, the total stress is equal to the depth below the ground surface multiplied by the total unit weight of the soil, and the pore water pressure is equal to the depth of a point of interest below the water table multiplied by the unit weight of water. Use of Terzaghi's effective stress implies that the water pressure acts in every direction with equal intensity and the difference between the total stress and pore water describes the stress state of the soil structure (Fredlund

2016). Terzaghi's effective stress equation is still continuously used in design practices to describe the stress state change for a soil beneath the ground water table (i.e., fully saturated soil).

Bishop and Blight (1963) proposed a definition for the effective stress state of an unsaturated soil, given as follows:

$$\sigma_v' = (\sigma_v - u_a) + \chi(u_a - u_w) \quad (2.2.2)$$

where the term $\psi = (u_a - u_w)$ is the matric suction and describes the air-capillary water interface and adsorptive forces within the pores, $\sigma_n = (\sigma_v - u_a)$ is the net vertical stress, and χ is an effective stress parameter that is a property of the soil and must be defined experimentally. In wet sands, adsorptive forces are negligible and negative pore water stresses contribute an apparent cohesive strength through capillarity arising from air-water surface tension (Lu and Likos 2004). For clays, adsorptive forces associated with particle-water interaction associated with clay mineralogy play a more important role in water retention (Lu et al. 2016). When χ is equal to 1 the soil is considered fully saturated, and the equation reduces to Terzaghi's effective stress given in Equation 2.2.1. When χ is equal to zero, the soil is considered dry with air filling all the voids, and the effective stress is equal to the net stress:

$$\sigma_v' = \sigma_v - u_a \quad (2.2.3)$$

Many definitions have been proposed for χ , but most researchers have assumed that it is linked with the degree of saturation or matric suction in the soil. For example, Lu et al. (2010) assumed that χ is equal to the soil's effective saturation (S_e), which can be defined as follows:

$$S_e = \frac{S - S_{res}}{1 - S_{res}} \quad (2.2.4)$$

where S_{res} is the residual saturation. An advantage of using this definition is that the effective saturation is linked to the suction through the SWRC. When setting χ equal to the effective

saturation in Equation 2.2.2, Lu et al. (2010) proposed the definition of a new variable referred to as the suction stress, given as follows:

$$\sigma_s = S_e(u_a - u_w) \quad (2.2.5)$$

In this manner, the vertical effective stress in an unsaturated soil can now be defined from Equation 2.2.2 as follows:

$$\sigma_v' = (\sigma_v - u_a) + \sigma_s \quad (2.2.6)$$

This equation indicates that unsaturated conditions will lead to an increase in the effective stress of the soil. However, the effect of matric suction on the effective stress will depend on the amount of water in the soil through the effective saturation. For example, the matric suction will increase linearly with height above the water table for the hydrostatic profiles shown in Figure 2.1.1, but the effective saturation will decrease with height above the water table according to the shape of the SWRC. Accordingly, the SWRC provides the link between the state variables of matric suction and water content which can be used to describe the amount of energy in the pore water voids for a given amount of saturation (Lu et al. 2010). The SWRC is also linked to the definition of the effective stress state of a soil if the density and pore void skeleton remain unchanged. The SWRC is the constitutive relationship at hydraulic equilibrium (no flow) between total suction and volumetric water content, gravimetric content, degree of saturation or effective saturation. Since hydraulic hysteresis occurs during the entry and/or exit of air and water in the pore voids of the soil skeleton, there will be two different curves corresponding to either the wetting or drying path of the soil (Khalili et al. 2008).

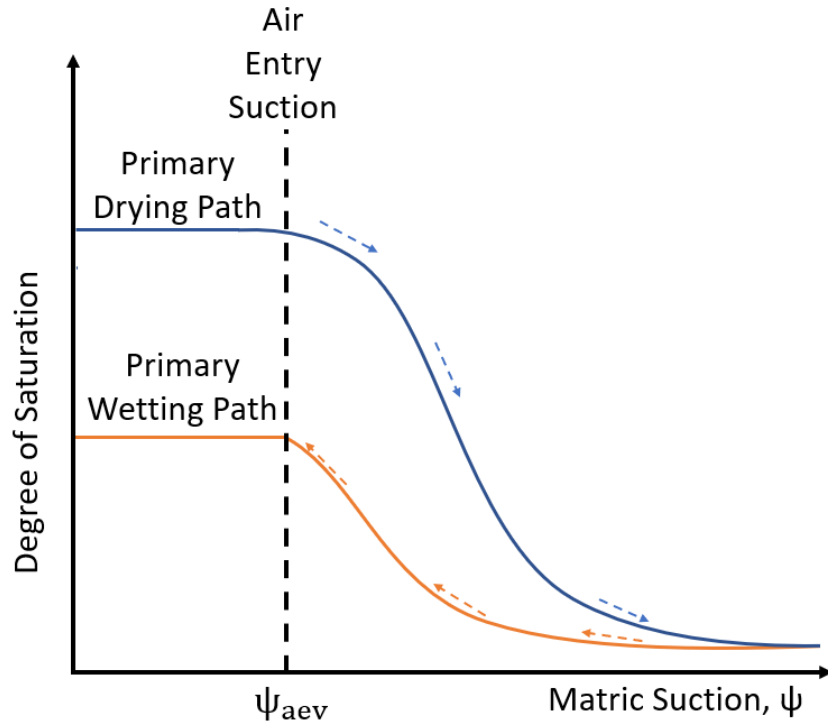


Figure 2.2.1 Schematic of a hysteretic SWRC showing typical shapes of the primary drying and wetting paths in blue and orange, respectively.

The water content, shape, radius, and packing arrangement of the solid particles will influence the shape of the SWRC and the range of effective stresses possible during wetting and drying (Lu et al. 2004). For sands, capillarity is the dominating suction mechanism, and the slope of the SWRC is controlled by the arrangement of the pore water menisci connecting the soil skeleton (Lu and Likos 2004).

A way to characterize the potential capillarity stresses in a soil profile is to have extensive knowledge about the soil’s water retention properties during drying or wetting phases. Brooks and Corey (1964) derived a discontinuous function to characterize the permeability of air and water in terms of the air entry value or “bubbling pressure” which was used to help understand the hydraulic retention properties of soil for farming advancements. The air entry value is the quantity of suction at which the surface tension between air and water is overcome and air can begin entering the pore

void spaces of a fully saturated soil transitioning to an unsaturated soil (i.e., drying curve). Air expulsion suction corresponds to the rewetting curve path and represents the suction at which air-filled voids collapse under water infiltration (Khalili et al. 2008). While the Brooks and Corey (1964) model may have the best fundamental definition, van Genuchten (1980) proposed a smoother SWRC which resolves issues with the discontinuity at the air entry suction that affect numerical modeling. The van Genuchten (1980) SWRC is given as follows:

$$S_e = \left\{ \frac{1}{1 + [\alpha_{vg} (u_a - u_w)]^{N_{vg}}} \right\}^{1 - \frac{1}{N_{vg}}} \quad (2.2.7)$$

where α_{vg} and N_{vg} are empirical fitting parameters that are related to the inverse air entry pressure and the pore size distribution, respectively. Using the van Genuchten (1980) SWRC model, Lu et al. (2010) derived an equation the suction stress of the soil at a given density, given as follows:

$$\sigma_s = \left[\frac{u_a - u_w}{(1 + [\alpha_{vg}(u_a - u_w)]^{N_{vg}})^{1 - \frac{1}{N_{vg}}}} \right] \quad (2.2.8)$$

Similar to the SWRC, the suction stress characteristic curve can be plotted showing the relationship between the suction stress and the degree of saturation, as shown in Figure 2.2.2. If the pore size distribution parameter N_{vg} is larger than 2.0 (most apparent in sands and silts), the SSCC increases and then decreases. When the pore size distribution parameter N_{vg} is less than 2.0 (most apparent in clays), the SSCC increases monotonically.

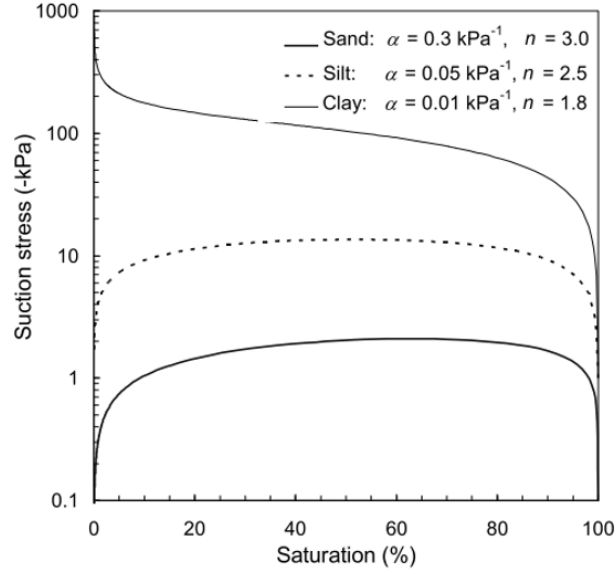


Figure 2.2.2 SSCCs representative of sands, silts, and clays (Lu et al. 2010)

Accordingly, the effective vertical stress (σ_v') in an unsaturated soil can be calculated by combining the suction stress and normal stress as follows (Lu et al. 2010):

$$\sigma_v' = (\sigma_n - u_a) + \left[\frac{u_a - u_w}{(1 + [\alpha_{vg}(u_a - u_w)]^{N_{vg}})^{1 - \frac{1}{N_{vg}}}} \right] \quad (2.2.9)$$

The effective stress obtained from the SWRC fitting parameters (α_{vg}, N_{vg}) only applies to the conditions where the pore size distribution is not changed. This implies that Equation 2.2.9 should be used with caution when studying seismic compression of unsaturated soils as the pore size distribution may change.

2.3 Cyclic Response of Soils

The dynamic response of soils is dependent upon the shear strain magnitude. Ground vibrations induce strain in the soil and can occur during heavy construction, factory machine vibrations or earthquakes. Earthquakes impose a range of wave types on soil layers, but it is well known that seismic shear waves have the greatest effect on permanent ground deformations (Hardin and Drnevich 1972). Various models have been developed from empirical data to predict

the dynamic response of shear stress and strain in soils during dynamic loading or ground action (Hardin and Black 1969; Hardin and Drnevich 1972). The shear stress-strain behavior of soils can be idealized as a hyperbola using the small-strain shear modulus (G_i) and the ultimate shear stress, (τ_{ult}) to depict the initial stage of shear loading of a soil as shown in Figure 2.3.1 (Hardin and Drnevich 1972).

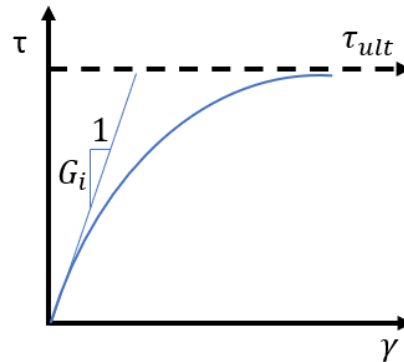


Figure 2.3.1 Example of a hyperbolic shear stress-shear strain curve with a definition of the small strain shear modulus G_i

At small strains (10^{-4} to 10^{-3} %), the shear modulus is constant, the material is linear elastic, and interparticle connections remain intact (i.e., no permanent particle rearrangement). At a certain threshold level of shear strain, cyclic or seismic shearing movement causes individual soil particle contacts to redistribute into denser arrangements resulting in distortion of the original soil skeleton. Hardin and Drnevich idealized that the response of soil degradation to induced shearing can be captured by the ratio of the small strain shear modulus (G_i) and the shear modulus at the varying strain (G/G_i) in a hyperbolic plot called the shear modulus reduction curve (Figure 2.3.2). It is important to note that seismic compression is only expected when the cyclic shear strain amplitude is greater than the cyclic threshold shear strain.

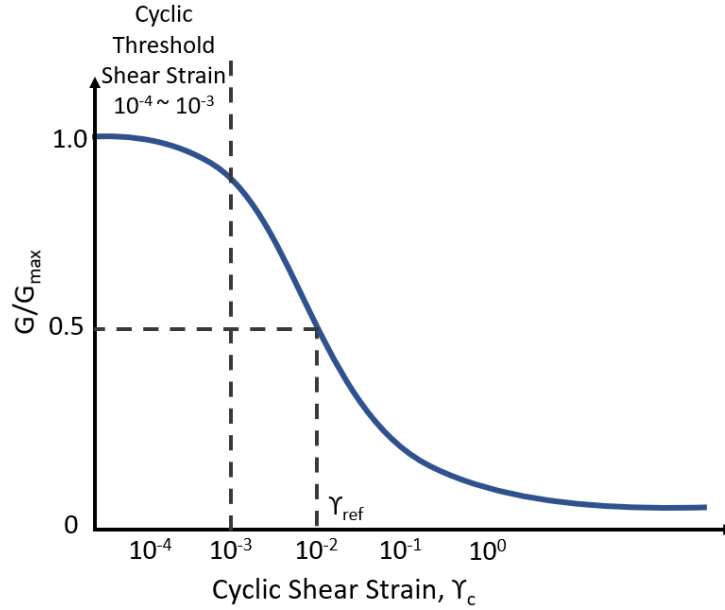


Figure 2.3.2 Example of a shear modulus reduction curve

Many studies have observed that the small strain shear modulus is governed by soil characteristics such as void ratio, degree of saturation and effective stress (Hardin and Drnevich 1972; Hardin 1978; Khosravi and McCartney 2009, 2012; Khosravi et al. 2010; Dong et al. 2016, 2017). Hardin (1978) proposed the following empirical power law relationship to describe the relationship between the small strain shear modulus of a dry or saturated soil with the void ratio, overconsolidation ratio (OCR) and mean effective stress (σ'_m):

$$G_i = AF\epsilon(\text{OCR})^k P_a^{1-n} (\sigma'_m)^n \quad (2.3.1)$$

where ϵ is a void ratio factor given by:

$$F(e) = \frac{1}{0.3 + 0.7e^2} \quad (2.3.2)$$

Degradation of the shear modulus occurs at shear strains induced by earthquake or repeated dynamic loading greater than those in the elastic regime and result in irreversible deformations of the soil fabric. The decreasing trend in the reduction modulus curve as strain increases exemplifies the plastic evolutions occurring in the soil during cyclic shearing.

Studies conducted on the shear modulus of unsaturated soils indicate that the small strain shear modulus will increase during drying of soils, with the results for several soils reinterpreted in terms of effective stress according to Equation 2.2.2 summarized by Khosravi and McCartney (2009). Khosravi and McCartney (2012) proposed an equation for the small strain shear modulus (G_i) of unsaturated soils using a double-hardening model extended from Equation 2.3.1:

$$G_i = AP_a \left[\frac{\sigma'_{mc0}}{(\sigma'_m - u_a)} \exp\left(\frac{\Delta e^p}{\lambda - \kappa}\right) \right]^K \left[\frac{(\sigma'_m - u_a)}{\sigma'_m} \exp(b[S_{e0} - S_e]) \right]^{K'} \left(\frac{\sigma'_m}{P_a} \right)^n \quad (2.3.3)$$

where σ'_{mc0} is the initial mean effective preconsolidation stress and b, K, and K' are hardening parameters building upon the model of Wheeler et al. (2003) to consider the effects of changes in void ratio or changes in degree of saturation on the shear modulus of unsaturated soils. Their equation was used to capture hysteretic changes in the small-strain shear modulus during hydraulic hysteresis (drying and wetting). The model of Khosravi and McCartney (2012) indicates that during drying at constant mean net stress, the shear modulus will increase but that during subsequent rewetting, the shear modulus will decrease upon a different path. This implies that drying and wetting of soils can lead to permanent changes in the shear modulus due to plastic hardening.

One issue with the use of Equation 2.3.3 is that it is very difficult to apply with several parameters. Alternatively, Dong et al. (2016) proposed a simplified model for the small strain shear modulus of an unsaturated soil based on measurements of the small strain shear modulus using bender elements:

$$G_i^{unsat} = G_i^{sat} \left(\frac{1}{S_e} \right)^\beta \left(\frac{\sigma'_m}{P_a} + 1 \right)^{\gamma_o} \quad (2.3.4)$$

where γ_o and β are empirical fitting parameters. This model was found to represent the small strain shear modulus of unsaturated soils well and has a consistent definition to that of Hardin (1978).

During cyclic shearing of a soil specimen, the sign of the shear strain will reverse, and the soil will be loaded and unloaded in a hysteretic manner. If the strain level is greater than the cyclic threshold shear strain, plastic deformations will occur and the hysteretic stress-strain curve will form a closed loop, as shown in Figure 2.3.3. As the shear strain amplitude increases, a decrease in shear modulus is expected according to the shear modulus reduction curve shown in Figure 2.3.2, which has been represented by the following equation (Darendeli 2001):

$$\frac{G}{G_i} = \left[\frac{1}{1 + \left(\frac{\gamma}{\gamma_r}\right)^a} \right] \quad (2.3.3)$$

where γ_r is a reference strain and a is an empirical fitting parameter. The seismic compression model developed in this study will use a form of this equation that is related to the derivative of a hyperbolic stress-strain curve and will be introduced in Chapter 3. The reversal shear stress is expected to follow the small strain shear modulus slope until reaching higher strains. Reload shearing of the soil follows the same trend (all stages are depicted in Figure 2.3.3) and represent the shear stress strain hysteresis loop. The area within the shear stress strain hysteresis loop in Figure 2.3.3 corresponds can be used to calculate the damping ratio of the soil D , which is another key soil dynamic property. The seismic compression obtained from the semi-empirical model developed in this study depends only on the shear modulus G , so the damping ratio is not discussed further in this study even though it could be derived from the hysteretic stress-strain curve.

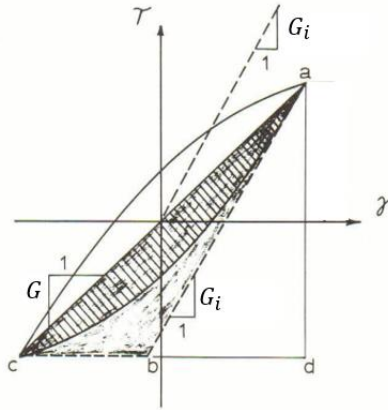


Figure 2.3.3 Example of shear stress-strain hysteresis of soils during loading, unloading and reloading (Hardin and Drnevich 1972)

2.4 Seismic Compression of Unsaturated Soils in Literature

Compression of soils during is expected during cyclic or seismic shearing and may occur in either drained or undrained conditions depending on the rate of shearing (Youd 1972, Silver and Seed 1971; Rong and McCartney 2019, 2020b). Historically in soil mechanics design, it has been considered conservative to assume the soil to be fully saturated or dry in settlement predictions as these are considered extreme cases of the soil's stress state (Tokimatsu and Seed 1987, Silver and Seed 1971). For saturated soils, seismic compression is not possible because the pore water is incompressible. Instead, cyclic or seismic shearing of saturated soils will lead to an increase in pore water pressure, which may result in liquefaction. It is possible that after liquefaction occurs, dissipation of the pore water pressures may lead to reconsolidation and corresponding settlements after the end of earthquake shaking (Bray and Olaya 2022). It is interesting to note that even a slight reduction of degree of saturation can increase the soil's resistance to liquefaction (Tsukamoto et al. 2002; Okamura et al. 2006). For unsaturated soils, soil interparticle stresses will increase due to capillary effects, and occluded air bubbles can mitigate the generation of pore water pressures during seismic shearing. However, there are cases where unsaturated soils with relatively high initial degrees of saturation can still liquefy under seismic excitation (Unno et al. 2008).

Ghayoomi et al. (2013) developed an empirical model that combined estimates of the post-liquefaction reconsolidation of unsaturated soils with estimates of the collapse of air-filled voids to predict the seismic compression of unsaturated soils in all three water retention regimes. Their model was able to capture trends in seismic compression of sand specimens with different initial degrees of saturation observed from centrifuge modeling results as shown in Figure 2.3.4. However, the model includes many parameters that are not easy to determine which could have major effects on the trends in the seismic compression as a function of the initial degree of saturation. The model being developed in this study focuses on predicting the seismic compression of unsaturated soils during earthquake shaking using hydro-mechanical coupling, and reconsolidation settlements due to dissipation of excess pore water pressures are not included.

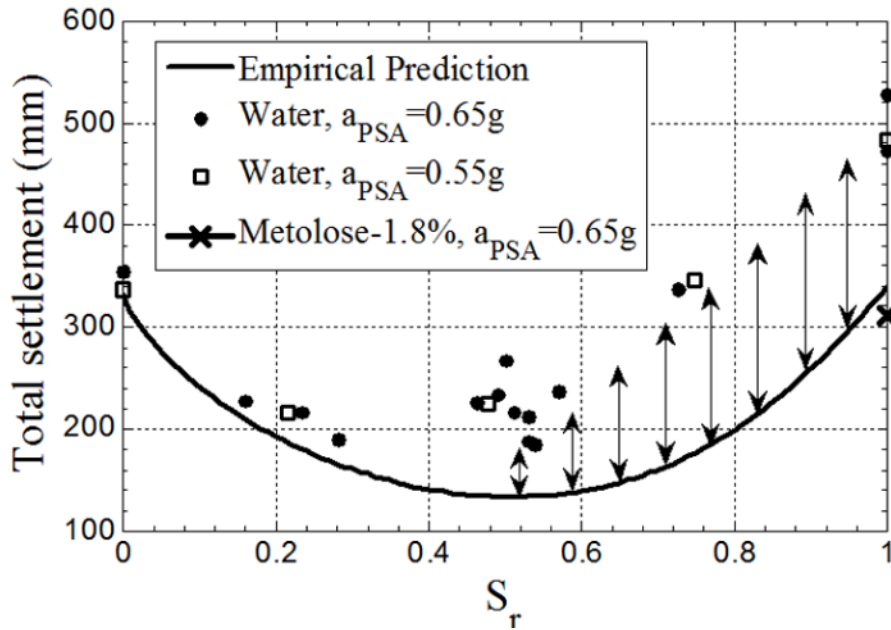


Figure 2.3.4 Comparison between seismic compression results from centrifuge tests and the empirical model of Ghayoomi et al. (2013)

In unsaturated soils with lower initial degrees of saturation, seismic compression is expected during strong shaking by earthquakes with shear strain amplitudes greater than the cyclic threshold shear strain (Stewart et al. 2004, Rong and McCartney 2019, 2020b). Earthquakes and

aftershocks often have rapid shearing with short durations that can lead to undrained conditions even for sands. Unsaturated soils have lower hydraulic conductivity than saturated soils, so it is expected that undrained conditions will be present in unsaturated soils during earthquake shaking. In undrained conditions, pore air and water pressures increase during shaking and compression of the air voids may occur which coincides with an increase in the saturation of the overall soil system. Several studies have performed cyclic triaxial tests (Unno et al. 2008; Kimoto et al. 2011) and cyclic simple shear tests (Whang et al. 2004; Duku et al. 2008, Craciun and Lo 2010; Milatz and Grabe 2015; Rong and McCartney 2019, 2020) to characterize the cyclic response of unsaturated soils. Early cyclic simple shear tests involved compaction of soils to different initial degrees of saturation followed by undrained shearing without measurement of changes in pore air or water pressures (Whang et al. 2004, 2005; Duku et al. 2008). It was not possible to separate the effects of hydro-mechanical coupling from the effects of soil structures induced by the compaction process. Other studies characterized the changes in pore air and water pressures and stress-strain responses during cyclic shearing (Unno et al. 2008; Kimoto et al. 2011; Craciun and Lo 2010; Milatz and Grabe 2015; Rong and McCartney 2020a, 2020b). Results from these studies indicate that it is critical to measure the pore air and water pressures in specimens with the same initial preparation conditions to effectively interpret the results from seismic shearing tests. In the funicular regime, Rong and McCartney (2020b) found that different changes in pore air and water pressures may occur during cyclic shearing, which is a focus of the model development in this study. In most of the studies on seismic compression, the soil skeleton compresses in response to the redistribution of the pore void spaces and the SWRC shifts in different ways depending on the drainage conditions (Rong and McCartney 2020a, 2020b). A thorough overview of the results from seismic compression measurements from cyclic simple shear and triaxial tests in the literature can

be found in Rong and McCartney (2021a). Chapter 4 also includes a discussion on the results from cyclic simple shear tests performed by Rong and McCartney (2021a) along with unpublished data from additional cyclic simple shear tests.

3 Model

3.1 Stresses and Strains during Cyclic Simple Shear Testing

This study involves the development of a semi-empirical model for the seismic compression of unsaturated soils that is calibrated based on the results from cyclic simple shear tests presented by Rong and McCartney (2020b). Cyclic simple shear tests first involve application of a vertical stress to a specimen confined with a housing that prevents lateral expansion, resulting in an at-rest initial stress state, as shown in the central figure of Figure 3.1.1. The horizontal stress is typically estimated using a coefficient of lateral earth pressure at rest, K_0 , which can be defined using Jaky's equation and the friction angle or Hooke's law and elastic parameters. Then shear stresses are imposed to the specimen without changing the mean stress. In a cyclic simple shear test, the specimen is typically sheared in one direction until reaching the target cyclic shear strain amplitude, then the direction of shearing is reversed until reaching the cyclic shear strain amplitude in the other direction. The shear stresses required to reach the shear strain amplitude are recorded during the test, and may decrease or increase depending on the changes in soil properties during shearing.

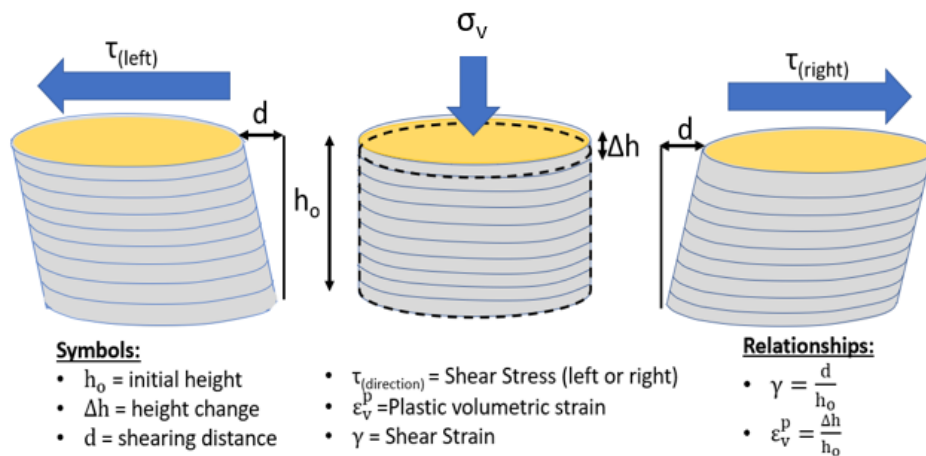


Figure 3.1.1 Key variables in a cyclic simple shear test on a soil specimen after vertical loading and during bi-directional cyclic simple shearing.

Mohr circles for a cyclic simple shear test are shown in Figure 3.1.2. The initial stress state is shown as a black circle, with $\sigma_h = K_0 \sigma_v$. This initial anisotropic stress state implies that there are initially shear stresses in the specimen. A cyclic simple shear test involves increasing the shear stresses applied to an element of soil, which lead to expansion of the circle about the same mean stress until reaching the blue circle. It is critical in a cyclic simple shear test that the blue circle does not reach the failure envelope. Reversal of the shear stresses makes the circle return to the at-rest state, after which shearing in the opposite direction causes the circle to expand back to the blue circle. The reversal of signs of the shear stresses during cyclic shearing is represented by the black and blue vertical lines on the Mohr circle. Because the mean effective stresses do not change during the cyclic simple shear test, a simplified constitutive model can be developed to represent seismic compression process that only focuses on the stress paths shown in Figure 3.1.2.

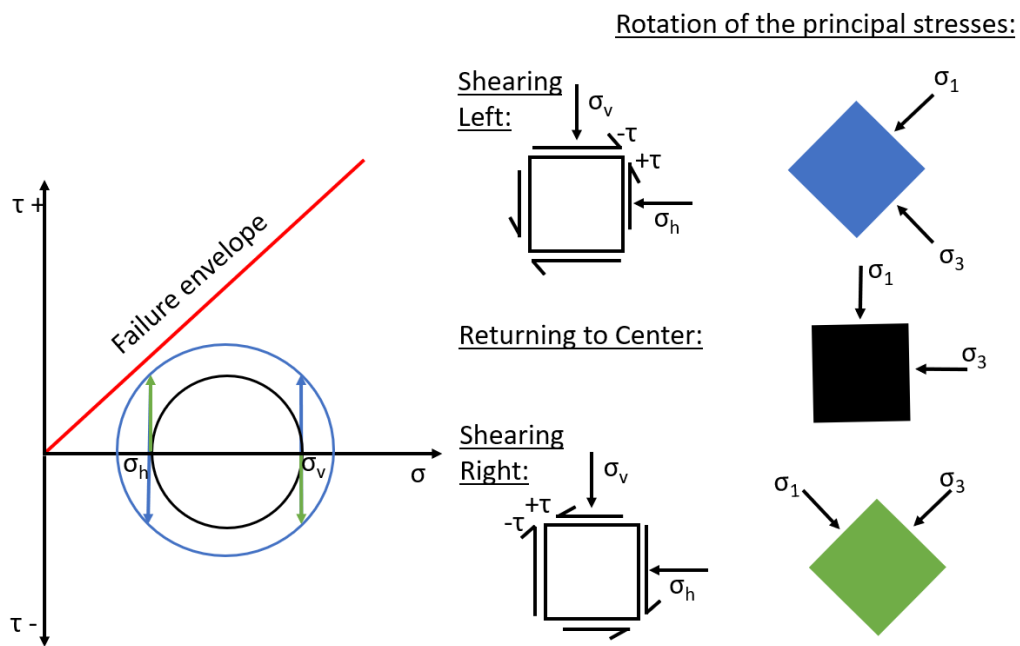


Figure 3.1.2 Schematic of the changes in stress state during cyclic simple shear testing of a soil specimen showing the directions of the stresses during applied shear strain testing

The first step in developing the semi-empirical constitutive model for seismic compression was to define a backbone curve. The backbone curve represents the shear stress-strain curve if the soil were sheared monotonically to failure (in either direction of shearing as shown in Figure 3.1.2). A major assumption of this study is that the backbone curve has a shape similar to a hyperbola. Hyperbolic models have been used most frequently to represent the stress-strain curves obtained from triaxial tests (e.g., Duncan et al. 1980) so several modifications are necessary to apply a hyperbolic model to cyclic simple shear tests. The equation for a hyperbolic shear stress strain curve, which provides the shear stress for any applied shear strain γ_{applied} , is given as follows:

$$\tau = \left(\frac{\gamma_{\text{applied}}}{\frac{1}{G_i} + \frac{\gamma_{\text{applied}} * R_f}{\tau_{\text{ult}}}} \right) \quad (3.1.1)$$

where G_i is the initial shear modulus (or small-strain shear modulus), τ_{ult} is the ultimate shear stress from the shape of the hyperbola, and R_f is a reduction factor that is used to adjust the curve to the actual shear stress at failure τ_f observed in an experiment. An example of a hyperbolic shear stress-strain curve is as shown in Figure 3.1.3.

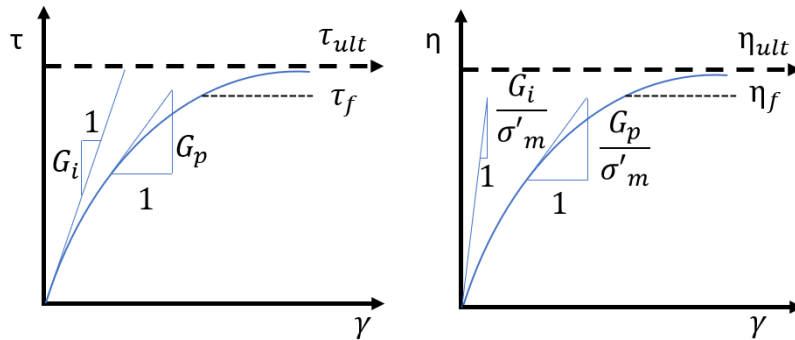


Figure 3.1.3 Backbone curve shape from the hyperbolic model: (a) Shear stress-strain curve; (b) Shear stress ratio-shear strain curve

This figure also shows that as the shear strain increases, the shear modulus decreases from G_i to a lower value of plastic shear modulus G_p , which will be defined in the next section. A normalized version of the shear stress-strain curve is shown in Figure 3.1.3 in terms of the shear stress ratio $\eta = \tau/\sigma_m'$, $\eta_{ult} = \tau_{ult}/\sigma_m'$, and $\eta_f = \tau_f/\sigma_m'$.

Additional modifications are necessary to the hyperbolic model when simulating a cyclic simple shear test (Naesgaard 2011). Specifically, the backbone curve only represents the shape of the shear stress-strain curve for the first $N = 0.25$ cycles of shearing. When the applied shear strain is reversed, a hysteresis loop can be formed that has a different shape from the backbone curve but has the same parameters. The first step in defining the equations for this hysteresis loop is to define the cyclic shear stress τ_c that will occur during application of a certain cyclic shear strain amplitude γ_c is defined as follows:

$$\tau_c = \left(\frac{\gamma_c}{\frac{1}{G_i} + \frac{\gamma_c * R_f}{\tau_{ult}}} \right) \quad (3.1.2)$$

After reaching τ_c in a cyclic simple shear test after the number of cycles $N = 0.25$, the direction of shearing will be reversed until reaching τ_c in the opposite direction of shearing when $N = 0.75$. The equations for the hysteretic shear stress strain curves can be derived from the equation for the backbone curve. Specifically, the equation for the shear stress strain curve for increasing applied strain (shearing to the right in Figure 2.1) is given as follows:

$$\tau = \left(\frac{\gamma_c + \gamma_{applied}}{\frac{1}{G_i} + \frac{(\gamma_c + \gamma_{applied}) * R_f}{2 * \tau_{ult}}} \right) - \tau_c \quad (3.1.3)$$

Similarly, the equation for the shear stress strain curve for decreasing applied strain (shearing to the left in Figure 2.1) is given as follows:

$$\tau = \left(\frac{\gamma_c - \gamma_{\text{applied}}}{\frac{1}{G_i} + \frac{(\gamma_c - \gamma_{\text{applied}}) * R_f}{2 * \tau_{\text{ult}}}} \right) + \tau_c \quad (3.1.4)$$

In this sense, Equations 3.1.3 and 3.1.4 can be used to form a hysteretic shear stress-strain loop as shown in Figure 3.1.4. The backbone curve intersects the hysteresis loop at $\pm(\gamma_c, \tau_c)$.

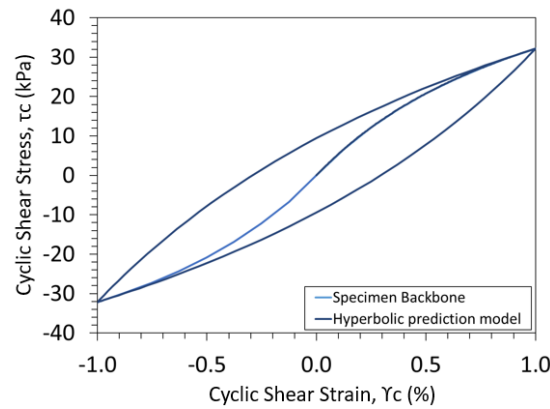


Figure 3.1.4 Hysteretic loop showing the hyperbolic shear stress strain reversals along with the hyperbolic backbone curve.

3.2 Prediction of the Volumetric Strain during Cyclic Shearing

As the unsaturated specimen is cyclically sheared in undrained conditions, particles will move into denser arrangements causing volumetric contraction of the soil skeleton. A simplified schematic depicting the volumetric changes during undrained cyclic simple shearing of spherical particles is seen in Figure 3.2.1. Although the water in the unsaturated specimen will likely be distributed throughout the specimen height, water will take up more of the space after the specimen rearranges into a tighter packing, causing an increase in degree of saturation.

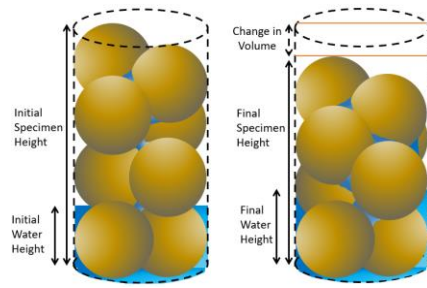


Figure 3.2.1 Schematic of soil particle rearrangement before and after cyclic shearing showing initial and final heights of specimen and changes in degree of saturation.

Due to the nonlinear shape of the hyperbolic stress-strain curve in Figure 3.1.4, it is assumed that each cycle of shearing will cause plastic shear strains. The experimental study of Youd (1971) suggests that plastic volumetric strains will thus occur during each cycle of shearing and will accumulate over multiple cycles. Accordingly, a flow rule is needed to relate the plastic shear strains with the plastic volumetric strains. The flow rule developed in the UBCSAND model was used to capture the indirect plastic volumetric strains caused by the shear stress-shear strain response of the soil. UBCSAND is a semi-empirical model described by Beaty and Byrne (2011) that combines a normalized semi-empirical hyperbolic shear stress-strain curve shown in Figure 3.2.2 with the elasto-plastic framework developed by Byrne et al. (1995). UBCSAND was originally developed to study the liquefaction behavior of sands and silty sands having relative densities less than 80% during monotonic shearing (Puebla et al. 1997) but was later extended to study liquefaction during earthquakes (Byrne and Park 2003; Byrne et al. 2004; Naesgaard 2011). This model has been adapted to study the liquefaction of unsaturated soils during earthquake shaking by assuming a combined bulk stiffness for the air and water pressures (Seid-Karbasi and Byrne 2006), but it has not been used to investigate the seismic compression of unsaturated soils.

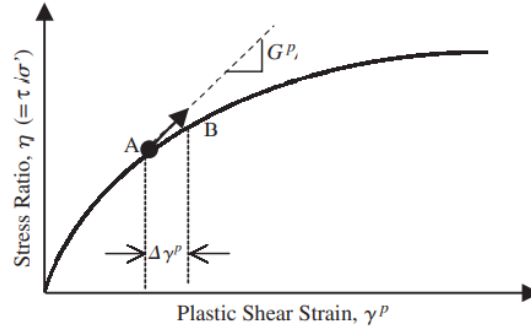


Figure 3.2.2 UBCSAND model hyperbolic stress-strain relationship (Byrne and Park 2003)

In the UBCSAND model, the initial small strain shear modulus is dependent on the changes in the mean effective stress through the following relationship:

$$G_i = k_G^e * P_a * \left(\frac{\sigma'_m}{P_a} \right)^{n_e} \quad (3.2.1)$$

where n_e is the elastic shear modulus exponent that governs the effect of mean effective stress on the shear modulus and k_G^e is the elastic shear modulus number. The first quarter cycle of shear stress – shear strain response from a drained cyclic simple shear test (i.e., the backbone curve) is typically used to calibrate the best fit values of k_G^e and n_e . Chapter 5 will include a summary of the model calibration, and Appendix A1 shows the procedure for defining the hyperbolic model parameters.

As mentioned, the shear stress-strain curve in the UBCSAND model is normalized. The normalized shear stress is defined as $\eta = \tau/\sigma'_m$. The plastic shear modulus is the ratio of the plastic shear stress and the plastic shear strain. To avoid having to carry the mean effective stress through all calculations as shown in Figure 3.1.3, the UBCSAND model defines the plastic shear modulus in a normalized manner. For example, the initial plastic shear modulus (G_i^p) at small strains is defined by dividing the small-strain shear modulus from Equation 3.2.1 by the mean effective stress, as follows:

$$G_i^P = k_G^e \times \left(\frac{\sigma'_m}{P_a} \right)^{n_e-1} \quad (3.2.2)$$

Accordingly, G_i has the same units as the shear stress while G_i^P is dimensionless. When shear stresses increase, the normalized tangent slope of the plastic response can be predicted the derivative of the hyperbolic curve, as follows:

$$G_p = G_i^P \times \left[1 - \frac{\tau}{\tau_f} R_f \right]^{0.5} \quad (3.2.3)$$

This equation indicates that the normalized plastic shear modulus is a function of the mean stress, the shear stress at failure (τ_f), and the failure ratio (R_f).

The incremental change in the developed stress ratio can be computed as the derivative of the hyperbolic stress-strain curve shown in Figure 3.2.2 as follows:

$$\eta_d = \frac{\tau}{\sigma'_m} = \sin \phi_d \quad (3.2.4)$$

$$\Delta \eta_d = \left[\frac{\Delta \tau}{\sigma'_m} - \left(\frac{\tau}{(\sigma'_m)^2} \right) \Delta \sigma'_m \right] \quad (3.2.5)$$

where ϕ_d is the developed friction angle.

In general, due to the nonlinear shape of the hyperbolic stress strain curve, any shear strains generated during loading or reloading are be considered plastic shear strains. The plastic shear response is captured assuming a hyperbolic relationship between the incremental changes in the plastic shear strains ($\Delta \gamma^P$) and the developed stress ratio ($\Delta \eta_d = \frac{\Delta \tau}{\sigma'_m}$), as follows The plastic shear strains can be computed using the change in the developed stress ratio and the plastic shear modulus.

$$\Delta \gamma^P = \Delta \eta_d \left(\frac{1}{G^P} \right) \quad (3.2.6)$$

UBCSAND uses a flow rule developed from energy considerations to compute the coupling between the plastic shear strain and the plastic volumetric strain response, as follows:

$$\Delta\varepsilon_v^p = \Delta\gamma^p(\sin\phi_{cv} - \eta_d) \quad (3.2.7)$$

where (ϕ_{cv}) is the constant volume friction angle (Puebla et al. 1997). Additional derivations related to the flow rule are presented in Appendix A5. Plastic volumetric strains in loose sands are contractive and are influenced by the evolution of the developed stress ratio. In dense sands, the plastic volumetric strains are dilative (Puebla et al. 1997). Lateral constraint during the applied shear strain in a cyclic simple shear test indicates that the plastic volumetric strain will be due solely to vertical axial strains (e.g., no radial strains).

An important aspect of this model is that the cumulative volumetric strain only accrues during loading/reloading and not during unloading because loading/reloading is a plastic response causing permanent deformations whereas unloading is considered to be an elastic response garnering no permanent deformation of the structure. Unloading is defined as the case when the shear stress is reduced from a value of $\tau = \tau_c$ until $\tau = 0$. The schematic in Figure 3.2.3 shows the development of plastic shear and volumetric strains during loading/reloading (labeled in red) and elastic unloading (labeled in green). Elastic changes in volumetric strain are only expected if there are changes in mean effective stress, so during elastic unloading (labeled in green), no volumetric strains will occur.

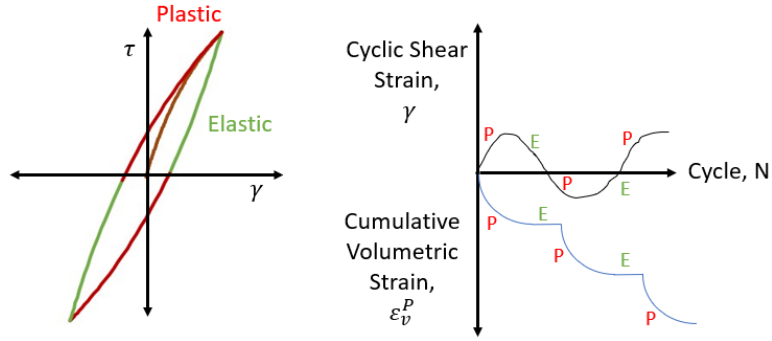


Figure 3.2.3 Hysteretic shear stress-shear strain showing plastic load/reload and elastic unload, with the corresponding plastic/elastic cyclic shear strain and cumulative plastic volumetric strain

To calculate the cumulative plastic volumetric strain (ϵ_v^P), the increment of plastic volumetric strain during each cycle ($\Delta\epsilon_v^P$) is added to the plastic volumetric strain from the previous cycle (ϵ_{v0}^P):

$$\epsilon_v^P = \Delta\epsilon_v^P + \epsilon_{v0}^P \quad (3.2.8)$$

The cumulative plastic volumetric strain in percent is:

$$\epsilon_v^P(\%) = \epsilon_v^P(100\%) \quad (3.2.9)$$

The total volumetric strain ϵ_v^T is equal to the sum of the plastic volumetric strain and the elastic volumetric strain, where the elastic volumetric strain is directly proportional to the mean effective stress through the bulk modulus of the soil (which can be estimated from the shear modulus and Poisson's ratio). However, it can be assumed that the elastic volumetric strain in a cyclic simple shear test on an unsaturated sand in the funicular regime is approximately equal to zero as the changes in mean effective stress are not expected to be significant. While Rong and McCartney (2020b) did observe changes in mean effective stress, they were within 10% of the mean total stress applied in the experiments.

3.3 Changes in Degree of Saturation during Undrained Shearing

It is assumed that there will be no change between the initial and final volume of water in an undrained specimen during cyclic simple shearing due to the high bulk modulus of water. Saturation is the ratio between water volume and void volume (i.e., void volume is comprised of the total water volume and air volume), therefore the change in saturation due to plastic volumetric compression is linked to the volume change of the pore air voids. By incorporating the pore air volume change in terms of the plastic volumetric strain and initial void ratio, the following relationship for saturation change during cyclic simple shearing can be defined where the volume of solids V_s is assumed to equal 1 (derivation in Appendix A2):

$$S = \frac{V_s e_o S_o}{e_o - (V_s + e_o) \epsilon_v^p} \quad (3.4.1)$$

As the volume of solids, the initial void ratio, and initial degree of saturation are constants, Equation 3.4.1 indicates that the degree of saturation is inversely related to changes in the plastic volumetric strain.

3.4 Estimation of Changes in Pore Air Pressure During Undrained Shearing

A major difference in the presented model compared to UBCSAND is that the air and water pressures are assumed to increase at different rates (surface tension not ignored) whereas UBCSAND assumes the pressures are increasing at constant rates by implementing a bulk stiffness to account for both pressures simultaneously (Seid-Karbasi and Byrne 2006). To account for surface tension, separate equations are derived for air and water pressure generation. The instantaneous bulk modulus of air is assumed to be initially at atmospheric conditions and increase incrementally during undrained cyclic simple shearing. The degrees of saturations considered in this study are in the funicular regime and the pore air voids are assumed to be continuous and connected. Some voids may be water filled, air filled or have partial air and water menisci. To extend the hyperbolic model to include a poromechanical approach, it is assumed that all volumetric compression is a reduction in air volume due to the incompressibility of water and the assumption that no particle crushing occurs to the soil. Air is assumed to be an ideal gas and the temperature of the air-water-soil system is at ambient conditions ($T = 294$ K) with no fluctuation. Incorporating volumetric definitions of the soil's 3-phase diagram into the equations of the Ideal Gas Law, Henry's Law, allows for a derivation to find the pore air pressure change corresponding to a volume change during undrained cyclic simple shearing (derivation in Appendix A1). The relationship between pore air pressure and volumetric strain for a given initial degree of saturation and initial void ratio can be defined as follows:

$$u_a = \frac{(P_{atm} \times \epsilon_v^p * (1 + e_o))}{(h \times S_o \times e_o \times RT + e_o \times (1 - S_o) - \epsilon_v^p * (1 + e_o))} \quad (3.2.9)$$

This pore air pressure equation is an isothermal equation that is comprised of constant values (initial void ratio, initial degree of saturation, Henry's constant, and temperature) and the plastic volumetric strain that will evolve during cyclic shearing. The study of Youd (1971) indicates that

all soils are expected to have compressive plastic volumetric strains occurring during cyclic simple shearing, which implies that that air pressure calculated from Equation 3.2.9 will increase during the course of a cyclic simple shear test. Further, the pressurization of the pore air during cyclic simple shearing is expected to affect the seismic compression in unsaturated sands during earthquakes by leading to a decrease in the mean effective stress according to Equation 2.2.2.

3.5 Estimation of Changes in Pore Water Pressure During Undrained Shearing

The application of the UBCSAND model to unsaturated soils by Seid-Karbasi and Byrne (2006, 2007) and Byrne et al. (2006) assumed that the changes in pore water pressure are equal to the changes in pore air pressure during undrained cyclic shearing of unsaturated soil for simplicity. However, several experimental studies (Unno et al. 2009; Rong and McCartney 2020) found that the pore air and water pressures evolved in different manners during undrained cyclic shearing. The approach followed in this study was to estimate the changes in matric suction from the changes in degree of saturation predicted from Equation 3.4.1, then to use the definition of the matric suction to calculate the pore water pressure from the pore air pressure calculated in Equation 3.2.9. Specifically, the pore water pressure can be calculated from the pore air pressure and matric suction as follows:

$$u_w = u_a - \psi \quad (3.5.2)$$

Use of this equation implies that the water retention in the soil is due primarily to capillarity (Lu and Likos 2004). It is assumed that the thermodynamic state of the soil is constant throughout the duration of cyclic simple shearing as surface tension and capillarity are affected by temperature.

During undrained cyclic shearing, Rong and McCartney (2020b) found that unsaturated sand specimens initially on the primary drying path of the SWRC followed a wetting transient SWRC scanning path having a slope that depended on the initial degree of saturation of the

specimens. Using the relationship between degree of saturation and matric suction, a semi-empirical equation is derived from the soil's SWRC. To predict the changes in the model's matric suction, a log-linear relationship between the saturation and matric suction was defined empirically as follows (derivation in Appendix C):

$$\psi = 10^{\frac{S - (S_0 + m \log_{10} \psi_0)}{-m}} \quad (3.5.1)$$

This equation is only valid for initial degrees of saturation in the funicular regime as shown in Figure 3.5.1. For greater degrees of saturation, a reconsolidation analysis using pore water pressures predicted using the model of Seid-Karbasi and Byrne (2004) is necessary. This is a topic for a future study. Using the model's prediction of matric suction from Equation (3.5.1) and the pore air pressure from Equation 3.2.9, the pore water pressure can be computed.

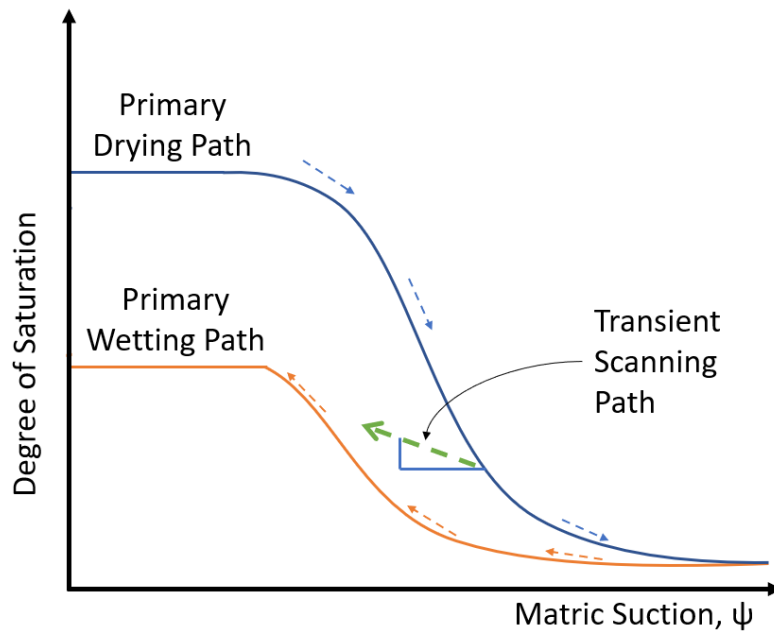


Figure 3.5.1 Schematic of the transient scanning path of the SWRC for a sand specimen initially on the primary drying path.

3.6 Calculation of Effective Stress Changes during Cyclic Shearing

Once the air pressure, saturation and matric suction changes are predicted, the incremental effective stress can now be computed using Lu et al. (2010) equation for effective stress, given as follows using the effective saturation as the effective stress parameter:

$$\sigma'_v = (\sigma_v - u_a) + S_e \psi \quad (3.6.1)$$

Since the cyclic simple shear test is confined to a cylindrical specimen that does not deform radially (no bulging sides) during shearing, K_o conditions are considered to be valid. The effective stress is converted to mean effective stress assuming (K_o) conditions using Poisson's ratio (ν).

$$K_o = \frac{\nu}{1 - \nu} \quad (3.6.2)$$

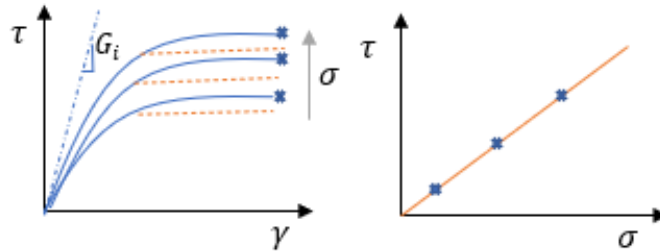
$$\sigma'_m = \left(\frac{1 + 2K_o}{3} \right) \sigma'_v \quad (3.6.3)$$

3.7 Predicting the Evolution in Hydro-Mechanical Variables during Undrained Shearing

The prediction of the volumetric strain during undrained cyclic shearing is closely related to the plastic shear modulus, and it was shown in section 3.2 that the mean effective stress governs the dynamic soil properties through the hyperbolic shear modulus equation. Accordingly, the values of σ'_m calculated during application of the cyclic shear strains in the hysteretic stress-strain curve equations are used to calculate the shear modulus that affect the evolution in cyclic shear stress. The sequence of the model is shown in the flow chart in Figure 3.6.1.

*Establish model relationships:

- $G_i = k_G^e * P_a * \left(\frac{\sigma'_m}{P_a}\right)^{n_e}$
- $G_i^P = k_G^e * \left(\frac{\sigma'_m}{P_a}\right)^{n_e-1}$
- $G^P = G_i^P * \left[1 - \frac{\tau}{\tau_f}\right]^5$



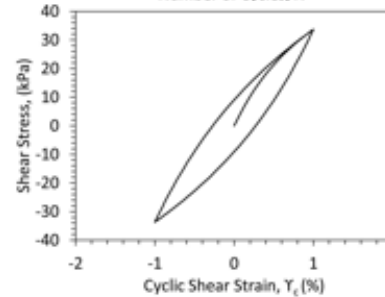
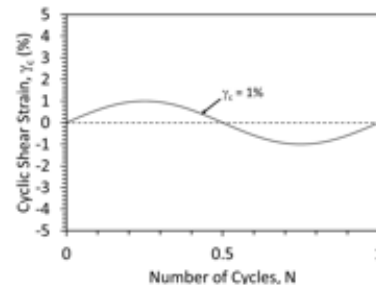
*Use Hysteretic Shear Stress-Strain Equations to establish τ from input strain history:

- γ_c at $f = 1\text{Hz}$ For N cycles
- As $\gamma_e \ll \gamma_p$ neglect, $\gamma = \gamma_p$
- During simple shear: $\Delta\sigma'_m \approx 0$, $\varepsilon_{ve} \approx 0$

Hysteretic Equations:

$$\tau_+ = \left(\frac{\gamma_c + \gamma_{\text{applied}}}{\frac{1}{G_i} + \frac{(\gamma_c + \gamma_{\text{applied}}) * R_f}{2 * \tau_{\text{ult}}}} \right) - \tau_c$$

$$\tau_- = \left(\frac{\gamma_c - \gamma_{\text{applied}}}{\frac{1}{G_i} + \frac{(\gamma_c - \gamma_{\text{applied}}) * R_f}{2 * \tau_{\text{ult}}}} \right) + \tau_c$$



*Use τ to calculate G_p

*Use G_p to calculate γ_p (only on load/reload)

* Use γ_p to calculate ε_v^p

* Use ε_v^p to calculate u_a and S

* Use S and SWRC transient curve to calculate ψ

* Use S , ψ , u_a to calculate σ'_m for next cycle

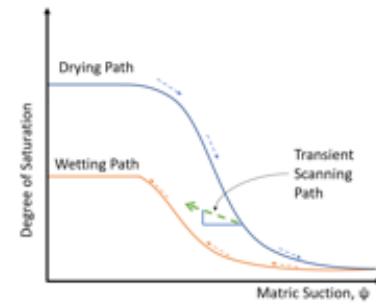


Figure 3.7.1 Flow chart for the semi-empirical hyperbolic model with hydro-mechanical coupling for seismic compression in the funicular regime

4 Data

4.1 Sand Specimens in Cyclic Simple Shear Database

The sand used in the available experimental database provided by Rong and McCartney (2020a, 2020b, 2021a, 2020b) is classified as a well-graded sand (SW) according to the Unified Soil Classification System (USCS). The sand has a mean particle diameter (D_{50}) and an effective particle diameter (D_{10}) of 0.8 and 0.2 mm, respectively. The sand is reported to have a coefficient of uniformity (C_u) and curvature (C_c) of 6.1 and 1.0, respectively. The maximum and minimum void ratios are 0.853 and 0.371, respectively. Figure 4.1.1 shows the particle size distribution curve for the SW sand.

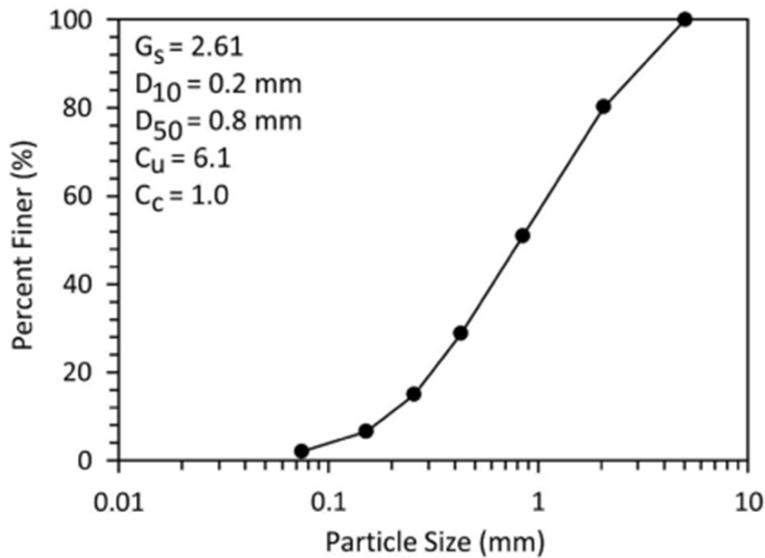


Figure 4.1.1 Particle size distribution curve for the SW sand (Rong and McCartney 2020b).

To prepare the specimens for cyclic simple shear tests, the sand was funneled into the specimen housing to reach a target relative density of 0.45 without tamping. The primary wetting and drying path of the SWRC were obtained using the hanging column approach, and the data points fitted with the van Genuchten (1980) SWRC model as shown in Figure 4.1.2 (Rong and McCartney 2020b).

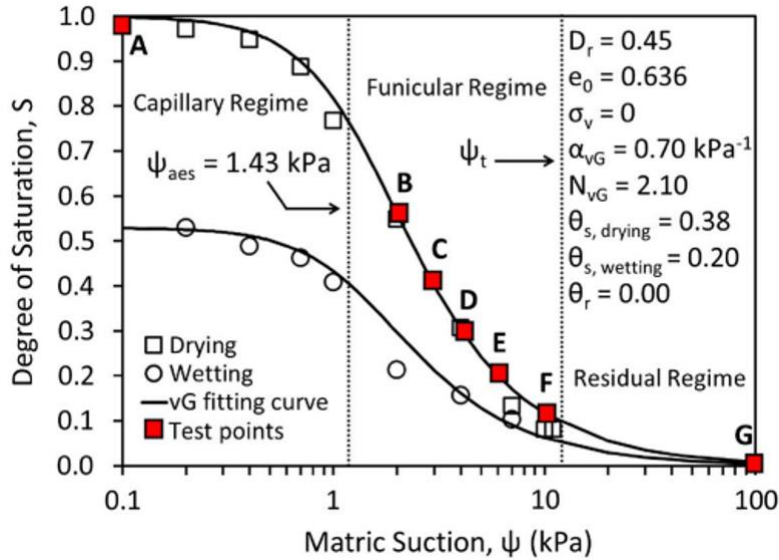


Figure 4.1.2 SWRC for the sand specimen at $D_r = 0.45$ (Rong and McCartney 2020b)

Rong and McCartney (2020b) used the hanging column technique similar to the approach used by Tatsuoka et al. (1979) to desaturate initially saturated sand specimens to reach different initial degrees of saturation in the funicular regime of the SWRC. During initial application of a target suction, the water outflow was tracked using the hanging column and the pore water pressure was monitored using a tensiometer until the target matric suction was reached and held for approximately 30 minutes, at which point the specimen is assumed to be at hydraulic equilibrium and ready for cyclic simple shearing (Rong and McCartney 2020b). They performed tests in both drained and undrained conditions. Rong and McCartney (2019, 2020b) reported the results from drained cyclic shearing tests having a range of different applied shear strain amplitudes (0.3, 1.0, 5, 10) for 200 to 1000 cycles. Rong and McCartney (2020a, 2020b) reported the results from undrained cyclic shearing tests applied shear strain of 1% at a strain rate of 0.833 %/min for a duration of 200 cycles. The drained tests were useful to define the backbone curve as they were performed to higher shear strain amplitudes, but this study is primarily focused on the seismic

compression during undrained shearing. Accordingly, in this thesis only selected drained tests are reported while several undrained tests are reported.

The cyclic simple shear tests reported by Rong and McCartney (2020a, 2020b, 202c) were performed in a modified NGI cyclic simple shear apparatus that has a wire-reinforced membrane that does not permit radial expansion and therefore the volumetric strain during shearing can be measured by the changes to the height of the cylindrical specimen. The schematic of the specimen housing used in the modified NGI cyclic simple shear device is shown in in Figure 4.1.3.

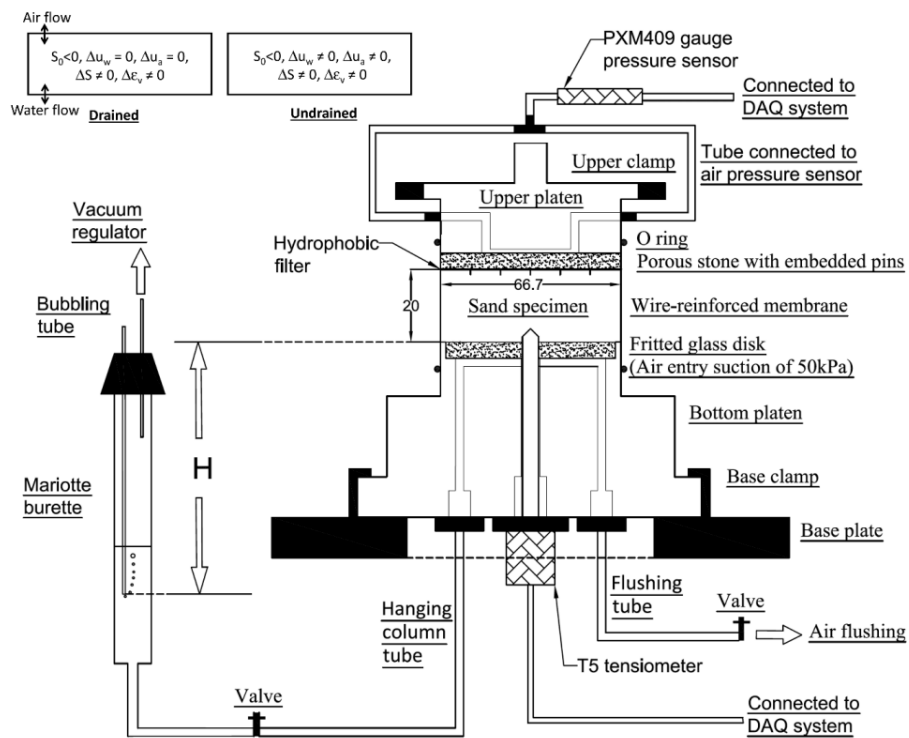


Figure 4.1.3 Schematic view of the specimen housing in the modified NGI simple shear device used for drained and undrained experiments (dimensions in mm) (Rong and McCartney 2021a).

The cylindrical sand specimens tested by Rong and McCartney (2020a, 2020b, 2021a) had a height of approximately 20 mm and a 66.7 mm diameter. The resulting height to diameter ratio was 0.3 which was less than the maximum value of 0.4 defined by ASTM D6528. All specimens regardless of drained or undrained were subjected to an applied vertical stress of 50kPa to recreate

loading conditions of a transportation design backfill during seismic shaking. A NGI simple shear device was modified by Rong and McCartney (2021a) to permit cyclic simple shearing of a soil from left to right by encapsulating the specimen in a cylindrical housing that permits for shear stresses in both directions to be applied to the top of the device. Rong and McCartney (2021a) also updated the NGI simple shear ports for sensors to record internal pore pressures during testing. The data presented in this thesis was tested using a modified NGI apparatus incorporated with a special bottom platen which transmits water from a hanging column and permits port access for tensiometer measurements (Rong and McCartney 2021a).

4.2 Drained Monotonic Simple Shear Data

The testing protocol for the fully drained experimental data was kept at a constant matric suction, valves on top/bottom of housing were left open and the ventilation permitted air flow thereby reflecting the pore air pressures at atmospheric conditions. As cyclic shearing was applied to the specimen, volumetric contraction commenced which induced the outflow of water. Shearing during the experiment was reported by Rong and McCartney (2020b) to be considered slow enough to allow for the dissipation of any generated excess pore water pressure. Several drained data sets were collected at constant matric suctions: 4kPa, 6kPa and 10kPa. Drained shearing tests with a constant suction of 4 kPa with cyclic shear strain amplitudes of 1% and 3% strain were used in the calibration of the backbone curve parameters, and the results shown in Figure 4.2.1 indicate that the shear-stress strain curves from the other tests were generally in good agreement. It should be noted that even when extrapolating this curve to 5% shear strain, the specimen had still not reached failure, which is expected to occur at a shear stress of approximately 63-65 kPa for these unsaturated conditions based on the shear strength parameters reported by Zheng et al. (2019).

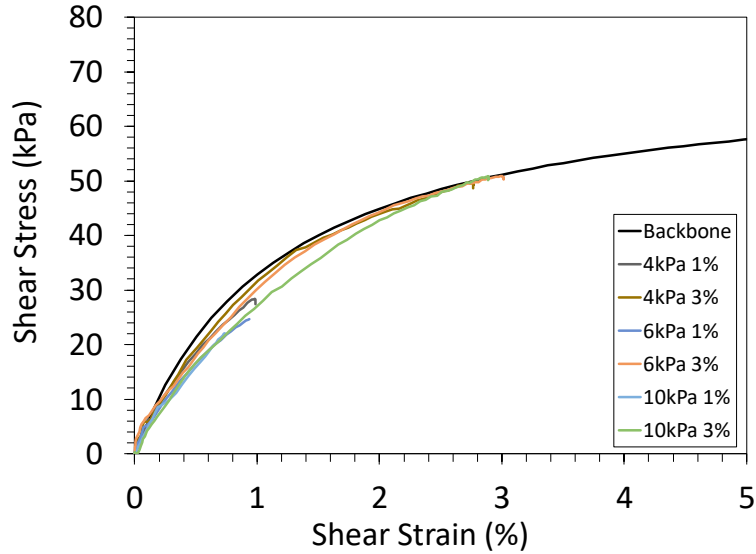


Figure 4.2.1 Backbone curves for drained sand ($D_r = 0.45$) at various constant suctions (4 kPa, 6 kPa, 10 kPa) and different shear strain amplitudes (1%, 3%) (Rong and McCartney 2020a)

Table 1: Summary of initial testing conditions and final shear strain

Specimen No.	Initial Matric Suction ψ_o (kPa)	Initial Saturation S_o	Target Strain Range γ_n (%)	Initial Achieved Strain Range γ_o (%)	Final Achieved Strain Range γ_f (%)
C-3	3.96	0.31	3.00 : (-3.00)	2.75 : (-2.86)	2.71 : (-3.01)
C-2	3.87	0.31	1.00 : (-1.00)	0.98 : (-1.06)	0.91 : (-1.13)
D-3	5.95	0.20	3.00 : (-3.00)	3.01 : (-2.64)	2.99 : (-2.83)
D-2	5.93	0.20	1.00 : (-1.00)	0.94 : (-0.95)	1.58 : (-0.22)
E-3	10.03	0.12	3.00 : (-3.00)	2.89 : (-2.76)	3.24 : (-2.34)
E-2	10.15	0.11	1.00 : (-1.00)	0.74 : (-1.20)	0.77 : (-1.10)

Note: Strain rate for all tests: 0.833%/min; Initial and final achieved shear strain ranges were measured for $N = 1$ and $N = 200$, respectively.

4.3 Undrained Cyclic Simple Shear Data

The testing protocol for the undrained experimental data had a gauge air pressure transducer attached to the top of the housing platen which blocked air ventilation and allowed for the pore air pressure to be measured during shearing. Once the sand specimen reached its target matric suction, the bottom housing valve was closed to water flow which caused excess pore water

pressures to increase during shearing. The initial conditions for the undrained experimental data sets are summarized in Table 2.

Table 2: Summary of initial conditions of undrained cyclic simple shear experiments of Rong and McCartney (2020) that were modeled in this study

S_o	(unitless)	0.117	0.2	0.3	0.4	0.558
ψ_o	(kPa)	10	6	4	3	2

Table 3: Summary of initial testing conditions and final shear strain for the undrained cyclic simple shear experiments (after Rong and McCartney 2020b).

Specimen No.	Initial Matric Suction ψ_o (kPa)	Initial Saturation S_o	Target Strain Range γ_{rn} (%)	Initial Achieved Strain Range γ_{ro} (%)	Final Achieved Strain Range γ_{rf} (%)
Set 1	1.99	0.560	1.00 : (-1.00)	0.98 : (-1.00)	0.86 : (-0.95)
Set 2	1.99	0.560	1.00 : (-1.00)	0.94 : (-0.82)	1.19 : (-0.69)
Set 1	2.99	0.400	1.00 : (-1.00)	0.80 : (-0.89)	0.61 : (-1.22)
Set 2	2.99	0.400	1.00 : (-1.00)	0.88 : (-0.81)	0.51 : (-1.16)
Set 1	3.99	0.300	1.00 : (-1.00)	0.85 : (-0.94)	0.68 : (-1.04)
Set 2	3.99	0.300	1.00 : (-1.00)	0.88 : (-0.81)	0.51 : (-1.16)
Set 1*	6.00	0.206	1.00 : (-1.00)	0.89 : (-1.08)	0.83 : (-1.03)
Set 2	5.99	0.206	1.00 : (-1.00)	0.91 : (-0.72)	0.87 : (-0.82)
Set 1	9.99	0.118	1.00 : (-1.00)	1.10 : (-0.81)	1.03 : (-0.94)
Set 2	10.00	0.117	1.00 : (-1.00)	0.89 : (-1.04)	0.78 : (-1.18)
Set 1*	100.00	0	1.00 : (-1.00)	0.92 : (-1.03)	1.00 : (-0.88)
Set 2*	100.00	0	1.00 : (-1.00)	0.92 : (-0.94)	0.78 : (-1.06)

Notes: The dry specimen is assumed to have a suction value of 100 kPa; Initial and final achieved shear strain ranges were measured for N = 1 and N = 200, respectively; *Unpublished data

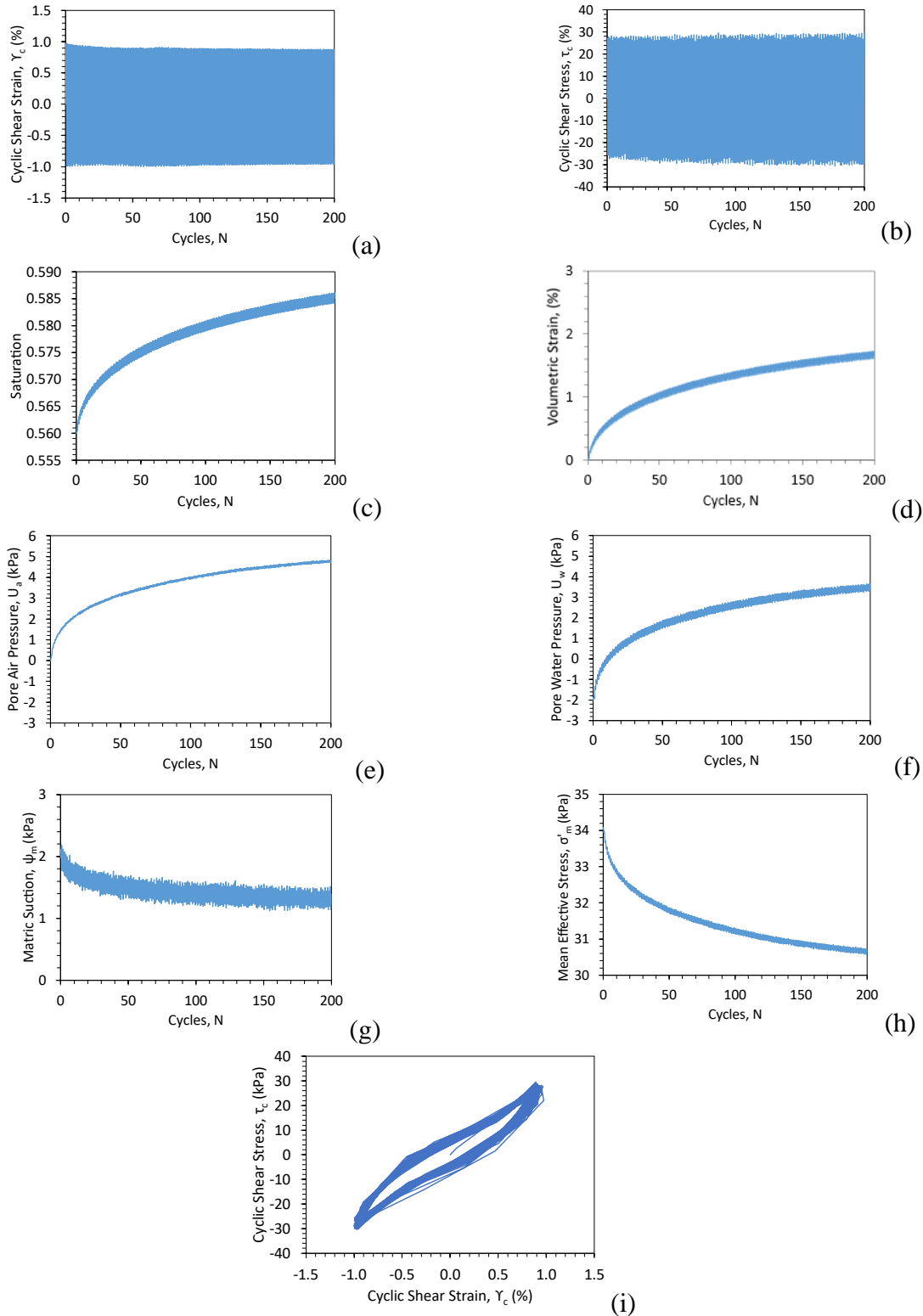


Figure 4.3.1 Data Set 1 $S=0.56$ Time series of (a) Shear strain (b) shear stress (c) Degree of saturation (d) Volume change (e) Pore air pressure change (f) Pore water pressure change (g) Matric suction change (h) Mean effective stress change (i) Cyclic shear stress and cyclic shear strain

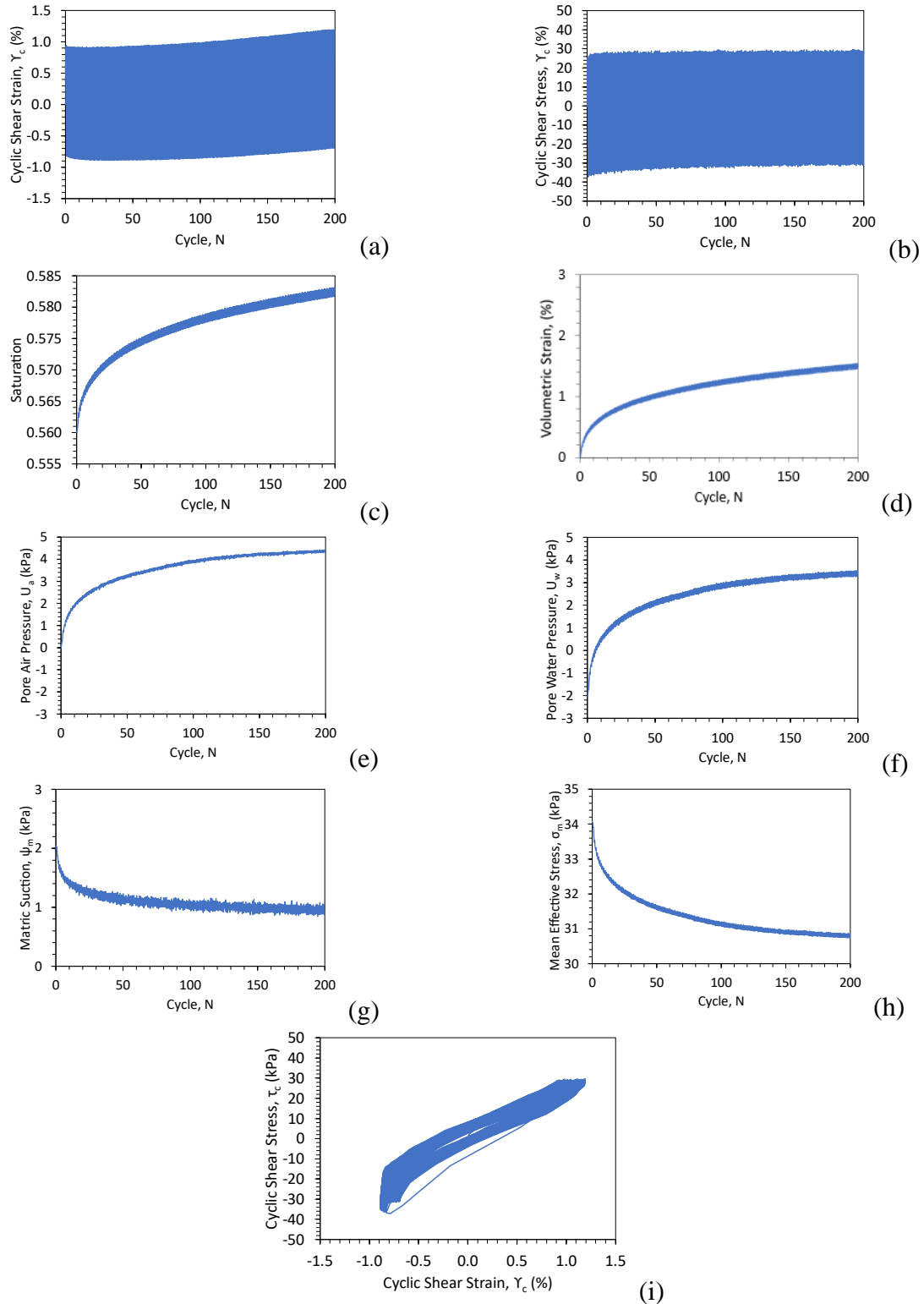


Figure 4.3.2 Data Set 2 $S=0.56$ Time series of (a) Shear strain (b) shear stress (c) Degree of saturation (d) Volume change (e) Pore air pressure change (f) Pore water pressure change (g) Matrix suction change (h) Mean effective stress change (i) Cyclic shear stress and cyclic shear strain

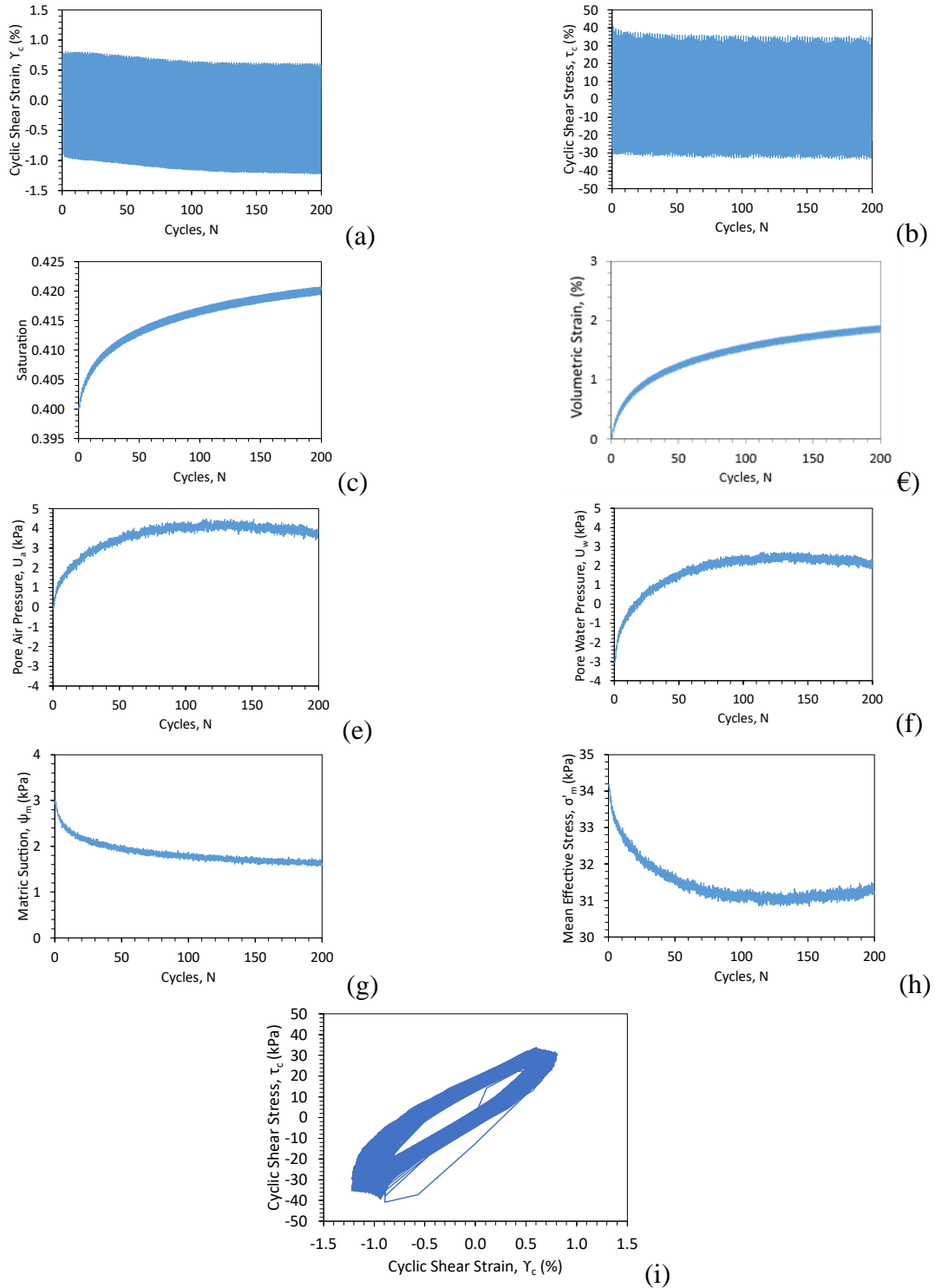


Figure 4.3.3 Data Set 1 $S=0.4$ Time series of (a) Shear strain (b) shear stress (c) Degree of saturation (d) Volume change (e) Pore air pressure change (f) Pore water pressure change (g) Matrix suction change (h) Mean effective stress change (i) Cyclic shear stress and cyclic shear strain

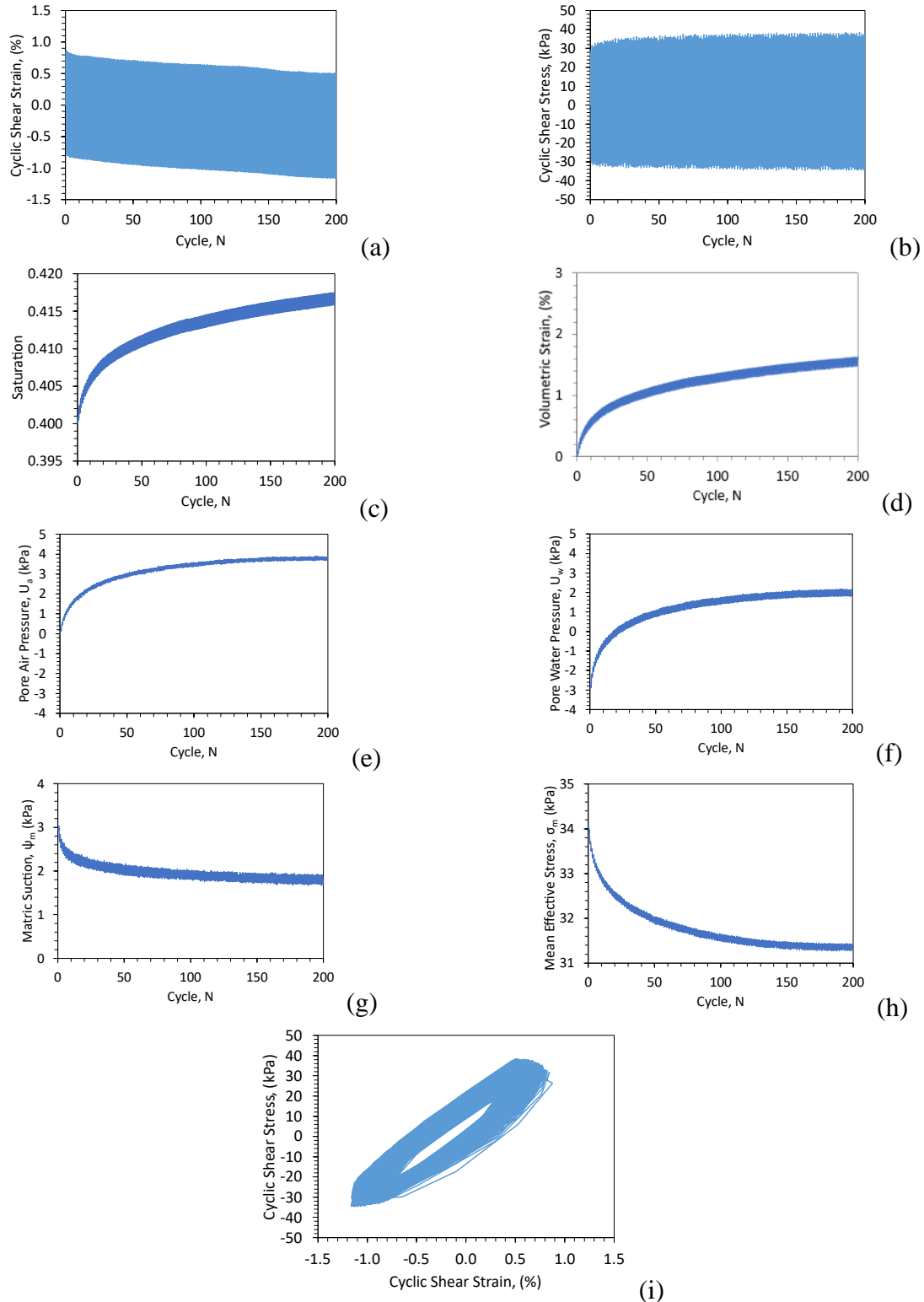


Figure 4.3.4 Data Set 2 $S=0.4$ Time series of (a) Shear strain (b) shear stress (c) Degree of saturation (d) Volume change (e) Pore air pressure change (f) Pore water pressure change (g) Matric suction change (h) Mean effective stress change (i) Cyclic shear stress and cyclic shear strain

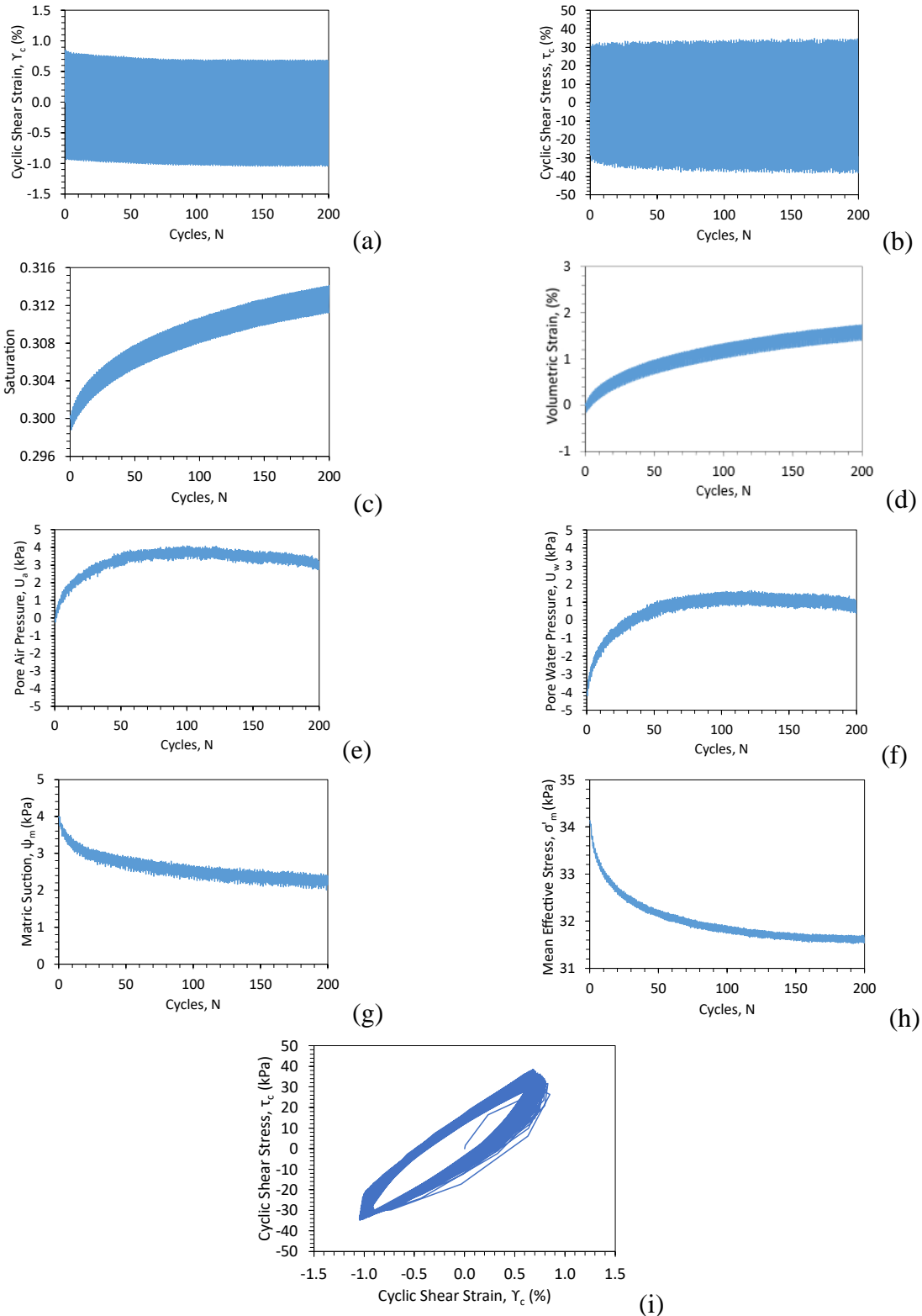


Figure 4.3.5 Data Set 1 $S=0.3$ Time series of (a) Shear strain (b) shear stress (c) Degree of saturation (d) Volume change (e) Pore air pressure change (f) Pore water pressure change (g) Matric suction change (h) Mean effective stress change (i) Cyclic shear stress and cyclic shear strain

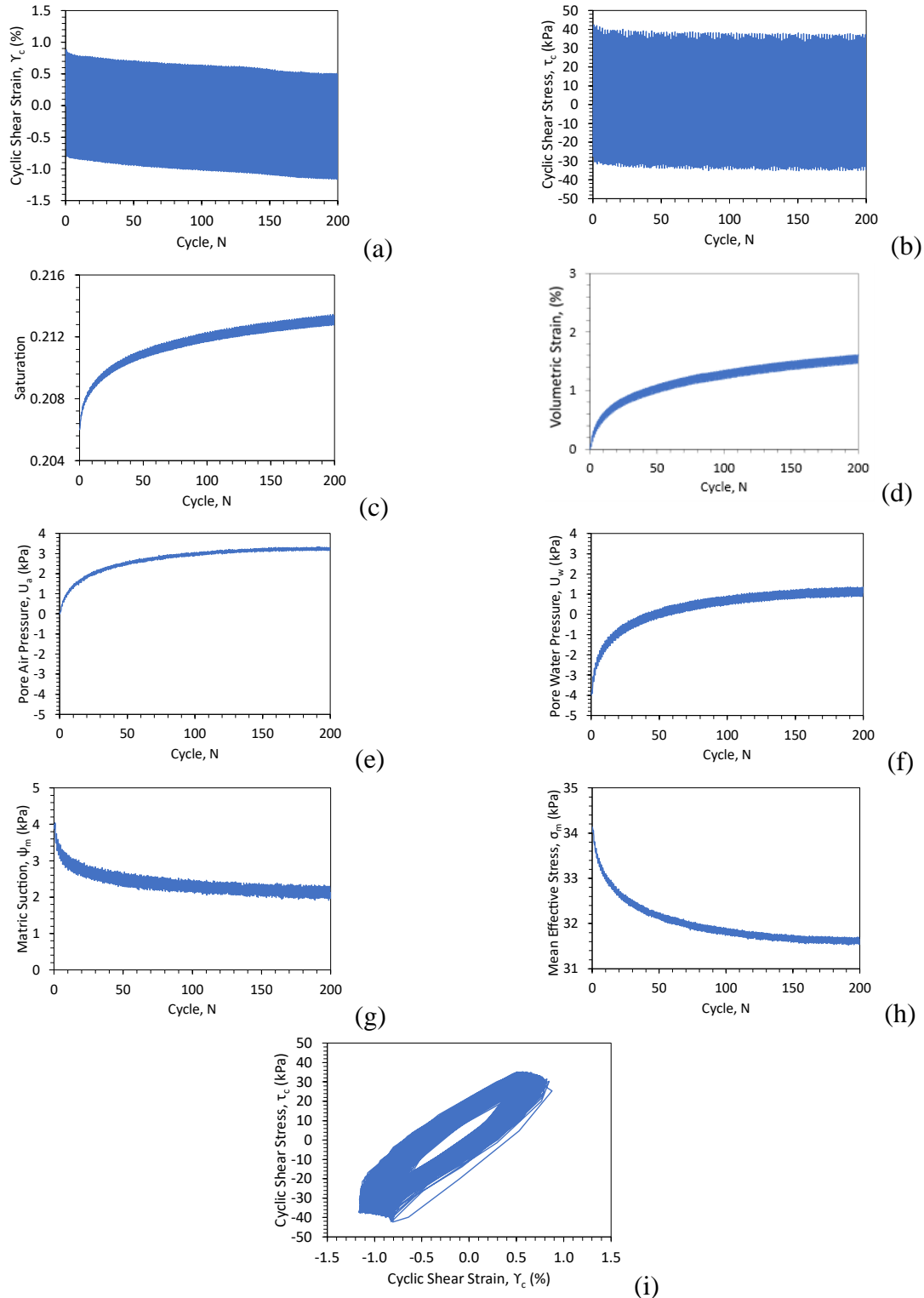


Figure 4.3.6 Data Set 2 $S=0.3$ Time series of (a) Shear strain (b) shear stress (c) Degree of saturation (d) Volume change (e) Pore air pressure change (f) Pore water pressure change (g) Matric suction change (h) Mean effective stress change (i) Cyclic shear stress and cyclic shear strain

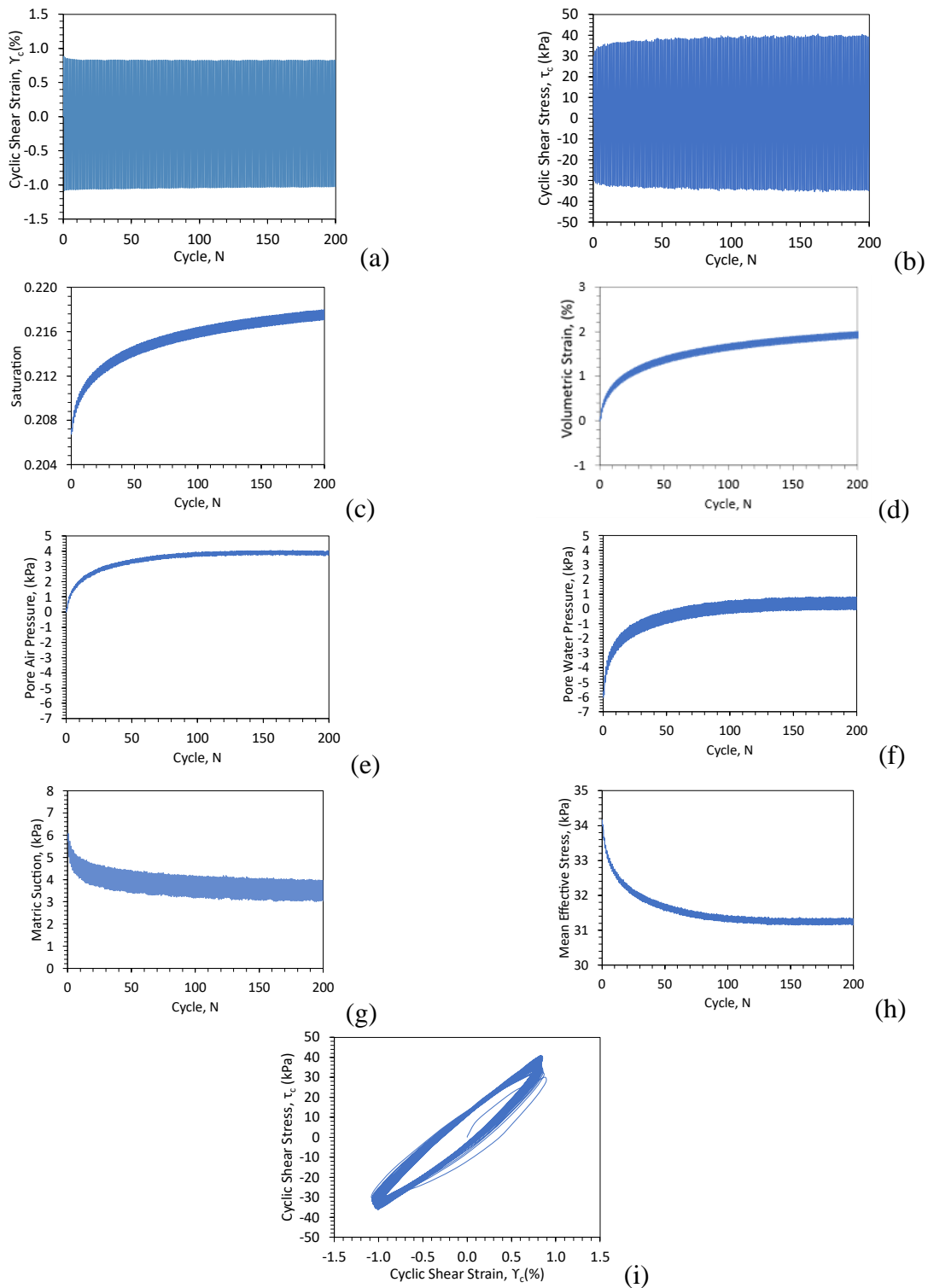


Figure 4.3.7 Data Set 1* S=0.206 Time series of (a) Shear strain (b) shear stress (c) Degree of saturation (d) Volume change (e) Pore air pressure change (f) Pore water pressure change (g) Matrix suction change (h) Mean effective stress change (i) Cyclic shear stress and cyclic shear strain

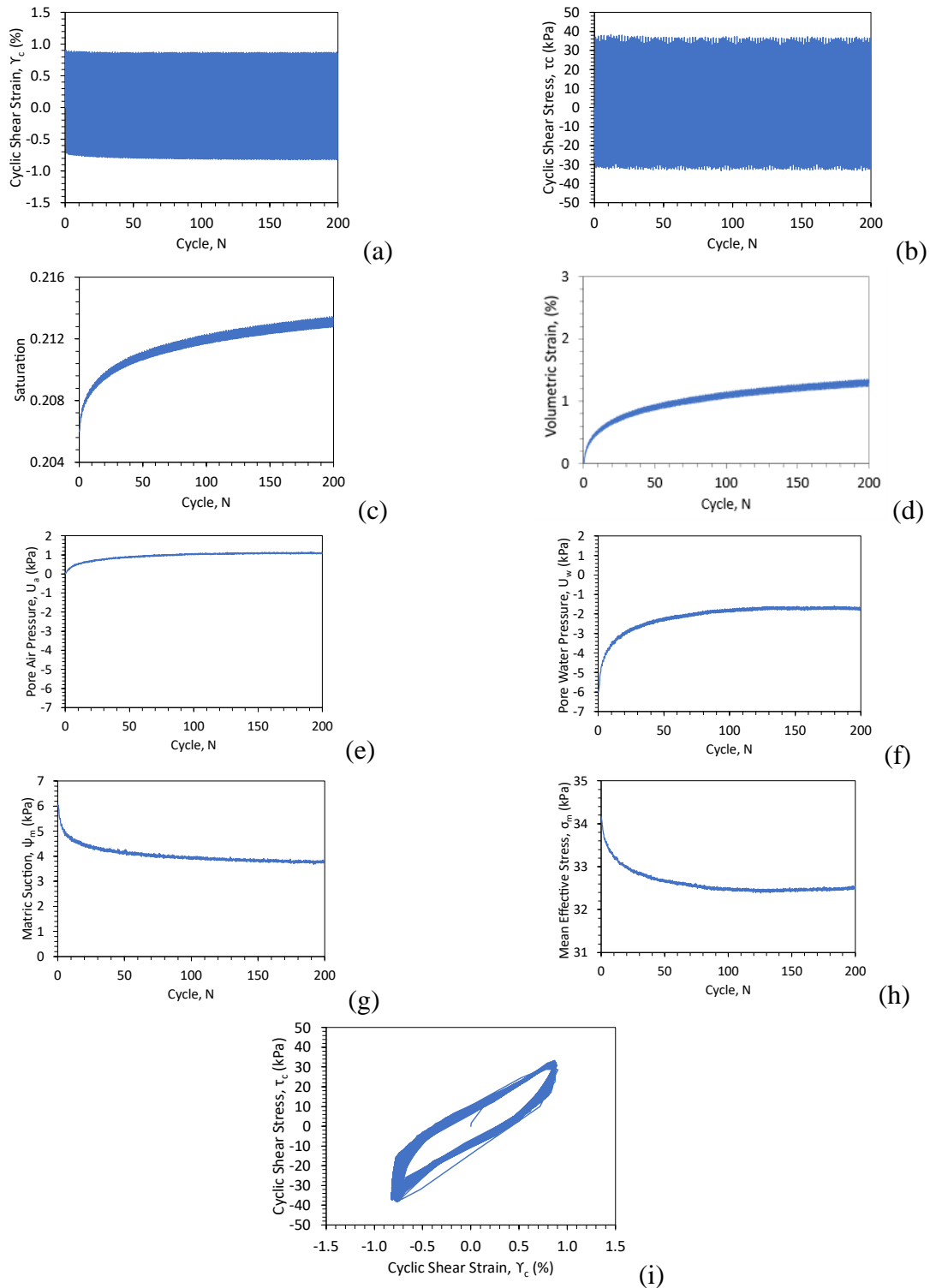


Figure 4.3.8 Data Set 2 $S=0.2$ Time series of (a) Shear strain (b) shear stress (c) Degree of saturation (d) Volume change (e) Pore air pressure change (f) Pore water pressure change (g) Matrix suction change (h) Mean effective stress change (i) Cyclic shear stress and cyclic shear strain

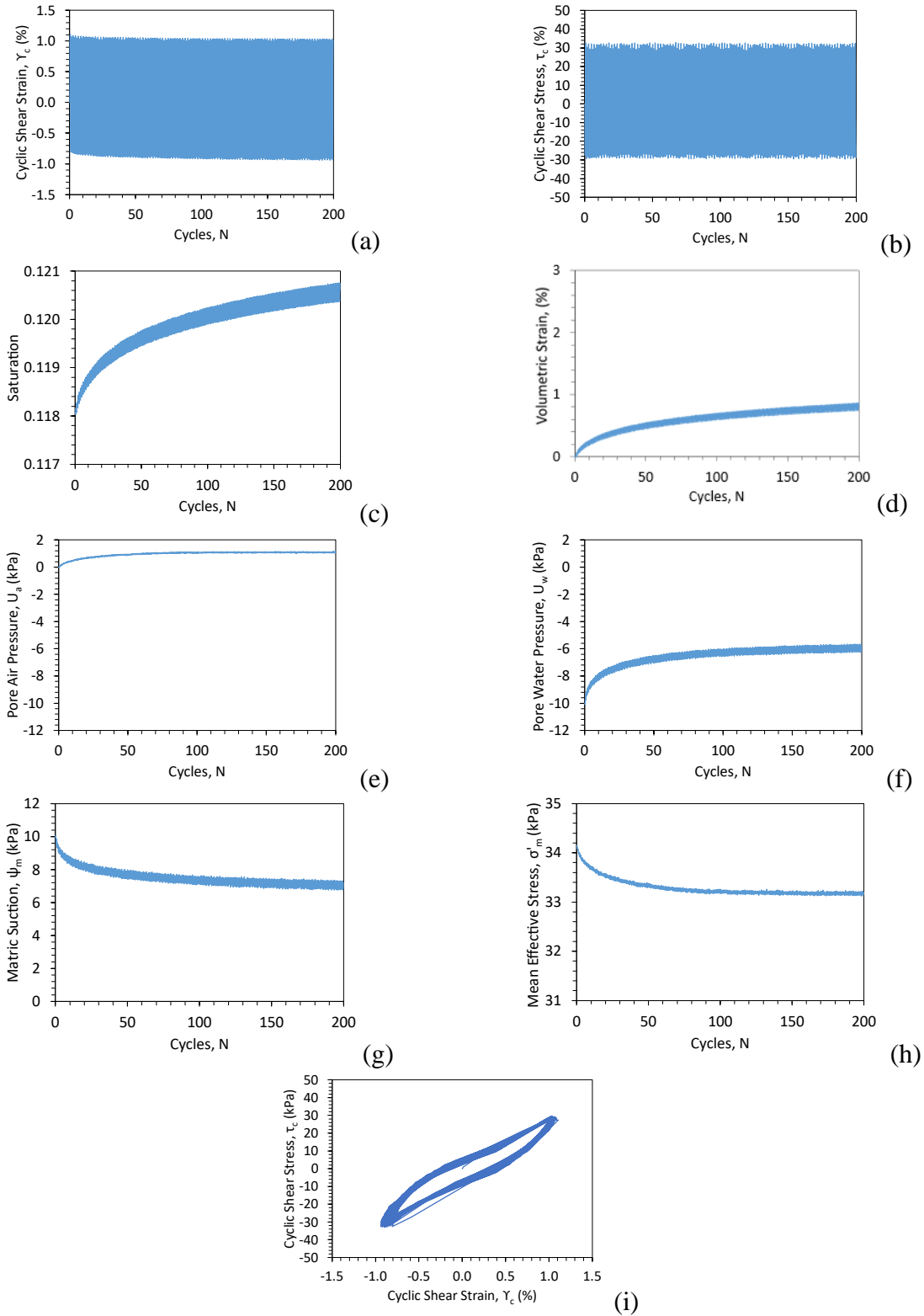


Figure 4.3.9 Data Set 1 $S=0.118$ Time series of (a) Shear strain (b) shear stress (c) Degree of saturation (d) Volume change (e) Pore air pressure change (f) Pore water pressure change (g) Matrix suction change (h) Mean effective stress change (i) Cyclic shear stress and cyclic shear strain

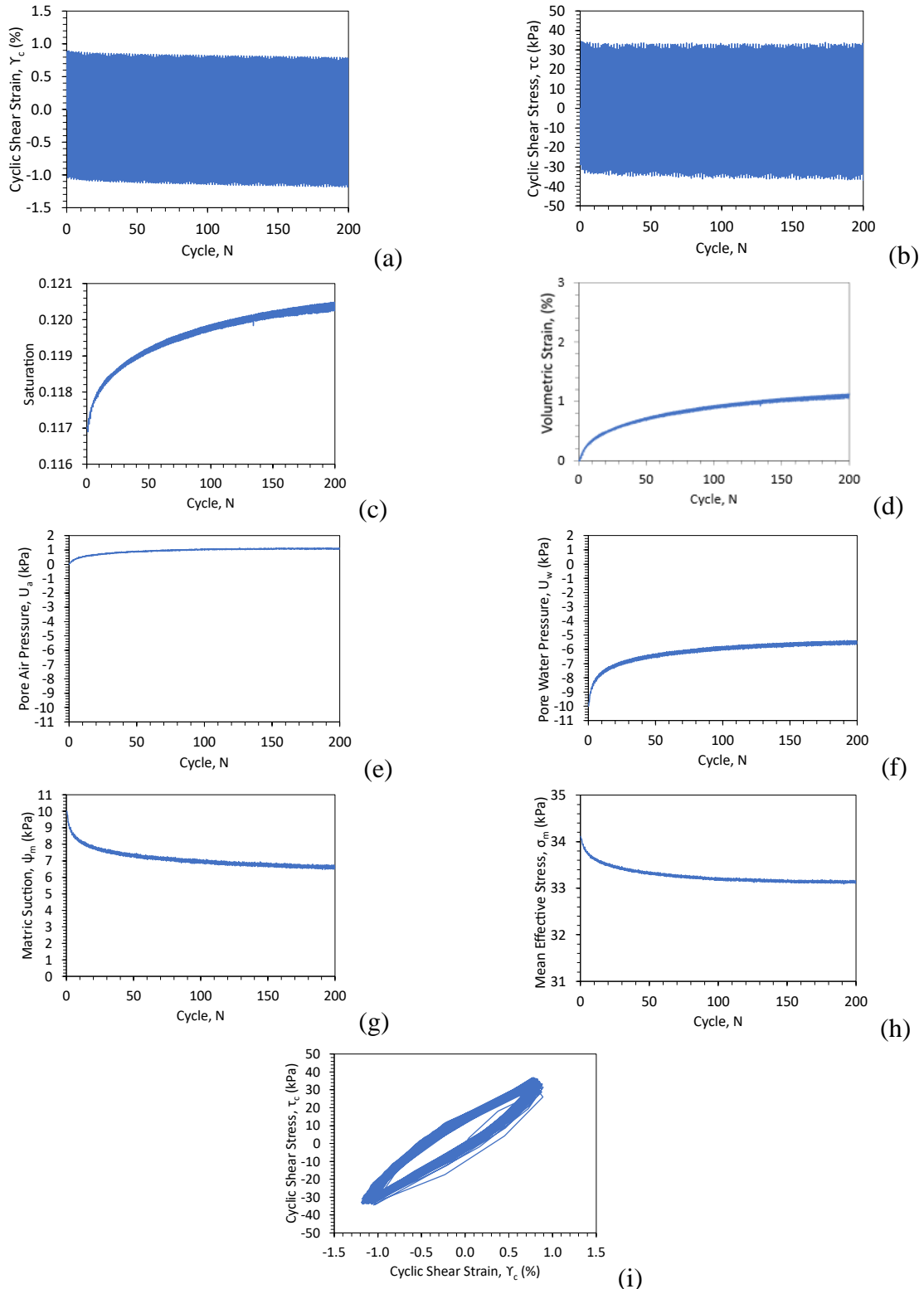


Figure 4.3.10 Data Set 2 $S=0.117$ Time series of (a) Shear strain (b) shear stress (c) Degree of saturation (d) Volume change (e) Pore air pressure change (f) Pore water pressure change (g) Matrix suction change (h) Mean effective stress change (i) Cyclic shear stress and cyclic shear strain

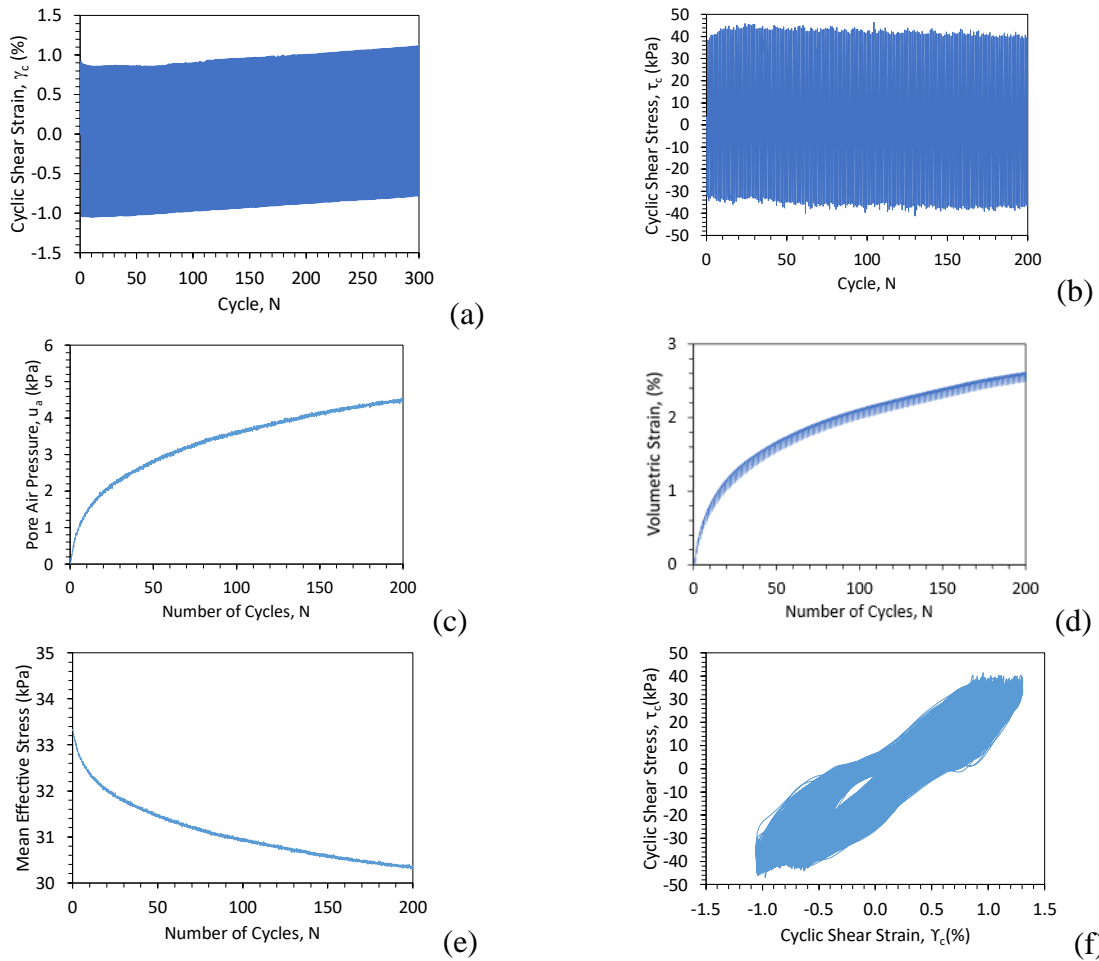


Figure 4.3.11 Data Set 1* S=0 DRY (a) Shear strain time series (b) shear stress time series (c) Volume change time series (d) Pore air pressure change time series (e) Mean effective stress change time series (f) Cyclic shear stress and cyclic shear strain loops

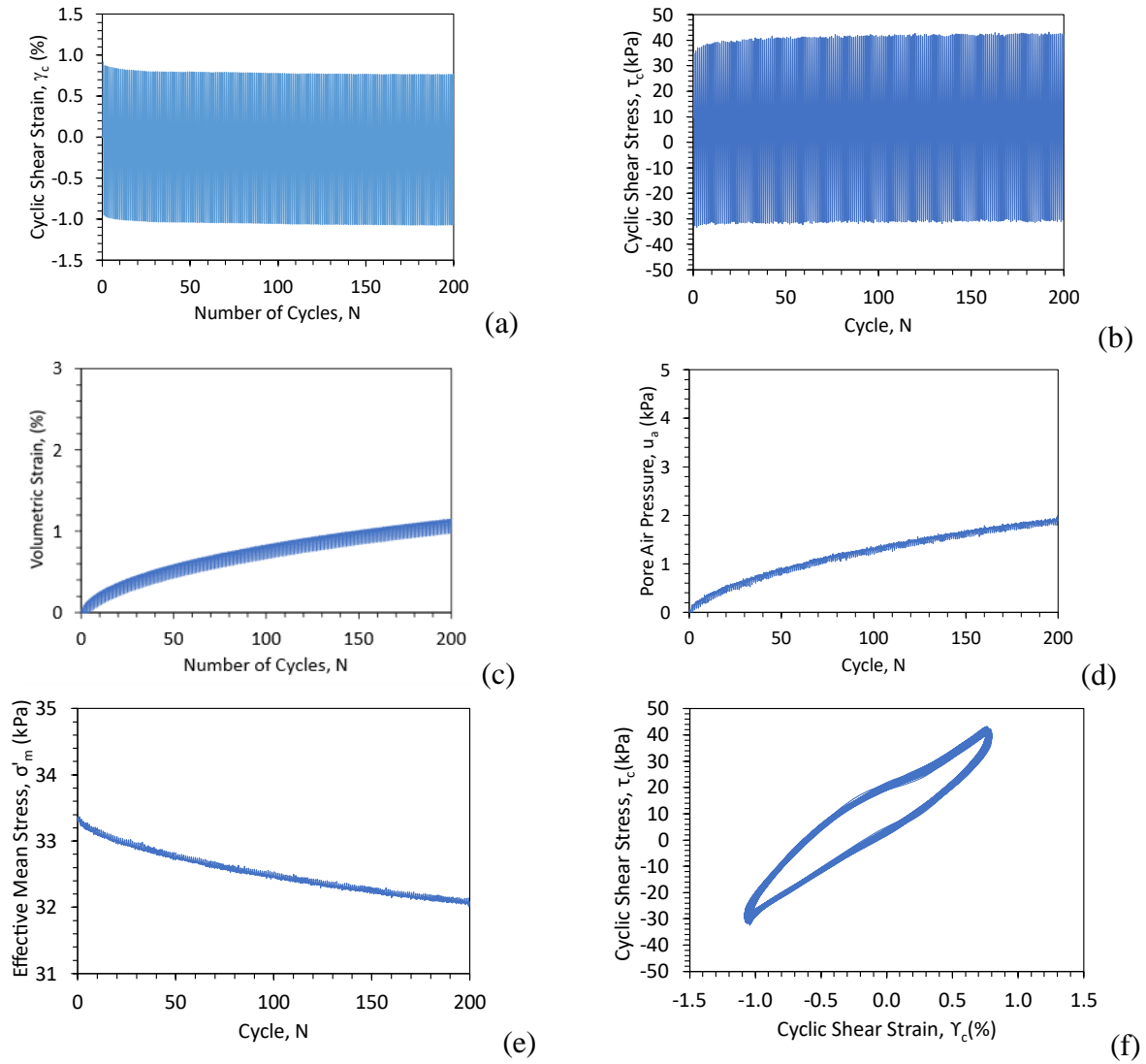


Figure 4.3.12 Data Set 2* S=0 DRY (a) Shear strain time series (b) shear stress time series (c) Volume change time series (d) Pore air pressure change time series (e) Mean effective stress change time series (f) Cyclic shear stress and cyclic shear strain loops

5 Model Calibration

5.1 Calibration of Backbone Curve from Drained Shearing of Unsaturated Sand

While the focus of this thesis is on the prediction of the seismic compression during undrained cyclic simple shearing, the data available from undrained cyclic simple shear tests performed by Rong and McCartney (2020b) only included tests that were performed to a shear strain of 1%. However, Rong and McCartney (2020a) performed drained cyclic simple shear tests on sands in the same conditions but to higher shear strains. To calibrate the parameters of the backbone shear stress-strain curve, data were used from two drained cyclic simple shear tests on sand at a relative density of 45%, a vertical total stress of 50 kPa, and an initial degree of saturation of 0.3 (corresponding to initial matric suction values of 4 kPa) performed to shear strains of 1% and 3% shear strains. Two sets of data were used to ensure that the calibration was a good match to both low and high strain values. The experimental data from each of the tests is shown in Figure 5.1.2 and 5.1.3 in both natural scales and a transformed scale. The transformed scale was used to identify the slope a and intercept b that can be used to identify the hyperbolic model parameters G_i and τ_{ult} as described in Figure 5.1.1.

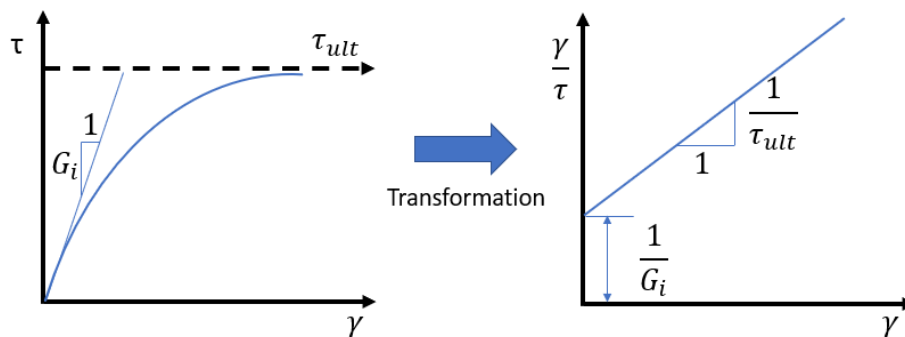


Figure 5.1.1 Linear transformation of hyperbolic shear stress-strain relationship.

The calibrated model parameters are summarized in Table 4 for the two tests, along with the average value of the parameters used in future model predictions. The shear stresses at failure τ_f in Table 4 was determined from the friction angle of this sand of 51.3° reported by Zheng et al. (2019) based on triaxial compression tests on dry sand and the vertical effective stress corresponding to the initial conditions in the specimens. The critical volume friction angle was assumed to be equal to 34° , although further laboratory tests are necessary to better quantify this value. The reduction factors were defined as the ratio of the shear stresses at failure τ_f and the ultimate shear stress from the hyperbolic fitting τ_{ult} , and an average value of $R_f = 0.9$ was used in future predictions. Although only one vertical effective stress was available for calibration of the model in the data presented by Rong and McCartney (2020a), the variation in shear modulus with normal stress could not be fully investigated. Accordingly, a value of $n = 0.5$ was used in the calibration (Duncan et al. 1980).

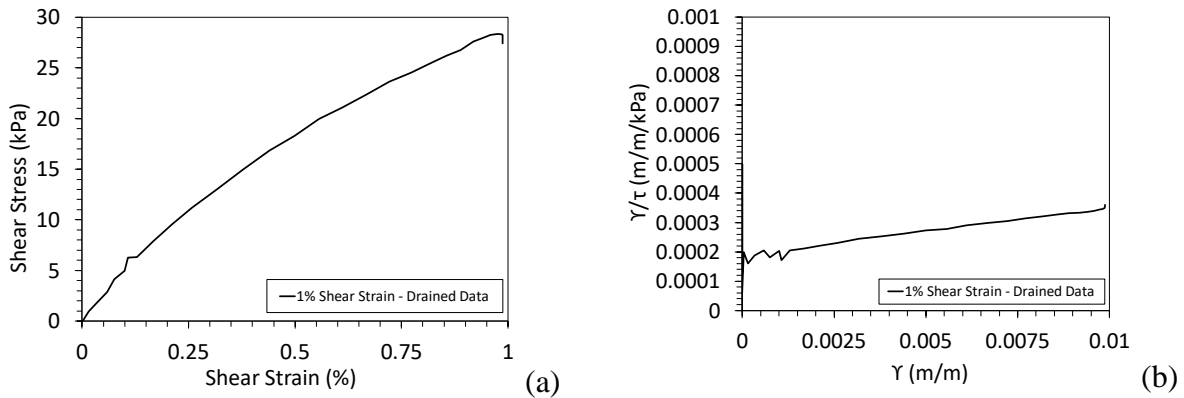


Figure 5.1.2 Hyperbolic fitting process for drained test to 1% shear strain: (a) Monotonic loading to 1% shear strain (b) Linearization of curve to find hyperbolic parameters

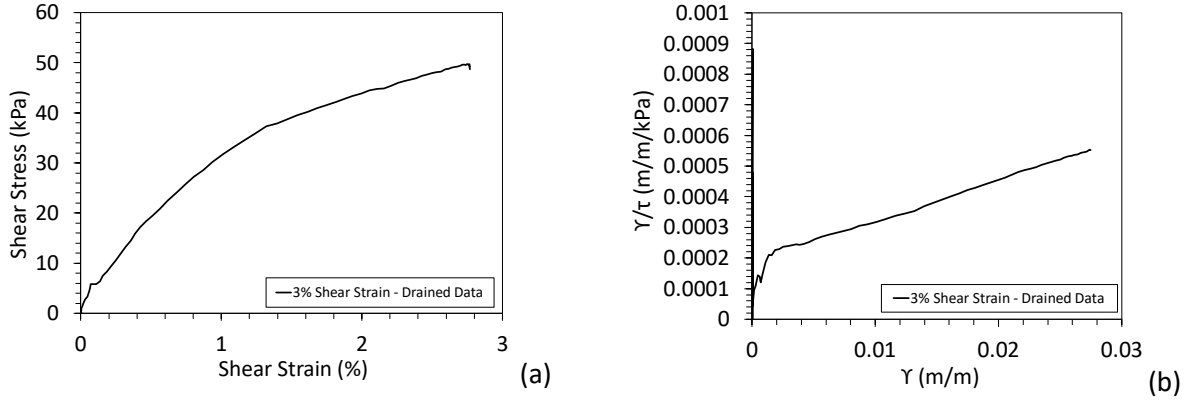


Figure 5.1.3 Hyperbolic fitting process for drained test to 3% shear strain: (a) Monotonic loading at 3% shear strain; (b) Linearization of curve to find hyperbolic parameters

Table 4: Calibrated hyperbolic model parameters for drained tests at a constant suction of 4 kPa performed to 1% and 3% shear strain

Strain amplitude	Initial Shear Modulus	Ultimate Shear Stress	Shear Stress at Failure	Reduction Factor	Shear Modulus Number	Shear Modulus Exponent
	$G_i = 1/a$	$\tau_{ult} = 1/b$	τ_f	R_f	k_G^e	n_e
(%)	(kPa)	(kPa)	(kPa)	(unitless)	(unitless)	(unitless)
1	5950	68.89	63.91	0.9277		
3	5810	72.52	63.91	0.8813		
Average	-	-	-	0.9	100	0.5

A comparison between the calibrated backbone curve and the hysteretic shear stress-strain curves and the experimental curves from the drained cyclic simple shear tests to shear strains of 1% and 3% is shown in Figure 5.1.4. A good match was observed between the calibrated and experimental curves. In this figure, the backbone curve is approaching the shear stress at failure at a shear strain of 10%. However, the test at 3% cyclic shear strain has a slightly steeper stress-strain loop upon application of negative shear strains, with maximum shear stresses close to the value at failure. When cyclic shear stress amplitude is close to the value at failure, there is a likelihood for creep or cyclic degradation that could lead to complex behavior. Fortunately, all of the undrained

cyclic simple shear tests performed by Rong and McCartney (2021b) were performed at a cyclic shear strain amplitude of approximately 1% and are well below the shear stress at failure.

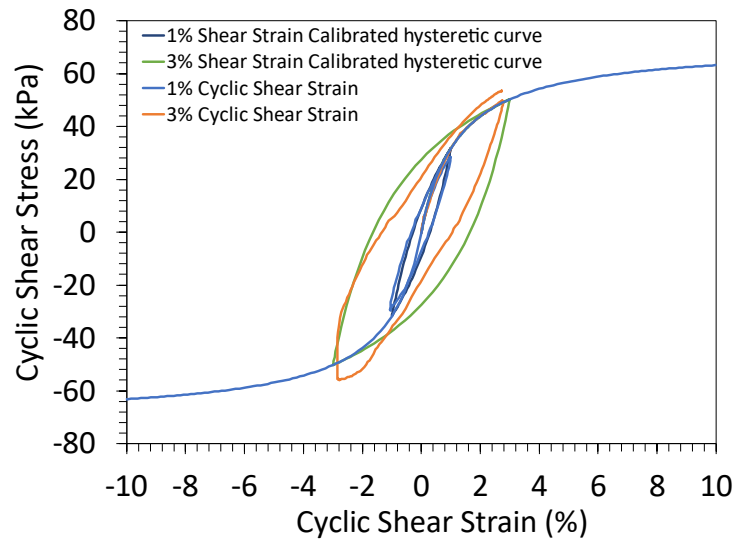


Figure 5.1.4 Comparison of the calibrated backbone and hysteretic shear stress-strain curves with the experimental data for $S_0 = 0.3$ and $s_v = 50$ kPa from Rong and McCartney (2020a)

During each cycle of shearing, plastic shear strains will occur during loading and reloading. Accordingly, plastic volumetric strains will also be generated. This means that the model parameters governing the evolution in the plastic shear strain during cyclic shearing are those governing the shape of the hysteretic shear stress-strain curve. Similarly, the degree of saturation can be directly calculated from the volumetric strain using phase relationships without the need for additional model parameters. Similarly, the pore air pressure model developed in Chapter 3 and Appendix A2 did not include additional parameters beyond the initial conditions of the sand specimen and those necessary to predict the plastic volumetric strain.

5.2 Calibration of Pore Water Pressure Generation Model

Different from the model for the pore air pressure generation, the model for the pore water pressure generation depends on the shape of the transient SWRC scanning paths for specimens with different initial degrees of saturation. An interesting aspect from evaluation of the

experimental results of Rong and McCartney (2020b) indicates that the slope of the transient changes in degree of saturation and matric suction will change during cyclic shearing, with greater changes for specimens with higher initial degrees of saturation, as shown in Figure 5.2.1.

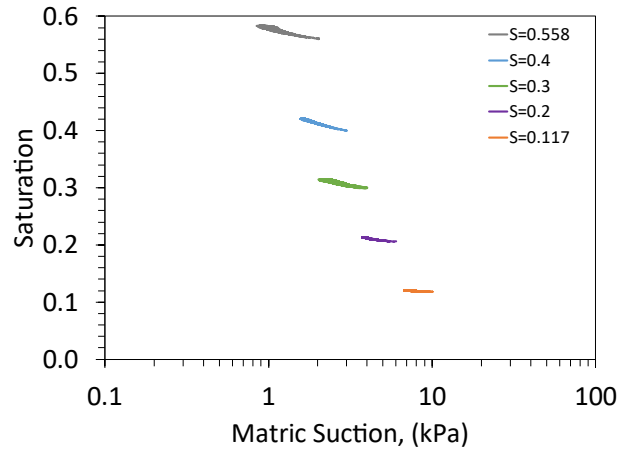


Figure 5.2.1 Transient SWRC wetting paths of undrained cyclic shear data set 1 after 200 cycles.

Since the volumetric compression data is changing most rapidly at the onset of cycling, the first 1.25 cycles of simple shearing are averaged to see the prediction response of the saturation versus matric suction. The shear modulus model parameters (n_e, k_G^e) were calibrated from the first cycle of shearing, and therefore it seemed logical to calibrate the transient curve in the same manner for comparison.

Using undrained experimental data from cyclic simple shearing of initial saturations in the funicular regime at 1% strain, the initial 1.25 cycles of the saturation versus matric suction data are fit to the linear equation in excel. Initial parameters are selected for the slope (m). An excel column is created with the transient scanning curve equation for matric suction using a selected slope (m) and the input saturation (S) will be the actual data points from the 1.25 undrained cycling data. Another excel column is created to compute the squared difference between the calculated matric suction (using the selected slope parameter) and the actual matric suction data. A cell is designated as the residual sum of squares and is used to calculate the sum of the squared differences

of the predicted matric suction and data matric suction column. Using Solver in excel, the residual sum of squares is input as the ‘target cell’ and is selected to be minimized by changing the (m) cell to fit the actual data. By selecting ‘solve’, excel computes the values for (m) that best fit the actual matric suction data by reducing the residual sum of squares cell to 0. The same procedure is used to find the slopes of the transient scanning curve at 200 cycles.

Using the above procedure, the rewetting path of the undrained specimen can be defined as a log-linear equation is defined to track the changes in saturation with the changes in matric suction (the equation is derived in Appendix A3). Undrained cyclic simple shear test data set 01 from Rong and McCartney (2020b) have initial degrees of saturation ranging in the funicular regime and are presented in Table 5 with corresponding initial matric suctions. The calibrations of the undrained data from 1.25 cycles were found to have initial slopes very close to the same value despite the range in initial saturations and is presented in Figure 5.2.2.

Table 5: Initial values of degree of saturation and matric suction from the undrained CSS Data Set 01 from Rong and McCartney (2020b).

S_o (unitless)	ψ_o (kPa)
0.117	10
0.200	6
0.300	4
0.400	3
0.558	2

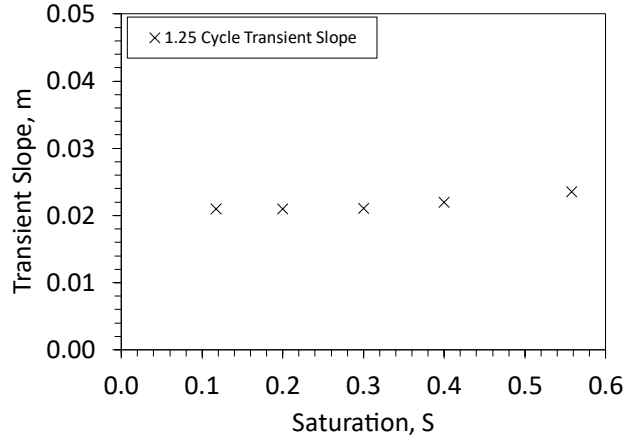


Figure 5.2.2 Slopes of transient SWRC wetting paths of data after 1.25 cycles of undrained cyclic simple shear.

Table 6: Initial conditions of the saturation, matric suction, and average slope for the transient SWRC rewetting path of the undrained data.

S_o	ψ_o (kPa)	m_{ave} (slope)
0.117	10	0.021
0.200	6	
0.300	4	
0.400	3	
0.558	2	

The undrained cyclic simple shear transient SWRC slopes from Data Set 1 for 200 cycles at 1% shear strain is presented in Figure 5.2.1. It is apparent from the undrained experimental CSS data that the slope of the transient curve is higher for specimens with higher initial saturation. The CSS data showed the initial transient SWRC slopes at 1.25 cycles for all the funicular regime saturations were approximately the same value of 0.021. The average transient SWRC slope over the entire 200 cycles for each set of unsaturated undrained data is presented in Table 7.

Table 7: Averaged transient SWRC slopes over entire 200 cycles from undrained cyclic simple shear Data Set 01 for funicular regime saturations.

Initial Degree of Funicular Saturation (S_f)	0.117	0.2	0.3	0.4	0.558
Slope (m_{200})	0.021	0.043	0.053	0.076	0.085

The test at the lowest degree of saturation of $S = 0.117$ had no further evolution in the transient SWRC slope and remained constant at 0.021. The transient SWRC slope increased for initial degrees of saturation in the funicular regime that were larger than $S = 0.117$ (S_f is defined as an initial degree of saturation higher than test value of 0.117), and it was found that the slope increase for each saturation in the funicular regime (m_{sf}) (where m_{sf} represents the new predicted slope based on the lowest slope value for initial degree of saturation $S = 0.117$) could be approximated using the initial transient SWRC slope of the lowest saturation ($m_{s=0.117} = 0.021$) that had no further slope change using Eq. (5.4.1):

$$m_{sf} = m_{s=0.117} + S_{s=0.117} S_f \quad (5.4.1a)$$

$$m_{sf} = 0.021 + 0.117 S_f \quad (5.4.1b)$$

Using the empirically derived equation in Eq. (5.4.1), a model is created to link the slope at the lowest saturation with the slope for higher degrees of saturation in the funicular regime. Figure 5.2.3(a) shows the undrained CSS data initial transient slope averages at 1.25 cycles and 200 cycles and Figure 5.2.3(b) shows the empirically derived equation representing the evolution in the transient slope with continued cycles of shear strain in blue with the data from the undrained cyclic simple shear tests in orange. Using the empirical equation to derive the remaining transient slopes from the lowest degree of saturation allows for fewer tests to model the full range of saturations in the funicular regime and the predicted slope values can be found in Table 8.

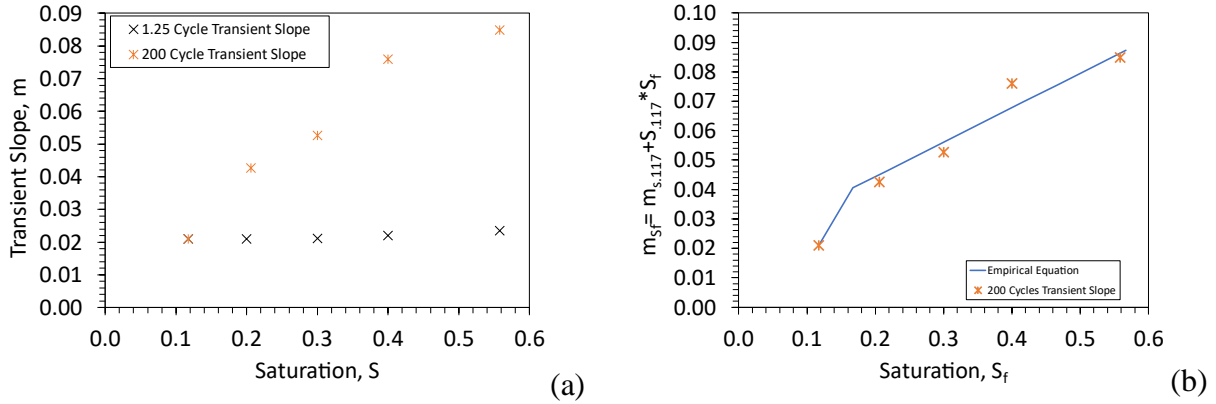


Figure 5.2.3 (a) Slopes of the transient SWRC scanning curve with averages at 1.25 cycles and 200 cycles (b) Empirical prediction of the slope of the transient SWRC scanning curve with degree of saturation in the funicular regime for 200 cycles

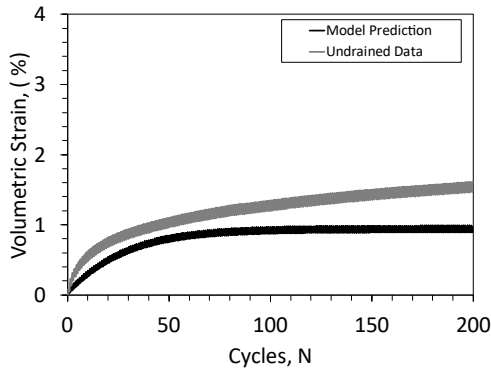
Table 8: Predicted transient SWRC slope of undrained CSS data set 01 for funicular regime saturations.

Initial Degree of Funicular Saturation (S_f)	0.117	0.2	0.3	0.4	0.558
Slope (m_{200})	0.021	0.045	0.056	0.070	0.086

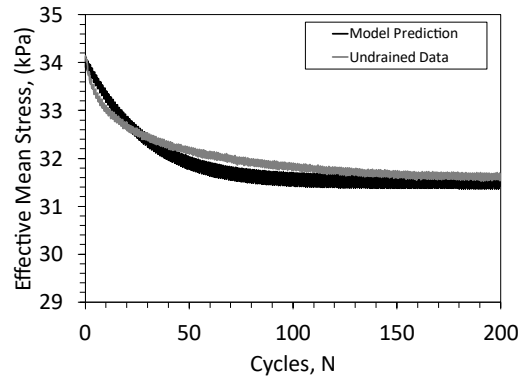
6 Analysis

6.1 Evolution in Hydro-Mechanical Variables during Undrained Cyclic Shearing

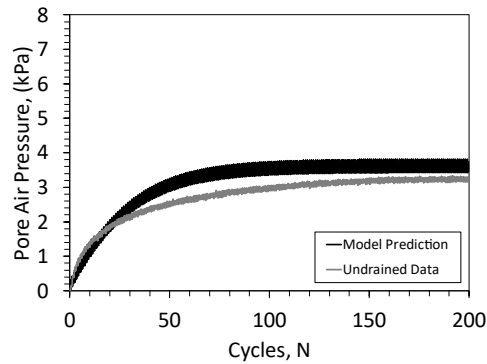
While comparisons between the evolution in key hydro-mechanical variables during undrained cyclic shearing for all the initial conditions summarized in Table 3 are presented in Appendix A6, this section presents an example of the evolution in the key hydro-mechanical variables for one of the tests on a sand specimen having an initial matric suction 4kPa and an initial saturation of 0.3. A comparison between the model prediction and the experimental results are presented in Figure 6.1.1 for undrained cyclic shearing at 1% shear strain (model in black, data in grey). The results in Figure 6.1.1(a) indicate that the model can capture the evolution in the volumetric strain well, especially at the beginning and end of cyclic shearing. The incremental results of the model show that the mean effective stress decreases with increasing cycles. The model's volumetric compression increases due to the lowering of the mean effective stress but at a decreasing rate, which is similar to the undrained CSS data results. The model's incremental pore air and water pressures increase at different rates during cyclic simple shearing which results in a decrease in the predicted value of matric suction from the models.



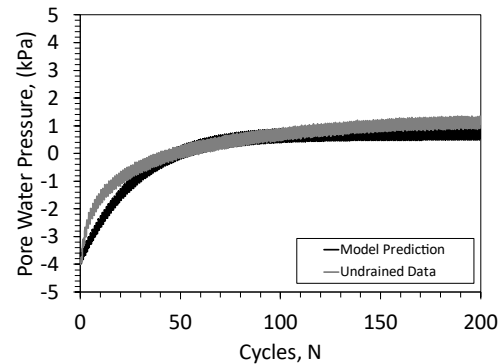
(a)



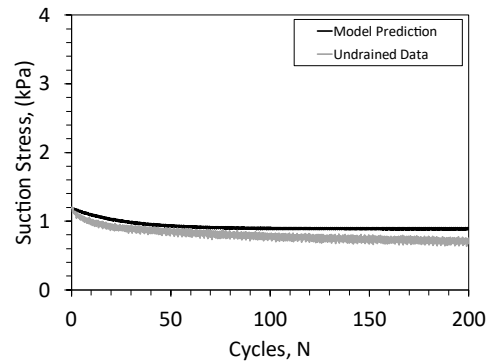
(b)



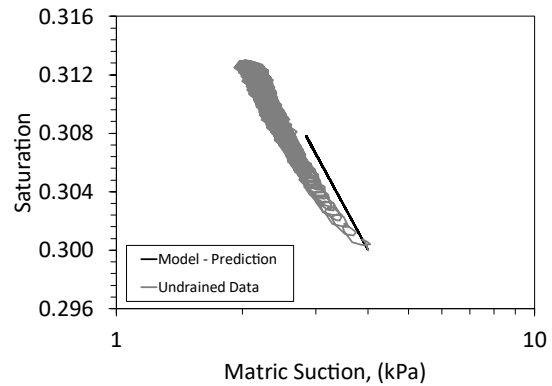
(c)



(d)



(e)

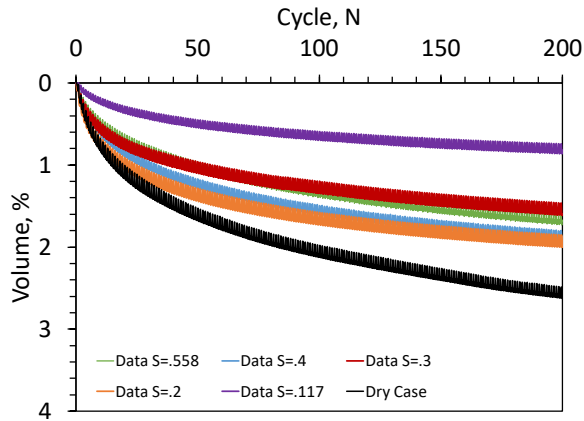


(f)

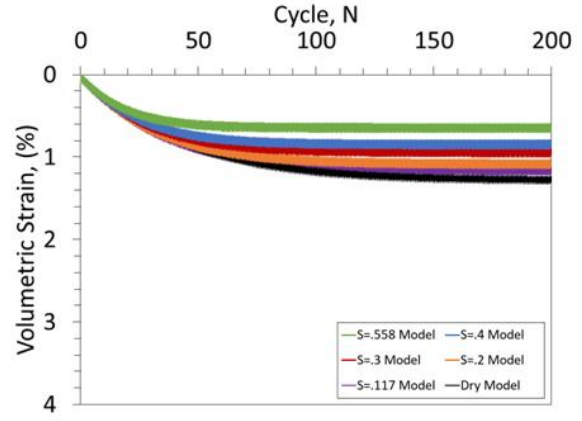
Figure 6.1.1 Comparison between cyclic simple shear results for a specimen with $S_0 = 0.3$ and model results: (a) Volume compression after 200 cycles; (b) Mean effective stress changes after 200 cycles; (c) Pore air pressure after 200 cycles; (d) Pore water pressure after 200 cycles; (e) Suction stress after 200 cycles; (f) Transient scanning path after 200 cycles

6.2 Evaluation of the Effects of Initial Degree of Saturation on Seismic Compression

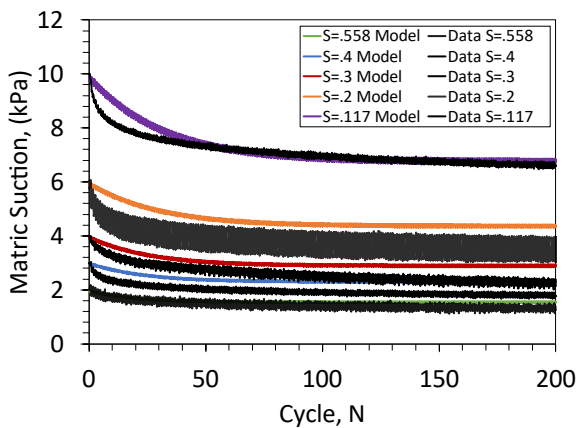
A comparison between the evolution in the key hydro-mechanical variables between the different tests in Data Set 1 is shown in Figure 6.2.1. The dry soil had the highest volumetric compression in both the model and the experiments. Overall, the model represents the evolution in hydromechanical variables well during many cycles of undrained shearing. However, the model's predictions for the volumetric compression were lower than the actual experimental data as shown in Figures 6.2.1(a) 6.2.1(b).



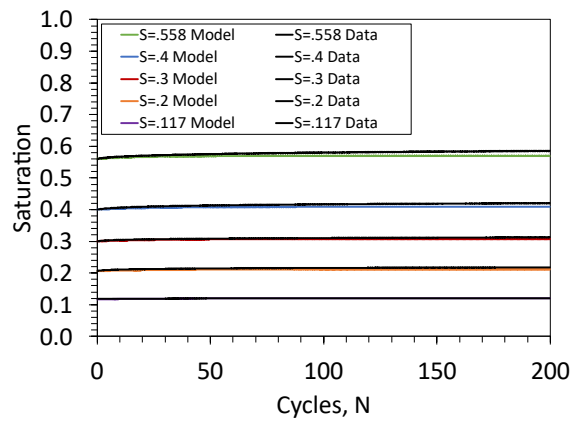
(a)



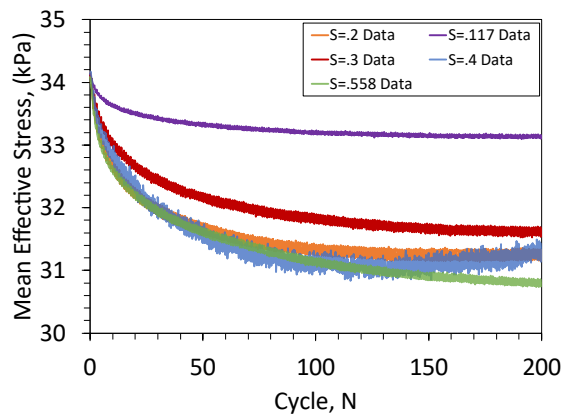
(b)



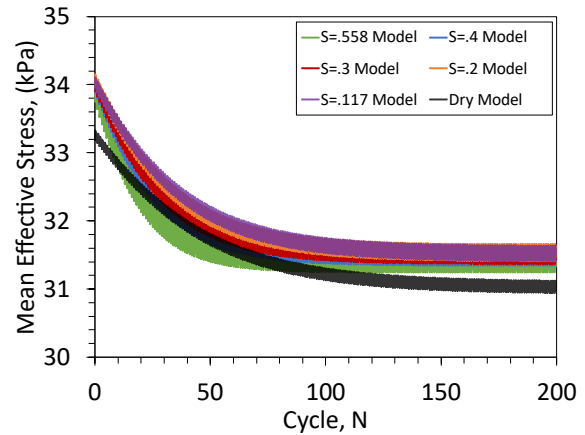
(c)



(d)



(e)



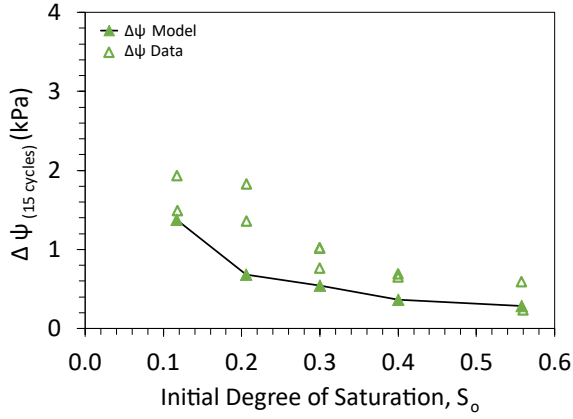
(f)

Figure 6.2.1 Data Set 1 vs. Model: (a) Volume vs. Cycles; (b) Model: Volume vs. Cycles; (c) Matrix suction vs. Cycles; (d) Saturation vs. Cycles; (e) Data: Mean Stress vs. Cycle; (f) Model: Mean Stress vs. Cycle

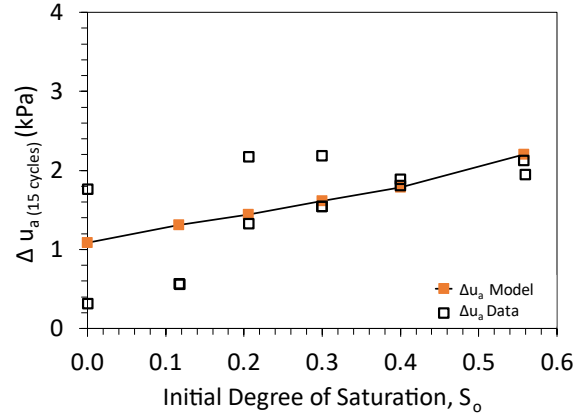
Using the calibrated parameters from the backbone curve and transient SWRC wetting path slope (m_{200}) averaged over 200 cycles of undrained CSS data, the pore pressures changes, volume

compressions and mean effective stress after 15 cycles are predicted and presented with the experimental results in Figure 6.2.2. The model's prediction of the pore matric suction changes over 15 cycles show a linear decreasing trend with increasing initial saturation, which is the same trend seen in the available data set. The model's prediction of the pore air pressure changes over 15 cycles show a linear increasing trend with decreasing initial saturation, which is in agreement with the available data set. However, the model's pore water pressure changes over 15 cycles appear to overpredict the available data sets. The volumetric compression predictions appear to underpredict the experimental data. The mean effective stress predictions of the model show a decreasing trend with increasing initial saturations, which is very similar to the data set at 15 cycles of shearing.

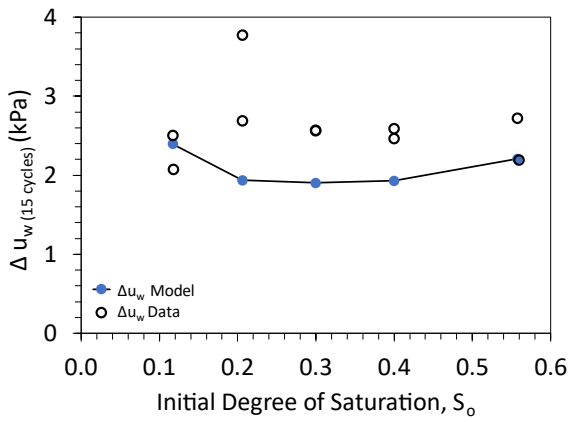
Using the calibrated parameters from the backbone curve and transient SWRC wetting path (calibrated to 200 cycles), the pore pressures changes, volume compressions, mean effective stress and predicted transient wetting path after 200 cycles (only Data Set 1) can be seen in Figure 6.2.3 and Figure 6.2.4. The results of the model show an uneven generation of pore air and water pressure, which is similar to the experimental data. The model's prediction of matric suction over 200 cycles has a good match to the experimental data. The volumetric compression predictions show a linear increasing trend with decreasing initial degree of saturation. The lowest degree of saturation in the undrained experiments had the lowest volumetric compression, however the model's predictions showed a linear increasing trend with the $S=0.117$ having the largest volumetric compressive strain aside from the modeled dry case.



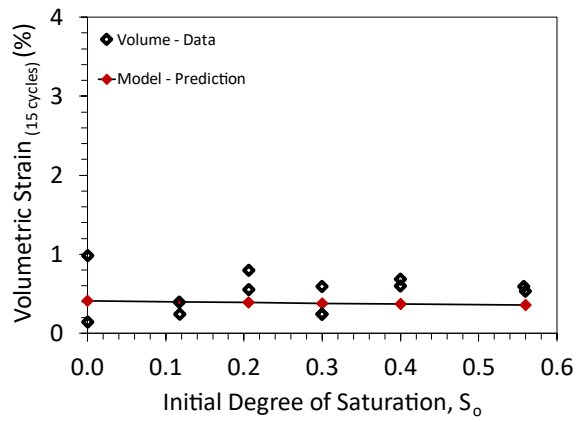
(a)



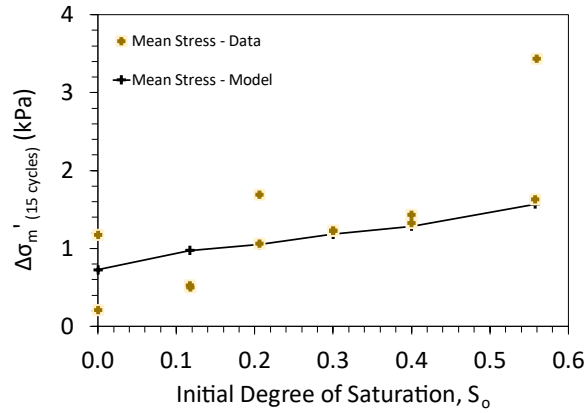
(b)



(c)



(d)



(e)

Figure 6.2.2 Comparison of trends between key hydro-mechanical variables after 15 cycles of undrained cyclic shearing and the initial degree of saturation obtained from the experiments of Rong and McCartney (2020b) and the model: (a) $\Delta\psi$ vs. S_0 ; (b) Δu_a vs. S_0 ; (c) Δu_w vs. S_0 ; (d) ΔV vs. S_0 ; (e) $\Delta\sigma'_m$ vs. S_0

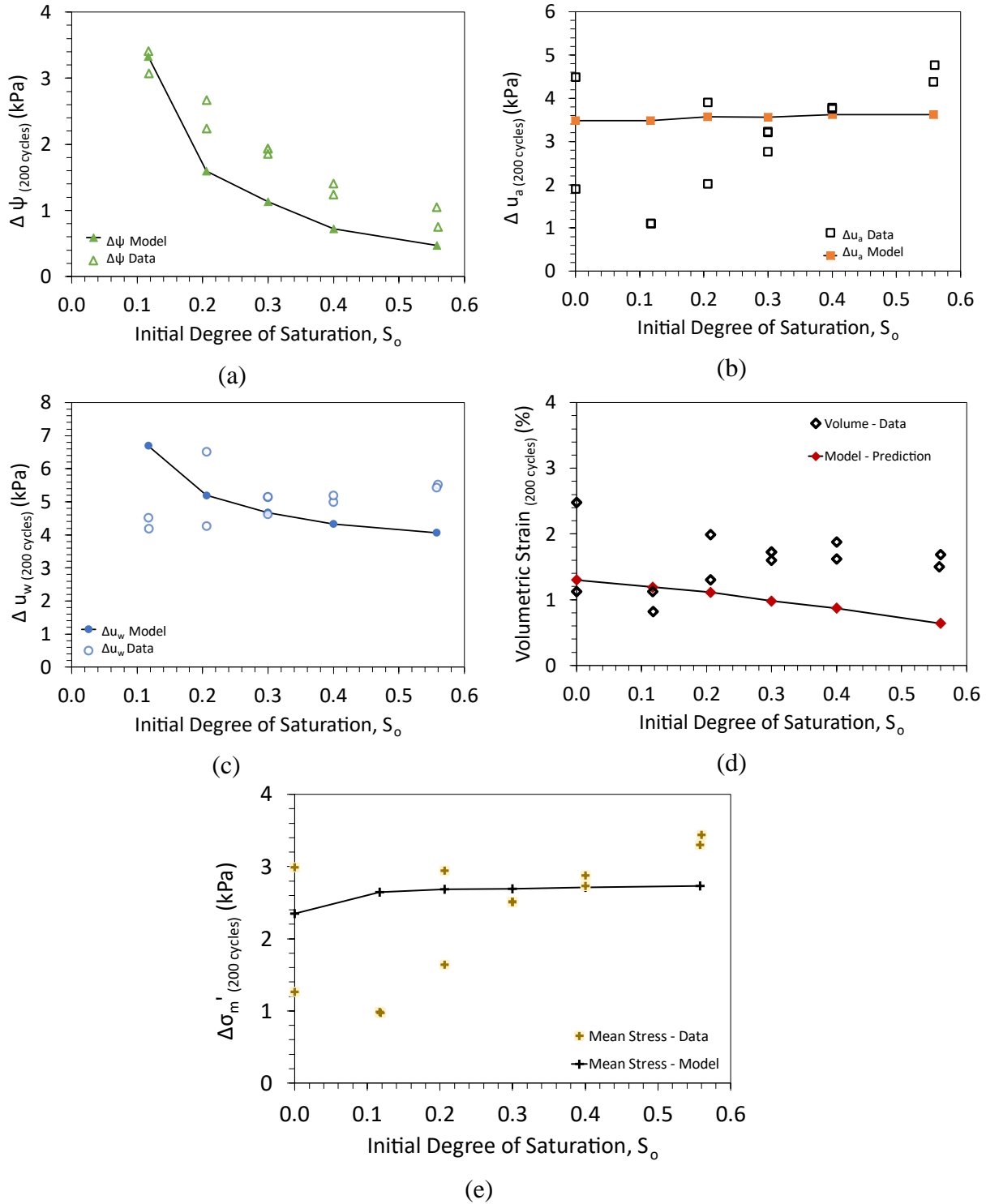


Figure 6.2.3 Comparison of trends between key hydro-mechanical variables after 200 cycles of undrained cyclic shearing and the initial degree of saturation obtained from the experiments of Rong and McCartney (2020b) and the model: (a) $\Delta \psi$ vs. S_o (b) Δu_a vs. S_o (c) Δu_w vs. S_o (d) ΔV vs. S_o (e) $\Delta \sigma'_m$ vs. S_o

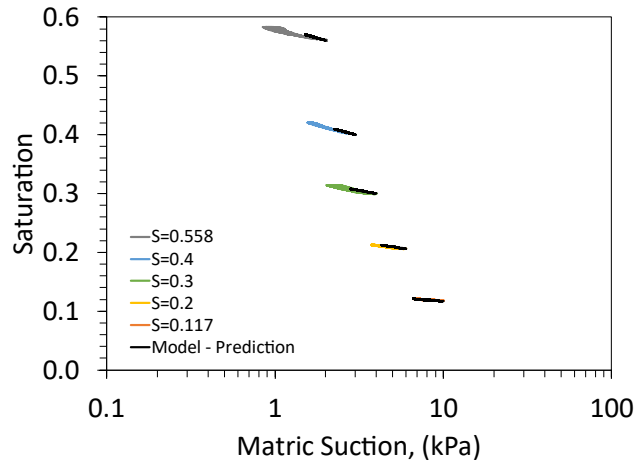


Figure 6.2.4 Transient SWRC scanning paths and predict transient SWRC paths from the model and experimental results from Data Set 1.

6.3 Evaluation of Reasons behind Discrepancy between Model and Experiments

6.3.1 Pore Air Pressure Generation

The predictions of pore air pressure generation from the model at 15 cycles show an increase with rising levels of initial degree of saturation. Similar results were observed in the undrained CSS data showing that higher initial degrees of saturation garnered more pore air compression and volume compression. The results in Figure 6.3.1.1 show that the model predicts an increasing trend in pore air pressure as initial degrees of saturation increase. During undrained CSS the air voids are squeezed by the pore water (due to the incompressibility of water) which increases the pore air pressure. A specimen with a higher initial saturation will contain more water exerting pressures on the air-filled voids and therefore will garner more air pressure generation in the voids during undrained CSS. The poromechanical coupling effect of the pore water squeezing the air voids to induce volumetric compression results in an overall increase to the saturation of the pore voids and a reduction in the mean effective stress of the soil skeleton. The predictions of pore air pressure at 15 cycles appears to capture the characteristic behavior of a loose granular soil. However, after several cycles the predicted pore air pressures approach similar values with slight

increases for higher initial degrees of saturations as observed in Figure 6.3.1.1(b). This was an unexpected observation from the model and may be due to the hydro-mechanical coupling effects on the mean effective stress for the different tests.

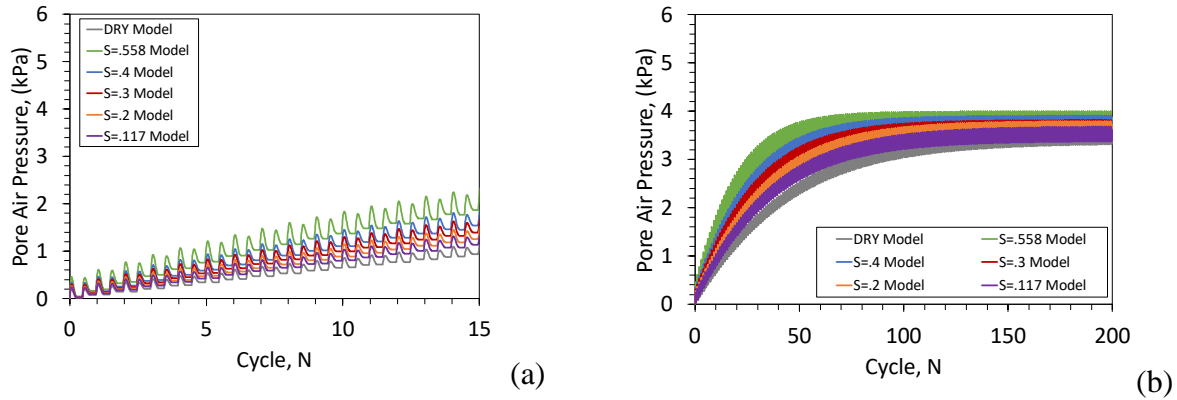


Figure 6.3.1.1 Model predictions of pore air pressure generation by initial saturation after (a) 15 cycles (b) 200 cycles

At 15 cycles, the model predictions of matric suction are captured by the uneven generation of pore water and air pressure. The model's results exhibited a decreasing trend in the matric suction regardless of 15 or 200 cycles, which is consistent with the available undrained cyclic shearing data from the literature. Similar trends were reported in Craciun and Lo (2010) showing a decrease in the matric suction of unsaturated soils during repeated cycles of undrained shearing on unsaturated soils. As the soil experiences a decrease in matric suction during undrained cyclic simple shearing, the largest air voids become flooded with nearby capillary water due to the shaking and rearrangement of soil particles. Occluded air bubbles can become trapped within water-filled pores due to the wetting process during cyclic shearing and may then damp out changes in pore water pressure during soil particle rearrangement.

6.3.2 Pore Water Pressure Generation

The slope of the transient scanning curve is dependent on the applied shear strain, initial degree of saturation, and initial matric suction. Although vertical effective stress does contribute to volumetric compression, it is not as significant as the effect of shear strain as the vertical total stress is maintained constant and changes in suction and degree of saturation have relatively small effects on the vertical effective stress. The pore water occupancy has a dual effect in that its representation as a pore void stress both can reduce and increase the effective stress during cyclic simple shear depending on draining conditions and its ratio to the remaining solids (soil) and fluids (air). If the drained conditions permit water to leave and matric suction increases, this typically correlates to a decrease in pore void water as the water is drawn out of the soil (drying effects) and the effective stress increases. When performing undrained cyclic simple shear tests, the matric suction will inevitably decrease due to the inability of water to flow out of the sample leading to air void compression (plastic volumetric compression), saturation increase and loss of effective stress. The developed hyperbolic model captures the trends of CSS testing to aid in replicating the seismic compression response of unsaturated sand during an earthquake, but the trends are only reliable for the initial cycles and begin to deviate around 25 cycles.

In the hyperbolic model presented, data was collected from experiments conducted by Rong and McCartney (2020b), and slopes of the transient scanning curve for initial cycling data at 1.25 cycles and 200 cycles were calibrated to fit and predict the pore pressures and volumetric changes of a sand specimen of approximately 45% density under a vertical stress of 50 kPa and 1% applied cyclic shear strain. The slopes of the transient scanning curve are a function of the applied cyclic shear strain, initial degree of saturation and initial matric suction. Since the model is centralized around the slopes of the transient scanning curve, it can only accurately predict the

volumetric compressions and pore pressure generation for the sand specimen at $D_r=0.45$ and 1% cyclic shear strain. In the undrained cyclic simple shear tests, the slope of the transient curve increases for initial degrees of saturations higher than 0.117 after initial cycling. Although there is a deviation in the model's pore pressure generation after numerous cycles, the model still provides a good approximation to the pore air generation and matric suction trends compared to the undrained CSS data up to 15 cycles.

The model does not provide insight on how the initial slope of the transient curve changes with higher or lower shear strains. More undrained tests of unsaturated sands at higher or lower shear strains are needed to provide insight on how the transient slopes evolve with increasing or decreasing shear strain. The best model representation will always be actual experimental data, and this is due to the various fallacies that can arise during parameter selection.

A compilation of the model results using the slope predictions equation (equation 5.4.1b) based on the lowest transient slope at the initial degree of saturation $S = 0.117$ are summarized in Appendix A6. The results of the model's volumetric compressions increase due to the response of the saturation change is more accurately captured given the change from the initial slope. The mean effective stress decreased which corresponds to the increase in volumetric compression. The model prediction of the pore air pressure increased while the pore water pressure predictions decreased slightly. The largest graphical variation is captured in the saturation versus matric suction plot as shown in Figures 6.3.2.1(a) and 6.3.2.1(b).

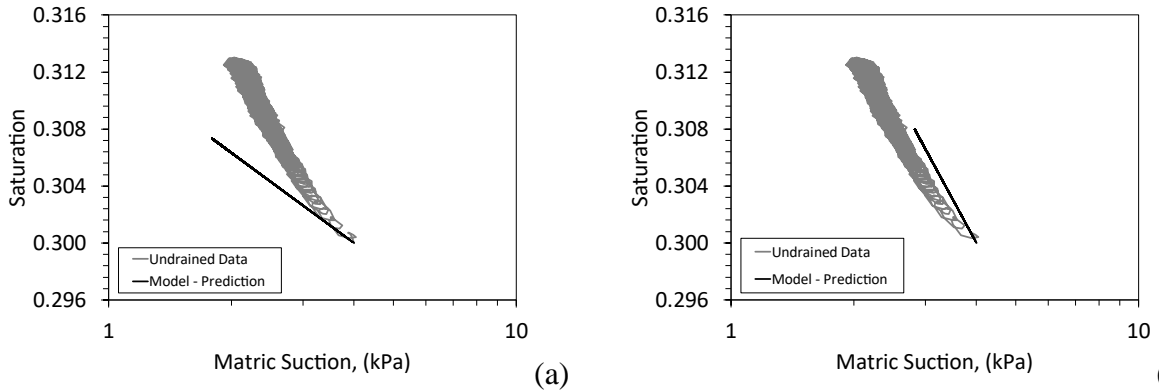


Figure 6.3.2.1 Variation in results between Data Set 1 transient SWRC: (a) $S=0.3$ $\psi=4$ kPa model calibrated to 1.25 cycles (b) $S=0.3$ $\psi=4$ kPa model calibrated to 200 cycles.

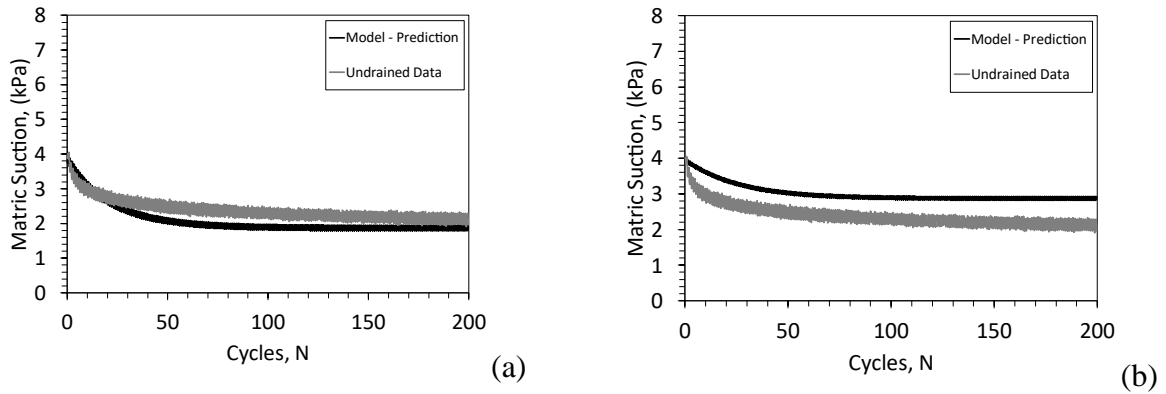


Figure 6.3.2.2 Variation in results between Data Set 1 matric suction vs. N cycles (a) $S=0.3$ $\psi=4$ kPa model calibrated to 1.25 cycles, (b) $S=0.3$ $\psi=4$ kPa model calibrated to 200 cycles

7 Conclusions

Results of the strain-controlled hyperbolic model showed that the permanent volumetric compressions are underpredicted and this could be due to the assumption that unloading is purely elastic overestimating hysteretic damping in the soil specimen. The model is intended for unsaturated soils in the funicular regime and a key feature is it assumes that the pore pressures have different generations due to the presence of air-water menisci with continuous air and water phases. While the model captured the trends in hydromechanical variables measured in many tests, a linearly decreasing trend between seismic compression and the initial degree of saturation was predicted from the model while a nonlinear increasing-decreasing trend was observed from the experiments. This may have been due to:

- Initial saturation may control the linear decreasing predictions of plastic volumetric strain causing air pressure generation to be the same after numerous cycles
- The model at 15 cycles shows a similar increasing trend for pore air generation to the experimental data but after many cycles pore air generation is approximately the same value as all other funicular saturation predictions with vary slight variation.
- Amplitudes of cyclic shear strains in the experimental data varied in range and never achieved intended strain range of $\mp 1.0\%$ during cycling (i.e., strain variance $\mp 0.2\%$ to $\mp 0.4\%$)
- Possible equipment issues in the measured pore air pressures during the test (probe interference with soil during shearing)
- Unloading path during cyclic shearing considered purely elastic, unable to fully capture nonlinearity of shear modulus
- Variation in small strain shear modulus for different suctions not considered in modeling of small strain shear modulus

- Model cannot predict the effect of different controlled shear strains due to empirical derivation of transient SWRC path.
- The evolution in the degree of saturation from the model did not capture the effects of creep during cycling.

8 Recommendations for Future Research

The model development raised several interesting questions that can be explored in future studies as additional experimental data becomes available, including:

- The role of the parameter n_e is not well understood in the model. As Rong and McCartney (2020a, 2020b) performed all tests under the same vertical total stress of 50 kPa, the actual value of n_e could not be confirmed. Cyclic simple shear tests performed at different values of mean effective stresses would help to understand the impact of the mean effective stress on the parameters of the hyperbolic curve. Changes in the magnitude of n will mean that evolution in the mean effective stress during cyclic shearing will have a greater effect on the evolution in plastic volumetric strain.
- The shift in the hysteretic shear stress-strain curves in the experiments should be better understood and may have been due to creep.
- For the collection of undrained data, the cyclic simple shear apparatus appeared to have issues with applying the target shear strain which can be observed in the shear stress versus shear strain plot in Figure 8.1 and also had a non-symmetric shape. Additional experimental improvements may be needed.

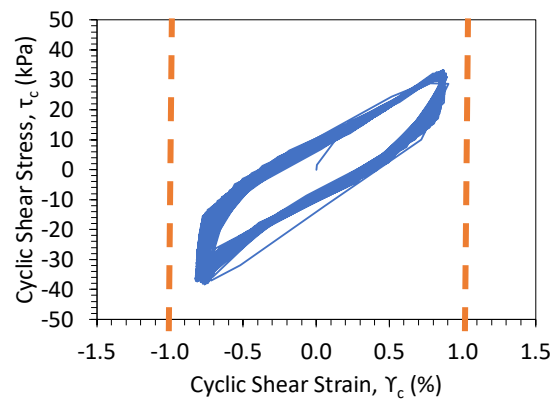


Figure 8.1 Shear stress-shear strain loops from undrained Data Set 2: $\psi_o = 6kPa$, $S_o = 0.2$

Appendix A

A1: Hyperbolic fitting for cyclic shearing Appendix

Using the small strain shear modulus and the ultimate shear stress, a hyperbolic model can be defined from initial loading data of the soil and is referred to as the backbone curve as shown in Figure A1.

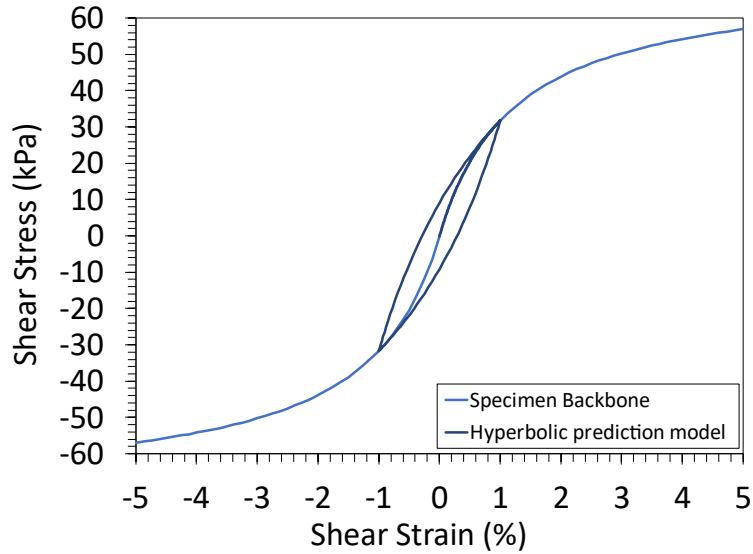


Figure A1: Depiction of backbone curve with a hysteretic loop depicting shear strain range of 1% representing 1.25 cycles of shear strain.

The backbone curve shown in Figure A1 was defined by fitting a hyperbola to the results from a monotonic set of shear stress versus shear strain data. Using hyperbolic fitting, the shear modulus is converted to a strain dependent parameter by linearizing the initial loading data of the stress strain curve. Specifically, by linearizing the relationship between $(\frac{\gamma}{\tau})$ and (γ) , the slope and intercept can be interpreted as $(\frac{1}{\tau_{ult}})$ and $(\frac{1}{G_i})$, ultimate shear stress and initial shear modulus, respectively.

$$\tau = \frac{\gamma}{\frac{1}{G_i} + \frac{\gamma}{\tau_{ult}}} \quad (\text{A1-1})$$

$$\frac{\gamma}{\tau} = \frac{1}{G_i} + \frac{\gamma}{\tau_{ult}} \quad (\text{A1-2})$$

The empirically based mathematical model can be seen in Figure A2. The ultimate shear stress is considered a fake parameter because the value is never reached and is used in calculating the reduction factor to truncate the hyperbolic curve from linear elastic shearing to nonlinear plastic shearing.

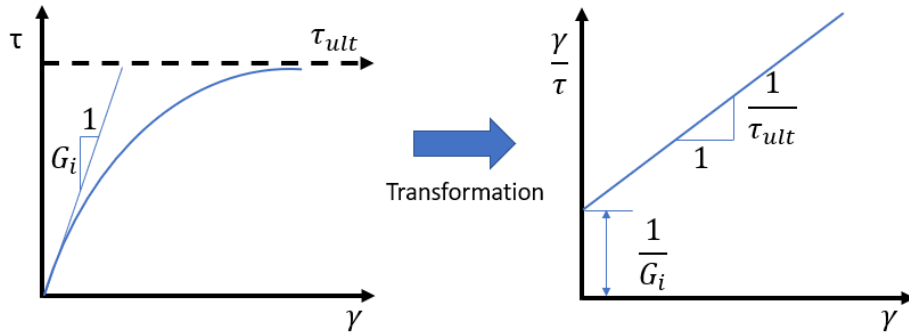


Figure A2: Linear transformation of hyperbolic shear stress-strain relationship.

Using the ultimate shear stress from the best fit hyperbola and the shear stress at failure, (τ_f), the failure ratio (R_f) can be defined:

$$R_f = \frac{\tau_f}{\tau_{ult}} \quad (\text{A1-3})$$

The failure ratio aids in governing the overall shape of the shear stress strain curve. The ultimate shear stress will always be larger than the shear stress at failure and therefore (R_f) will be smaller than unity. An (R_f) value close to 1 signifies that the hyperbolic curve is very ductile, (R_f) values approaching 0 signify a very brittle curve.

Since the actual data does not match a hyperbola perfectly, a certain stress level range is needed when fitting the slope and intercept. The stress level (SL) is defined as follows:

$$SL = \frac{\tau}{\tau_f} \quad (\text{A1-4})$$

If multiple data sets are available for the same soil sample at varying mean stresses, linearizing the data as seen in Figure 3A, the shear modulus number, (K_G^e) and exponent, (n_e), can be interpreted as the slope and intercept, respectively.

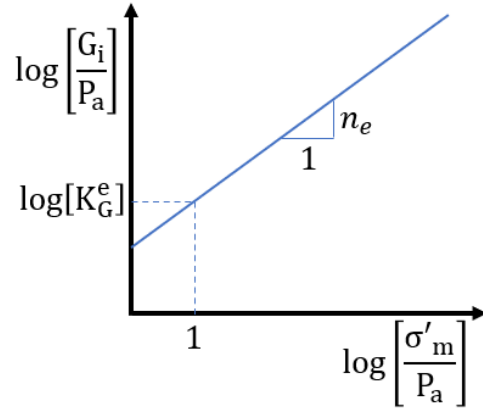


Figure A3: Variation of initial shear modulus with changing mean stress

$$G_i = K_G^e * P_a * \left(\frac{\sigma'_m}{P_a}\right)^{n_e} \quad (A1-5)$$

$$\log \left[\frac{G_i}{P_a} \right] = \log(K_G^e) + n_e \log \left(\frac{\sigma'_m}{P_a} \right) \quad (A1-6)$$

A2. Pore Air Pressure Derivation

Using Boyle's Law and an isothermal fluid elasticity, a relationship for the bulk modulus of air can be defined for seismic compression. It is assumed that all volumetric compression occurs in the air voids. The initial and final volume of water and soils does not change during undrained cycling. The image below shows before and after cycling as it pertains to the air in the sample:

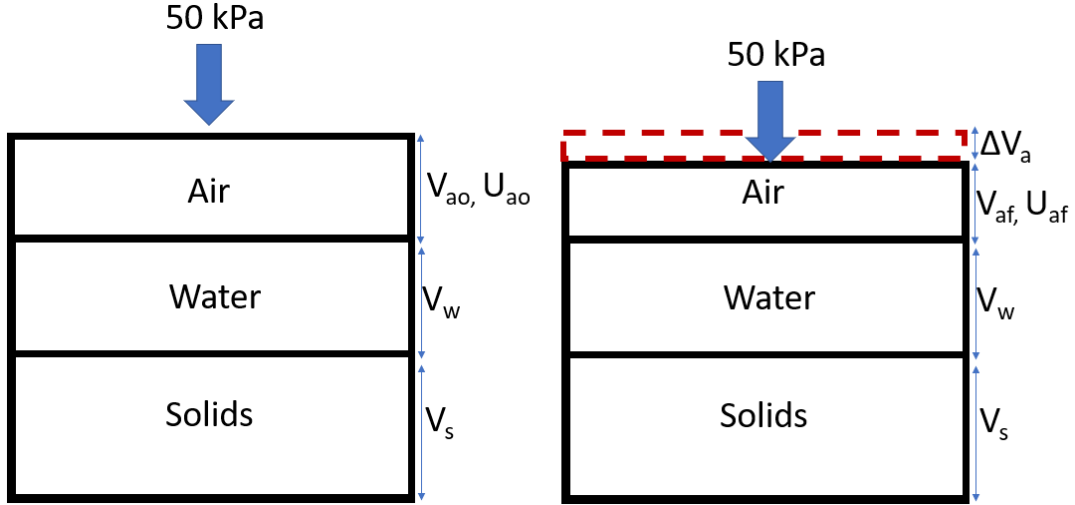


Figure A4: (a) Before cycling air pressure and volume (b) After cycling air pressure and volume

Boyle's Law for the undrained compression of air is given by:

$$u_{ao} V_{ao} = u_{af} V_{af} \quad (A2-1)$$

The change in volume of air can be defined as:

$$\Delta V_a = V_{ao} - V_{af} \quad (A2-3)$$

Which can be rearranged to find the V_{ao} and V_{af} :

$$V_{ao} = \Delta V_a + V_{af} \quad (A2-4)$$

$$V_{af} = V_{ao} - \Delta V_a \quad (A2-5)$$

Using these relationships, the volumetric strain of the air can be defined:

$$\varepsilon_a = \Delta V_a / V_{ao} = \frac{V_{ao} - V_{af}}{V_{ao}} \quad (A2-6)$$

Rearranging Eq. (6) to simplify to strain in terms of V_{af} :

$$V_{af} = V_{ao} - \varepsilon_a V_{ao} = V_{ao}(1 - \varepsilon_a) \quad (A2-7)$$

Substituting Eq. (6) into Boyle's Law Eq. (1):

$$u_{ao} V_{ao} = u_{af} \times V_{ao}(1 - \varepsilon_a) \quad (A2-8)$$

$$u_{ao} = u_{af}(1 - \varepsilon_a) = u_{af} - u_{af}\varepsilon_a \quad (A2-9)$$

$$u_{af}\varepsilon_a = u_{af} - u_{ao} = \Delta u_a \quad (\text{A2-10})$$

$$u_{af} = \Delta u_a / \varepsilon_a \quad (\text{A2-11})$$

The isothermal pressurization for air can be represented can be represented by fluid elasticity:

$$\varepsilon_a = \Delta u_a / K_a \quad (\text{A2-2})$$

Combining Eq (A2-11) and Eq (A2-2), the bulk modulus of air can be defined as:

$$K_a = u_{af} \quad (\text{A2-14})$$

Assuming that the initial pore air pressure is at atmospheric pressure and under isothermal conditions ($T = 70 \text{ C}$):

$$\Delta u_a = u_{af} - u_{ao} = u_{af} - P_{atm} \quad (\text{A2-12})$$

$$u_{af} = \Delta u_a + P_{atm} \quad (\text{A2-13})$$

$$K_a = \Delta u_a + P_{atm} \quad (\text{A2-15})$$

This equation implies that when cycling initiates, the bulk modulus of air will evolve with the change in pore air pressure. To define the change in pore air pressure, a model needs to be defined in terms of the three-phase system (air, water, solids):

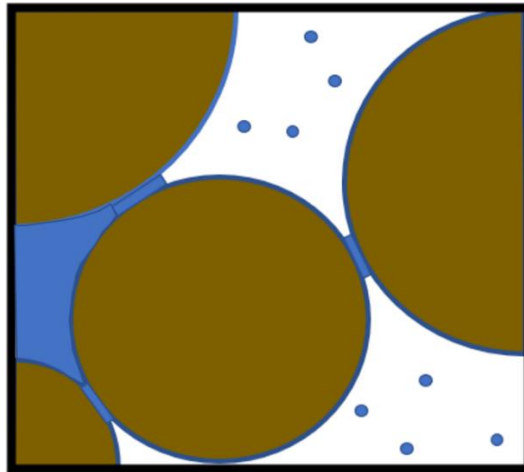


Figure A5: Three phase system of air (white), water (blue), and solids (brown) in the funicular region of SWRC.



Figure A6. Idealized image of partitioned three-phase system.

To represent the properties of the three-phase system, it is advantageous to define each phase in terms of their individual volumes:



Figure A7. Idealized image of volumes of a 3-phase system.

The sums of the volumes of the 3-phase system need to be defined in terms of saturation and void ratio. The phase relationships can be used to define the equations:

$$V_T = V_{s0} + V_{w0} + V_{a0} \quad (\text{A2-16})$$

$$V_{V0} = V_{w0} + V_{a0} \quad (\text{A2-17})$$

$$V_T = V_{so} + V_{vo} \quad (\text{A2-18})$$

$$S_o = \frac{V_{wo}}{V_{V_o}} = \frac{V_{wo}}{V_{a_o} + V_{wo}} \quad (\text{A2-19})$$

$$e_o = \frac{V_{vo}}{V_{s_o}} = \frac{V_{a_o} + V_{wo}}{V_{s_o}} \quad (\text{A2-20})$$

If the volume of the solids is equal to one, which is the case when finding relationships between different phase variables, the following relationships can be defined:

$$V_{s_o} = V_{s_f} = 1 \quad (\text{A2-21})$$

$$e_o = \frac{V_v}{V_s} = \frac{V_v}{1} \rightarrow e_o = V_{v_o} \quad (\text{A2-22})$$

$$S_o = \frac{V_w}{V_v} = \frac{V_w}{e_o} \rightarrow S_o \times e_o = V_{w_o} \quad (\text{A2-23})$$

If the previous relationships are true, then the three-phase system can be redefined as Figure 5:



Figure A8. Three-phase system new relationship

Using these relationships, the volume of air can be redefined in terms of void ratio and saturation:

$$V_{a_o} = V_T - V_{w_o} - V_{s_o} \quad (\text{A2-24})$$

$$V_T = 1 + e_o \quad (\text{A2-25})$$

$$V_{a_o} = 1 + e_o - S_o \times e_o - 1 = e_o - S_o \times e_o \quad (\text{A2-26})$$

$$V_{ao} = e_o \times (1 - S_o) \quad (A2-27)$$

The three-phase system can now be defined as shown in Figure 5A below:

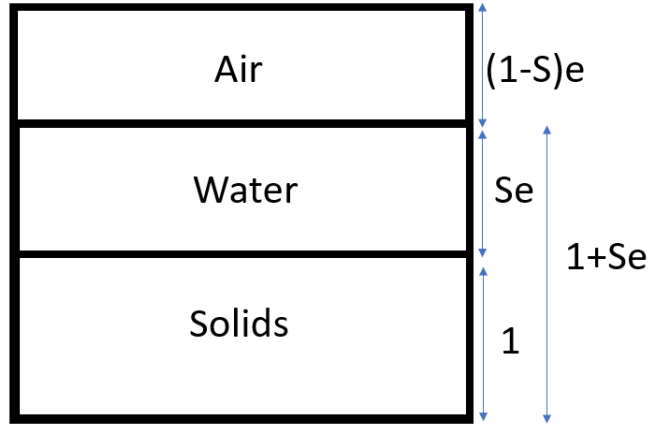


Figure A9. Three-phase system defined in terms of saturation and void ratio.

Cyclic shearing will cause compression of the three-phase system over time. The compression of the water volume is considered very small in comparison to the compression of the air volume. The volume of air will be the largest contributor to compression of the three-phase system. Some air may dissolve into the capillary water due to Henry's law and the remainder of air (free air) may change in density as the air volume compresses. Assuming the Ideal Gas Law is valid for pore air, the free air in the system can be defined as:

$$u_{ao}V_{ao} = n_{ao(FA)}RT = \text{constant} \quad (A2-28)$$

$$u_{af}V_{af} = n_{af(FA)}RT = \text{constant} \quad (A2-29)$$

Eq. (28) and Eq. (29) can be set equal to each other, which also defines Boyle's Law for energy conservation:

$$u_{ao}V_{ao} = u_{af}V_{af} \quad (A2-1)$$

Since our system is in an undrained state, the amount of air particles is constant and can exist as free air in the voids or as dissolved air particles (Henry's Law) in the capillary water. The following equations are valid and true:

$$n_{ao(FA)} = \frac{u_{ao} V_{ao}}{RT} \quad (A2-30)$$

$$n_{af(FA)} = \frac{u_{af} V_{af}}{RT} \quad (A2-31)$$

$$n_{ao} = n_{af} \quad (A2-32)$$

$$n_{ao} = n_{ao(FA)} + n_{ao(DA)} \quad (A2-33)$$

$$n_{af} = n_{af(FA)} + n_{af(DA)} \quad (A2-34)$$

Henry's law can be written as follows assuming that volume of water is constant ($V_{wo} = V_{wf} = V_w$) during cycling:

$$n_{ao(DA)} = h \times u_{ao} \times V_w \quad (A2-35)$$

$$n_{af(DA)} = h \times u_{af} \times V_w \quad (A2-36)$$

Inserting Eq. (36) into Eq. (34) yields:

$$n_{af} = n_{af(FA)} + h \times u_{af} \times V_w \quad (A2-37)$$

Rearranging Eq. (37) and inserting into Eq. (31) yields:

$$n_{af} - h \times u_{af} \times V_w = \frac{u_{af} V_{af}}{RT} \quad (A2-38)$$

Inserting Eq. (32) into Eq. (38):

$$n_{ao} - h \times u_{af} \times V_w = \frac{u_{af} V_{af}}{RT} \quad (A2-39)$$

Inserting Eq. (33) into Eq. (39):

$$n_{ao(FA)} + n_{ao(DA)} - h \times u_{af} \times V_w = \frac{u_{af} V_{af}}{RT} \quad (A2-40)$$

Inserting Eq. (30) and Eq. (35) into Eq. (40):

$$\frac{u_{ao} V_{ao}}{RT} + h \times u_{ao} \times V_w - h \times u_{af} \times V_w = \frac{u_{af} V_{af}}{RT} \quad (A2-41)$$

Inserting Eq. (30), Eq. (13) and Eq. (5) into Eq. (41):

$$\frac{u_{ao} V_{ao}}{RT} + h \times u_{ao} \times V_w - h \times (\Delta u_a + P_{atm}) \times V_w = \frac{(\Delta u_a + P_{atm})(V_{ao} - \Delta V_a)}{RT} \quad (A2-42)$$

Inserting $P_{atm} = u_{ao}$:

$$\frac{P_{atm} V_{ao}}{RT} + h \times P_{atm} \times V_w - h \times (\Delta u_a + P_{atm}) \times V_w = \frac{(\Delta u_a + P_{atm})(V_{ao} - \Delta V_a)}{RT}$$

Expand ():

$$\frac{P_{atm} V_{ao}}{RT} + h \times P_{atm} \times V_w - h \times \Delta u_a V_w - h \times P_{atm} \times V_w = \frac{(\Delta u_a + P_{atm})(V_{ao} - \Delta V_a)}{RT}$$

Reduce:

$$\frac{P_{atm} V_{ao}}{RT} - h \times \Delta u_a V_w = \frac{(\Delta u_a + P_{atm})(V_{ao} - \Delta V_a)}{RT}$$

Expanding RHS:

$$\frac{P_{atm} V_{ao}}{RT} - h \times \Delta u_a V_w = \frac{(\Delta u_a \times V_{ao})}{RT} - \frac{(\Delta u_a \times \Delta V_a)}{RT} + \frac{(P_{atm} \times V_{ao})}{RT} - \frac{(P_{atm} \times \Delta V_a)}{RT}$$

Reduce:

$$-h \times \Delta u_a V_w = \frac{(\Delta u_a \times V_{ao})}{RT} - \frac{(\Delta u_a \times \Delta V_a)}{RT} - \frac{(P_{atm} \times \Delta V_a)}{RT}$$

Multiply both sides by RT and rearrange to put all Δu_a on one side:

$$(P_{atm} \times \Delta V_a) = h \times \Delta u_a V_w \times RT + (\Delta u_a \times V_{ao}) - (\Delta u_a \times \Delta V_a)$$

$$(P_{atm} \times \Delta V_a) = (h \times V_w \times RT + V_{ao} - \Delta V_a) \Delta u_a$$

The change in pore air pressure is equivalent to:

$$\frac{(P_{atm} \times \Delta V_a)}{(h \times V_w \times RT + V_{ao} - \Delta V_a)} = \Delta u_a \quad (A2-43)$$

Using saturation and void ratio definitions from Eq. (23) and Eq. (27) to replace V_w and V_{ao} respectively:

$$\frac{(P_{atm} \times \Delta V_a)}{(h \times S_o \times e_o \times RT + e_o \times (1 - S_o) - \Delta V_a)} = \Delta u_a \quad (A2-44)$$

For cumulative volume strain, the pore air pressure is defined as:

$$\begin{aligned}
 V_t &= 1 + e_o \\
 \frac{\Delta V_a}{V_t} &= \Delta \varepsilon_v^p \\
 \Delta V_a &= \Delta \varepsilon_v^p (1 + e_o) \\
 \varepsilon_v^p &= \Delta \varepsilon_v^p + \varepsilon_{v0}^p \\
 \text{cumulative volume strain} &= \varepsilon_v^p (1 + e_o) \\
 u_a &= \frac{(P_{\text{atm}} \times \varepsilon_v^p (1 + e_o))}{(h \times S_o \times e_o \times RT + e_o \times (1 - S_o) - \varepsilon_v^p (1 + e_o))} \quad (\text{A2-44b})
 \end{aligned}$$

The solubility constant in Henry's equation is defined as below ($h_a = 0.187 \frac{\text{mol}}{\text{L} \cdot \text{bar}}$):

$$h = \frac{\rho_a}{\rho_w} h_a \quad (\text{A2-45})$$

Inserting the equation for pore pressure change Eq. (44b) into bulk modulus of air Eq. (15):

$$K_a = \left[\frac{(P_{\text{atm}} \times \varepsilon_v^p (1 + e_o))}{(h \times S_o \times e_o \times RT + e_o \times (1 - S_o) - \varepsilon_v^p (1 + e_o))} + P_{\text{atm}} \right] \quad (\text{A2-46})$$

Rearranging Eq. (46):

$$K_a = \left[\frac{\varepsilon_v^p (1 + e_o)}{(h \times S_o \times e_o \times RT + e_o \times (1 - S_o) - \varepsilon_v^p (1 + e_o))} + 1 \right] \times P_{\text{atm}} \quad (\text{A2-47})$$

A3: Relationship between Degree of Saturation and Volumetric Strain

Incremental change in saturation can be found using the initial conditions and assuming the change in pore air volume is responsible for the change in total volume of the specimen:

$$S = \frac{V_w}{V_v} \quad (\text{A3-1})$$

$$S = \frac{V_{wo}}{V_{af} + V_{wo}} \quad (\text{A3-2})$$

Using the equations defined in appendix A1, the following relationship exists for the initial volume of water:

$$V_{so} = V_{sf} = 1 \quad (\text{A3-21})$$

$$e_o = \frac{V_v}{V_s} = \frac{V_v}{1} \rightarrow e_o * V_s = V_{vo} \quad (\text{A3-22})$$

$$S_o = \frac{V_{wo}}{V_v} = \frac{V_{wo}}{e_o V_s} \rightarrow S_o \times e_o V_s = V_{wo} \quad (\text{A3-23})$$

$$S = \frac{V_s e_o S_o}{V_{ao} - \Delta V_a + V_s e_o S_o} \quad (\text{A3-3})$$

$$S = \frac{V_s e_o S_o}{(V_s e_o (1 - S_o)) - \Delta V_a + V_s e_o S_o} \quad (\text{A3-4})$$

$$S = \frac{V_s e_o S_o}{e_o - \Delta V_a} \quad (\text{A3-5})$$

where $\Delta \varepsilon_v^p = \frac{\Delta V_a}{V_t}$, $V_t = (V_s + e_o)$

$$S = \frac{V_s e_o S_o}{e_o - V_t \Delta \varepsilon_v^p} \quad (\text{A3-6})$$

$$S = \frac{V_s e_o S_o}{e_o - (V_s + e_o) \Delta \varepsilon_v^p} \quad (\text{A3-7})$$

$$S = \frac{V_s e_o S_o}{e_o - (V_s + e_o) \Delta \varepsilon_v^p} \quad (\text{A3-8a})$$

For cumulative saturation change, the cumulative volumetric strain can be defined as follows :

$$\varepsilon_v^p = \Delta \varepsilon_v^p + \varepsilon_{vo}^p \quad (\text{A3-9})$$

$$\text{cumulative volumetric change in volume} = \varepsilon_v^p (V_s + e_o) \quad (\text{A3-10})$$

$$S = \frac{V_s e_o S_o}{e_o - (V_s + e_o) \varepsilon_v^p} \quad (\text{A3-8b})$$

A4. Transient Scanning Curve Equation

To capture the poromechanical evolutions, the model uses empirical transient SWRC paths to calculate the changes in matric suction as the degree of saturation increases during rewetting. The data from Rong and McCartney (2020b) showed that the transient rewetting slopes increased with initial degree of saturation. The equation was derived using a simple linear path transformed for a semi-log plot. Using the rewetting path to create a linear equation to track the change in saturation with the change in matric suction would provide a way to model the pore water pressure generation. If initial cycling data is available, the slopes (m) can be interpreted and used to predict the trend of matric suction if the saturation changes are known:

$$S = -m \log_{10} \psi + b \quad (\text{A4-1})$$

$$S - b = -m \log_{10} \psi \quad (\text{A4-2})$$

$$10^{\frac{S-b}{-m}} = 10^{\log_{10} \psi} \quad (\text{A4-3})$$

$$10^{\frac{S-b}{-m}} = \psi \quad (\text{A4-4})$$

$$S_0 + m \log_{10} \psi_0 = b \quad (\text{A4-5})$$

$$\psi = 10^{\frac{S - (S_0 + m \log_{10} \psi_0)}{-m}} \quad (\text{A4-6})$$

A5. Volume Compression Equations

The volumetric compression equations are derived using a hyperbolic model similar to Duncan-Chang and can be found in Puebla et al (1997). The developed stress ratio is defined as the maximum shear stress divided by the mean stress. The developed stress ratio plotted against

the plastic shear strains has a hyperbolic function with the plastic tangential shear modulus as the slope. Taking the derivative, the developed stress ratio is defined as follows:

$$\Delta\eta_d = \left[\frac{\Delta\tau}{\sigma'_m} - \left(\frac{\tau}{(\sigma'_m)^2} \right) \Delta\sigma'_m \right] \quad (\text{A5-1})$$

The increment of the mean stress is defined as the final mean stress minus initial mean stress:

$$\Delta\sigma'_m = \sigma'_m - \sigma'_{m0} \quad (\text{A5-2})$$

The increment of the shear stress is defined similarly as the final shear stress minus the initial mean stress:

$$\Delta\tau = \tau - \tau_0 \quad (\text{A5-3})$$

Using the energy considerations for plane strain conditions: $d\varepsilon_2^e = d\varepsilon_2^p = 0$, the dissipated energy can be defined as:

$$dE^D = \sigma'_1 * d\varepsilon_1^p + \sigma'_3 * d\varepsilon_3^p \quad (\text{A5-4})$$

The equation can be expressed in the following way:

$$\sigma'_1 * d\varepsilon_1^p + \sigma'_3 * d\varepsilon_3^p = \frac{\sigma'_1 + \sigma'_3}{2} (d\varepsilon_1^p + d\varepsilon_3^p) + \frac{\sigma_1 - \sigma_3}{2} (d\varepsilon_1^p - d\varepsilon_3^p) \quad (\text{A5-5})$$

Now the equation for energy can be defined in terms of mean stress and shear stress:

$$dE^D = \sigma'_m * d\varepsilon_v^p + \tau * d\gamma^p \quad (\text{A5-6})$$

For constant volume assumptions, the energy dissipation can be defined as:

$$dE^D = \tau * d\gamma^p = \sigma'_m \sin \phi_{cv} d\gamma^p \quad (\text{A5-7})$$

The Cam Clay model for plastic energy dissipation is defined as:

$$dE^P = \sigma'_m \sin \phi_{cv} d\gamma^p \quad (\text{A5-8})$$

Combining equations A4-6 and A4-8:

$$\sigma'_m * d\varepsilon_v^p + \tau * d\gamma^p = \sigma'_m \sin \phi_{cv} d\gamma^p \quad (\text{A5-9})$$

Now the plastic volumetric strain can be defined as:

$$d\varepsilon_v^p = \left(\sin \phi_{cv} - \frac{\tau}{\sigma'_m} \right) d\gamma^p \quad (\text{A5-10})$$

In incremental form, the plastic volumetric strain increment can now be obtained:

$$\Delta\varepsilon_v^p = \left(\sin \phi_{cv} - \frac{\tau}{\sigma'_m} \right) \Delta\gamma^p \quad (\text{A5-10b})$$

The plastic shear strain increment is found using the derivative of the developed stress ratio and the tangential plastic shear modulus:

$$\Delta\gamma^p = \left(\frac{1}{G^p} \right) \left[\frac{\Delta\tau}{\sigma'_m} - \left(\frac{\tau}{(\sigma'_m)^2} \right) \Delta\sigma'_m \right] \quad (\text{A5-11})$$

Figure A10 shows the hyperbolic relationship between the plastic shear strain, tangential plastic shear modulus and the developed stress ratio (where $\eta_d = \frac{\tau}{\sigma'_m}$):

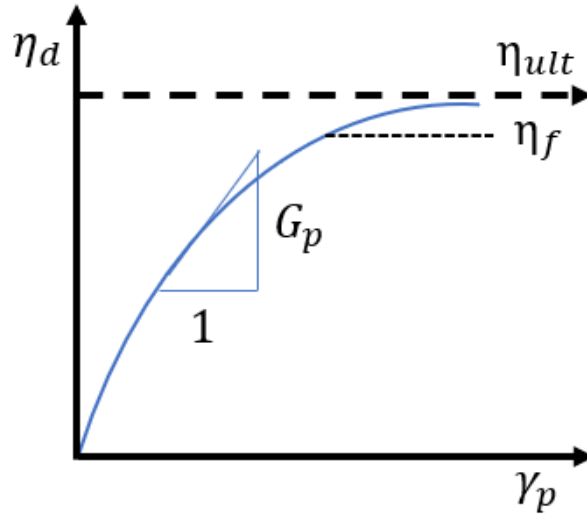


Figure A10. Normalized shear stress-shear strain curve.

A6. Graphical Results of Model for All Specimens

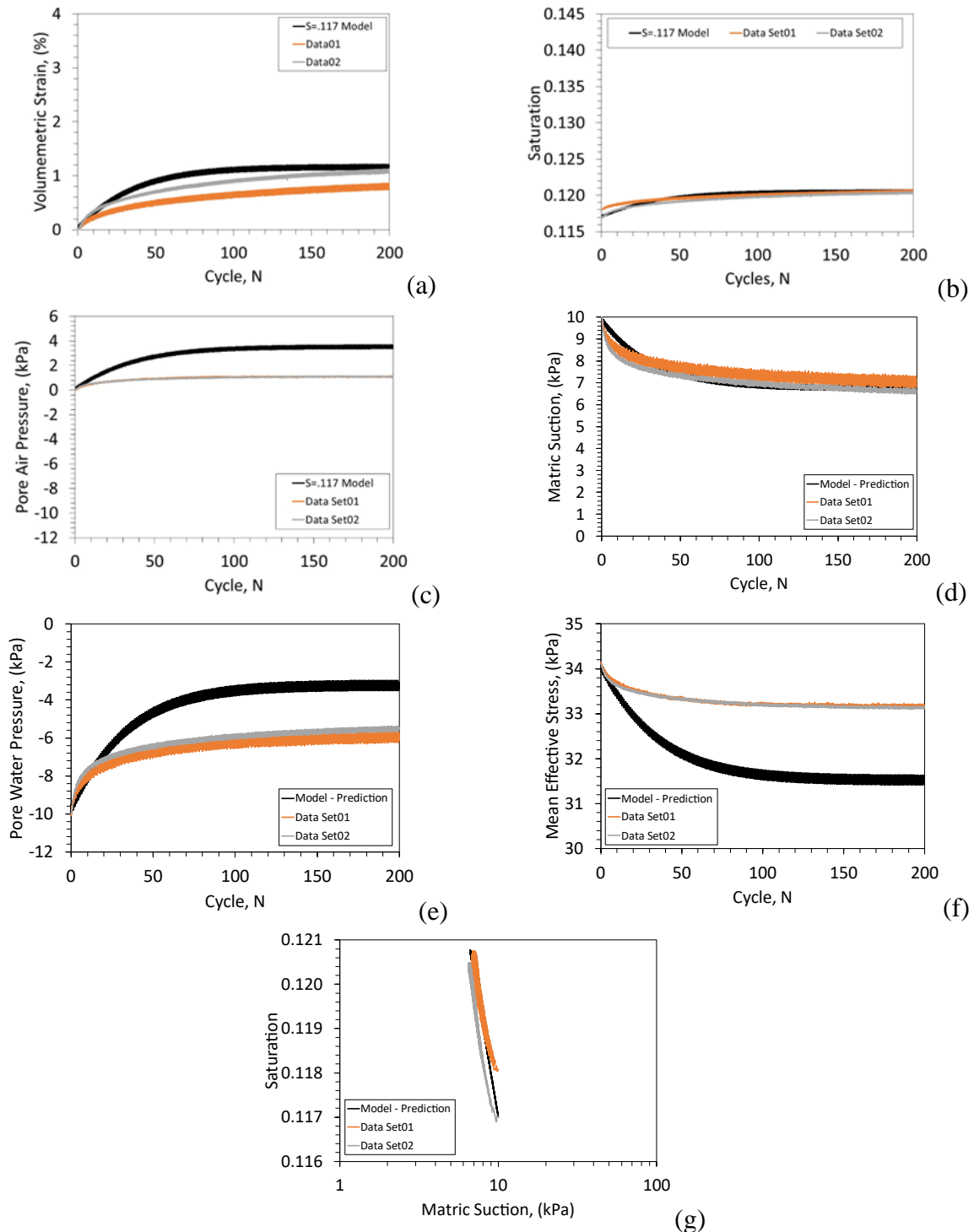


Figure A6-1: Comparison between experimental results and model predictions for a sand specimen with $S_o=0.117$, $\psi_o=10$ kPa: (a) Volume change; (b) Degree of Saturation; (c) Pore air pressure; (d) Matric suction; (e) Pore water pressure; (f) Mean effective stress; (g) Degree of saturation vs. matric suction

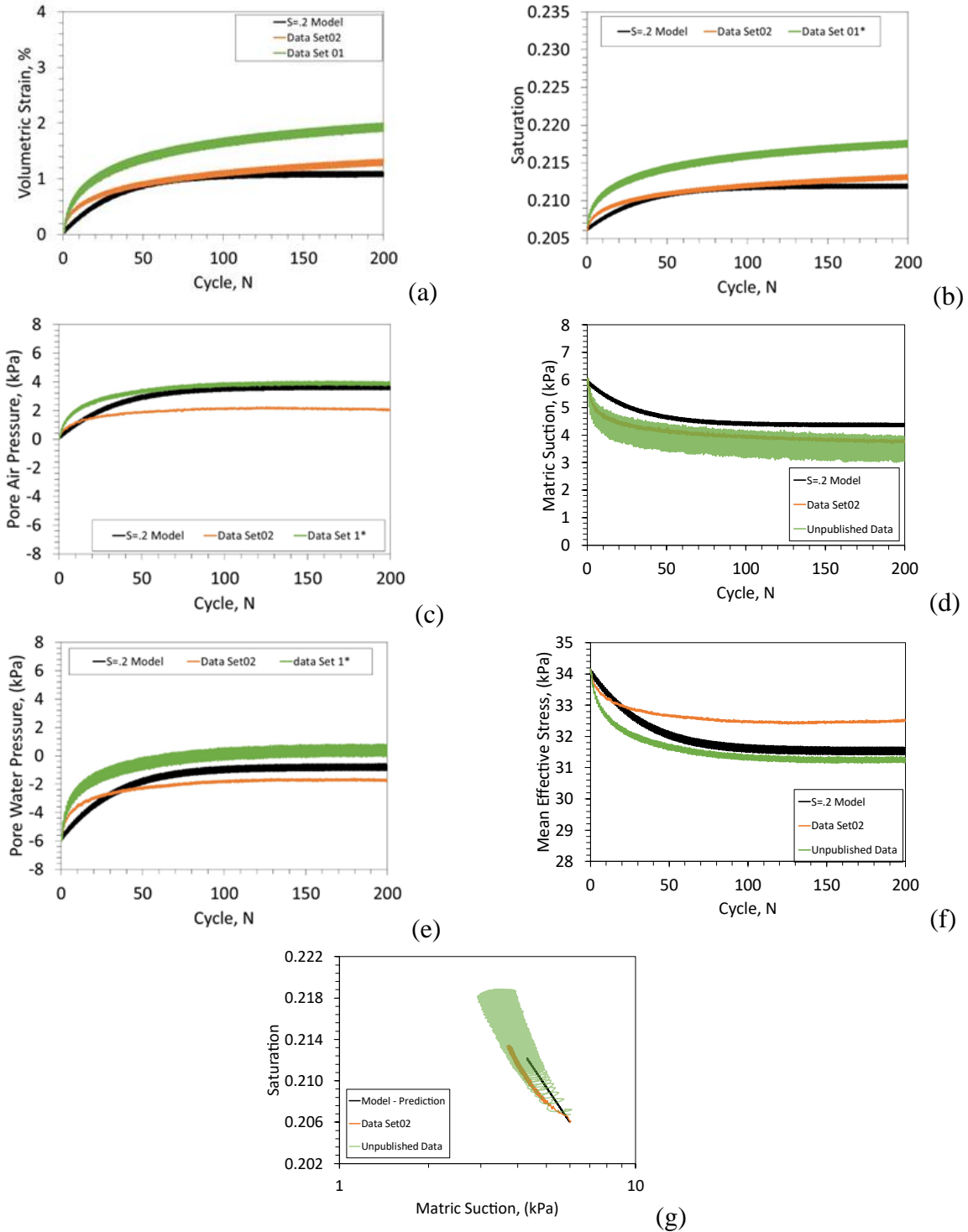


Figure A6-2 Comparison between experimental results and model predictions for a sand specimen with $S_o=0.2$, $\psi_o=6$ kPa for SWRC fit to low cycles: (a) Volume change; (b) Degree of Saturation; (c) Pore air pressure; (d) Matric suction; (e) Pore water pressure; (f) Mean effective stress; (g) Degree of saturation vs. matric suction

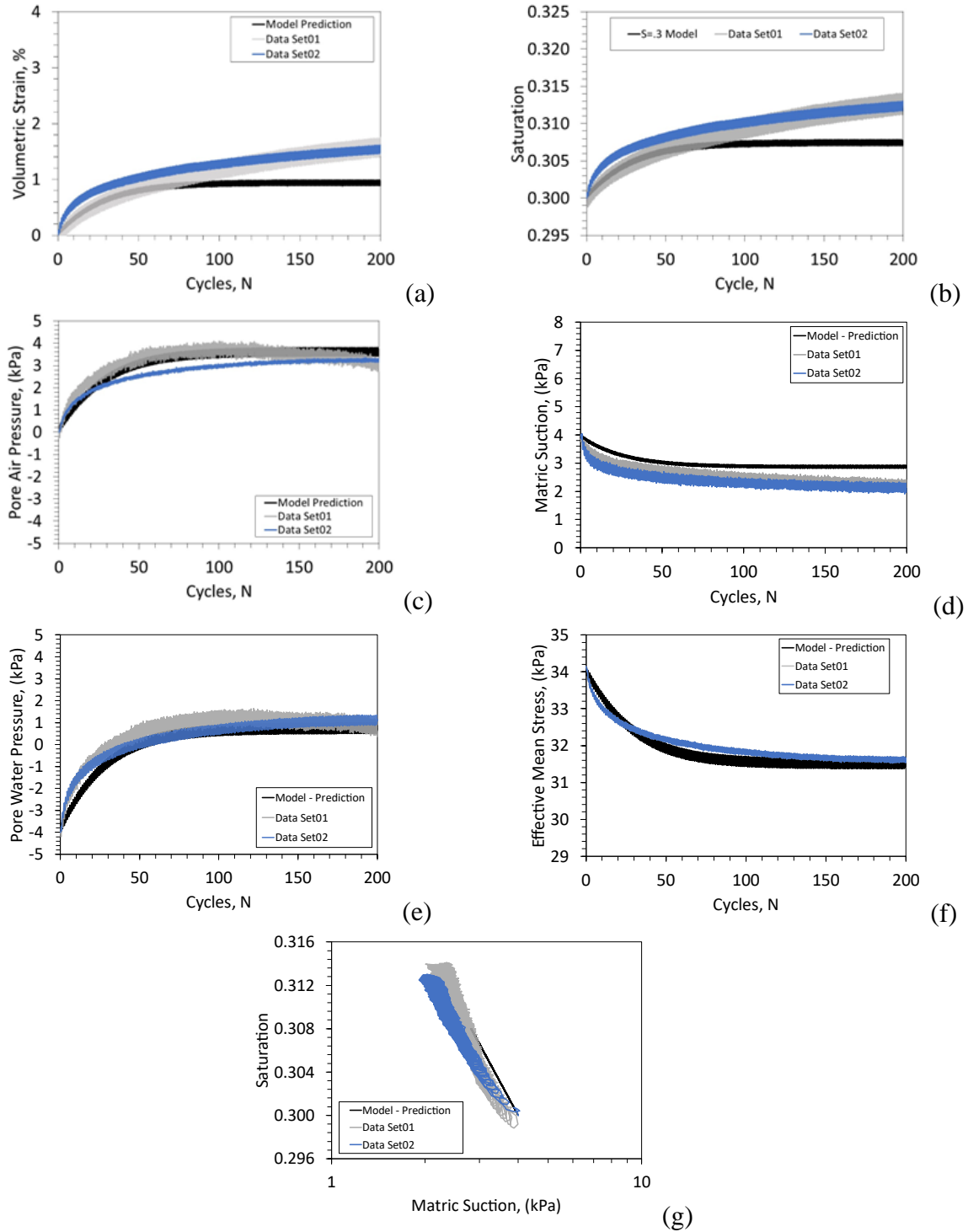


Figure A6-3 Comparison between experimental results and model predictions for a sand specimen with $S_o=0.3$, $\psi_o=4$ kPa for SWRC fit to low cycles: (a) Volume change; (b) Degree of Saturation; (c) Pore air pressure; (d) Matric suction; (e) Pore water pressure; (f) Mean effective stress; (g) Degree of saturation vs. matric suction

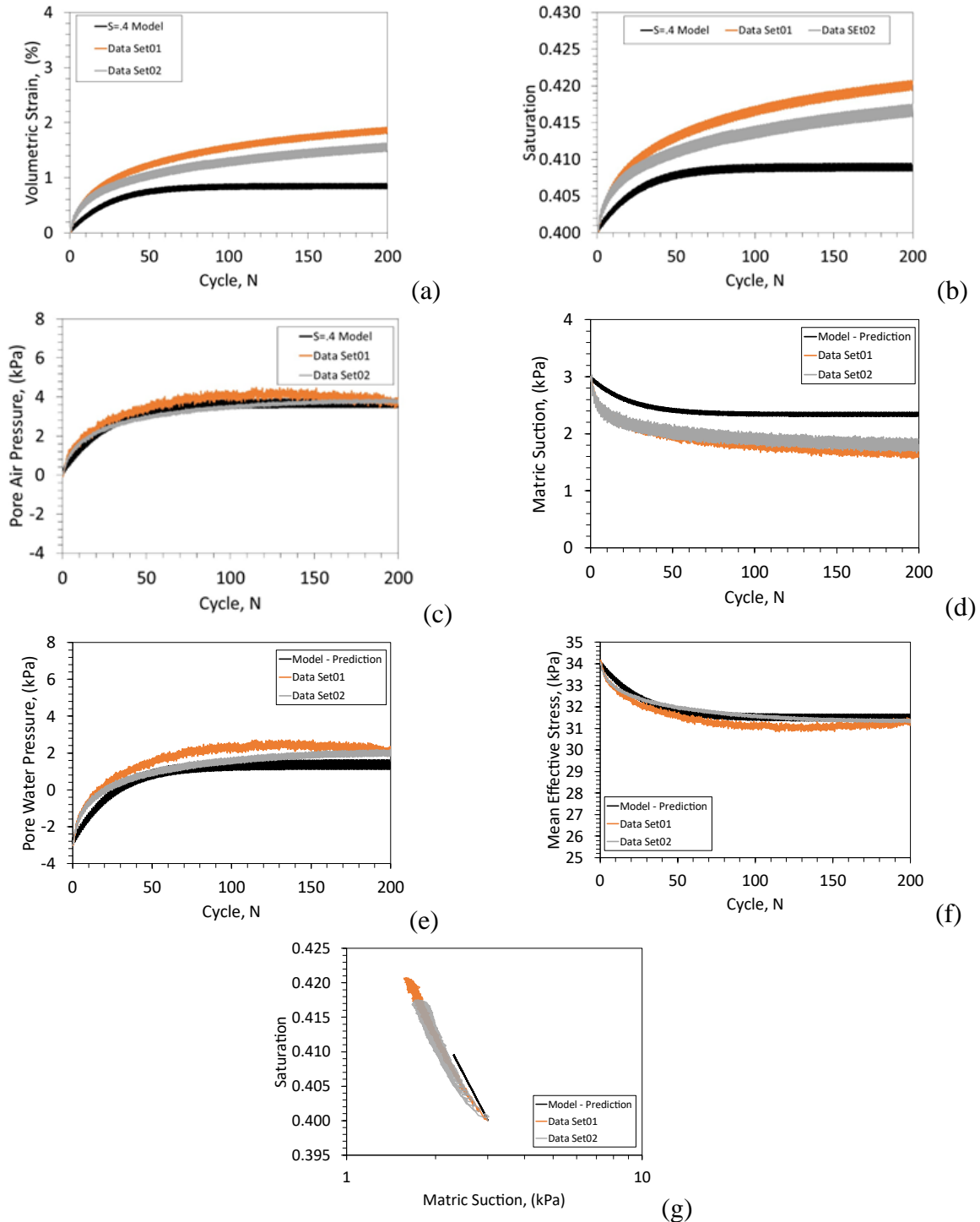


Figure A6-4 Comparison between experimental results and model predictions for a sand specimen with $S_0=0.4$, $\psi_0=3$ kPa for SWRC fit to low cycles: (a) Volume change; (b) Degree of Saturation; (c) Pore air pressure; (d) Matric suction; (e) Pore water pressure; (f) Mean effective stress; (g) Degree of saturation vs. matric suction

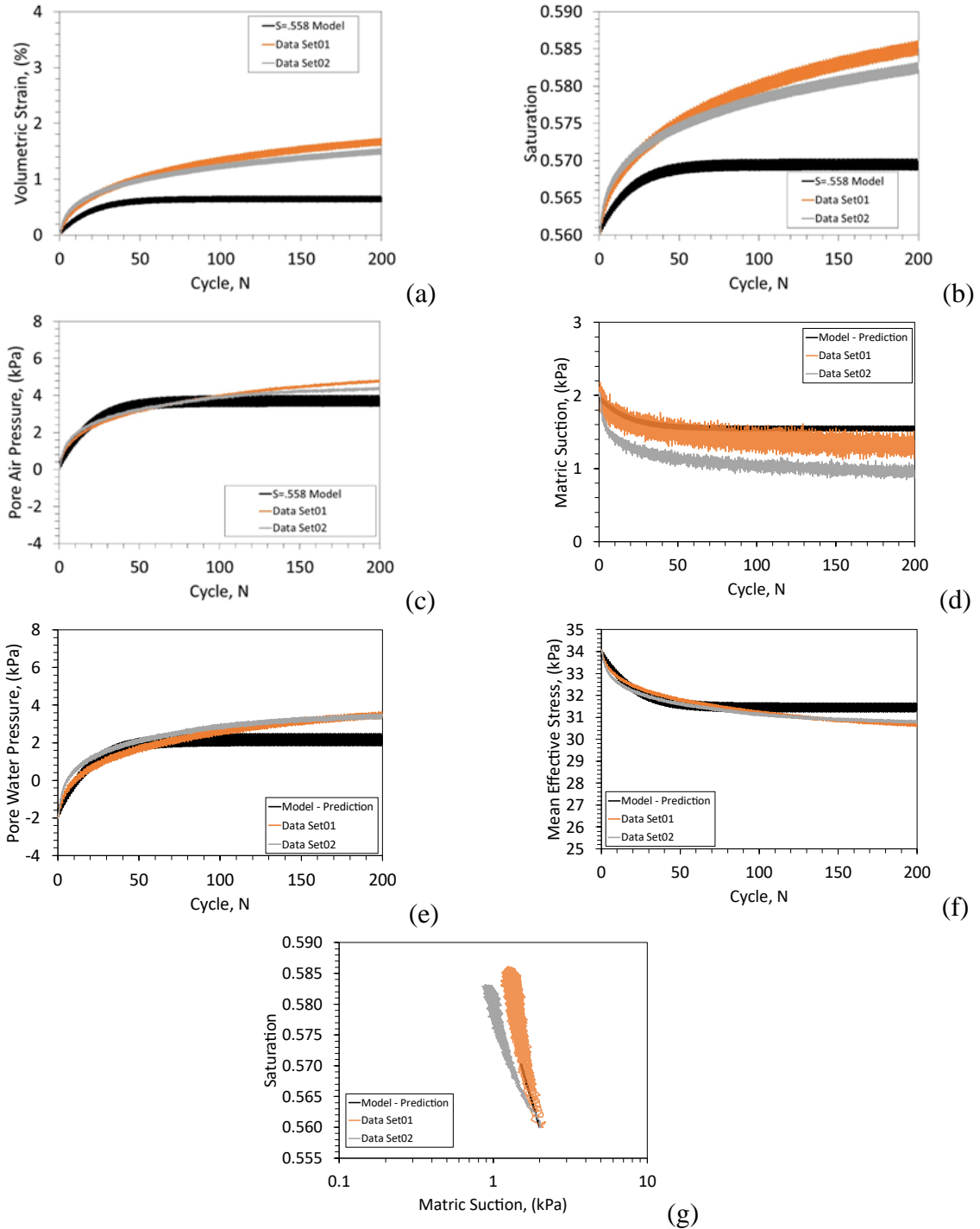


Figure A6-5: Comparison between experimental results and model predictions for a sand specimen with $S_o=0.56$, $\psi_o=2$ kPa for SWRC fit to low cycles: (a) Volume change; (b) Degree of Saturation; (c) Pore air pressure; (d) Matric suction; (e) Pore water pressure; (f) Mean effective stress; (g) Degree of saturation vs. matric suction

REFERENCES

- ASTM D6528 (2017). Standard Test Method for Consolidated Undrained Direct Simple Shear Testing of Cohesive Soils. ASTM International. West Conshohocken, PA.
- Beaty, M., and Byrne, P.M. (1998). "An effective stress model for predicting liquefaction behavior of sand." In *Geotechnical Earthquake Engineering and Soil Dynamics III*: (pp. 766-777). ASCE.
- Bishop, A.W. (1959). "The principle of effective stress." *Teknisk Ukeblad*, 106(39), 859-863.
- Bishop, A.W. and Blight, G.E. (1963). "Some aspects of effective stress in saturated and partly saturated soils." *Géotechnique*, 13(3), 177-197.
- Bjerrum, L. and Landva, A. (1966). "Direct simple-shear tests on a Norwegian quick clay." *Geotechnique*, 16(1), 1-20.
- Bray, J.D. and Olaya, F. R. (2022). "Examination of the volumetric strain potential of liquified soil with a database of laboratory tests." *Geo-Congress 2022*, 334, 495-505
- Byrne, P.M., Roy, D., Campanella, R.G., and Hughes, J. (1995). "Predicting liquefaction response of granular soils from pressuremeter tests." *ASCE National Convention, ASCE, GSP 56*, 122-135.
- Byrne, P.M. and Park, S.S. (2003). "Seismic liquefaction: centrifuge and numerical modeling" *FLAC and Numerical modeling in Geomechanics*, Brummer et al. (eds), 320-331.
- Byrne, P.M. Naesgaard, E. and Seid-Karbasi, M., (2006). "Analysis and design of earth structures to resist seismic soil liquefaction" *59th Canadian Geotechnical Conference*, Canadian Geotechnical Society. 1-24.
- Chong, S.H. and Santamarina, J.C. (2016). "Sands subjected to repetitive vertical loading under zero lateral strain: accumulation models, terminal densities, and settlement." *Canadian Geotechnical Journal*, 53(12), 2039-2046.
- Craciun, O. and Lo, S.C.R. (2010). "Matric suction measurement in stress path cyclic triaxial testing of unbound granular base materials." *Geotechnical Testing Journal*, 33(1), 33-44.
- Cuomo, S., Moscariello, M., and Foresta, V. (2017). "Wetting tests of partially saturated soils under simple shear conditions." *Géotechnique Letters*, 7(2), 197-203.
- Duncan, J.M. and Chang, C.Y. (1970). "Nonlinear analysis of stress and strain in soils." *Journal of Soil Mechanics and Foundations Div.*
- Duku, P.M., Stewart, J.P., Whang, D.H., and Yee, E. (2008). "Volumetric strains of clean sands subject to cyclic loads." *J. of Geotech. and Geoenv. Eng.*, 134(8), 1073-1085.

- Dong, Y., Lu, N., and McCartney, J.S. (2016). "Unified model for small-strain shear modulus of variably saturated soil." *J. of Geotech. and Geoenv. Eng.*, 142(9), 04016039.
- Dong, Y., Lu, N., and McCartney, J.S. (2017). "Scaling shear modulus from small to finite strain for unsaturated soils." *J. of Geotech. and Geoenv. Eng.*, 144(2), 04017110.
- Finn, W.L., Byrne, P.M., and Martin, G.R. (1976). "Seismic response and liquefaction of sands." *J. of Geotech. and Geoenv. Eng.*, 102(8), 841-856.
- Fredlund D.G. (2016). "Variables in saturated-unsaturated soil mechanics". *Soils and Rocks*, 39(1), 3-17
- Geiser, F., Laloui, L., and Vulliet, L. (2006). "Elasto-plasticity of unsaturated soils: laboratory test results on a remoulded silt." *Soils and Foundations*, 46(5), 545-556.
- Ghayoomi, M., McCartney, J.S., and Ko, H.Y. (2011). "Centrifuge test to assess the seismic compression of partially saturated sand layers." *Geotechnical Testing Journal*, 34(4), 321-331.
- Ghayoomi, M., McCartney, J.S., and Ko, H.Y. (2013). "Empirical methodology to estimate seismically induced settlement of partially saturated sand." *J. of Geotech. and Geoenv. Eng.*, 139(3), 367-376.
- Ghayoomi, M. and McCartney, J.S. (2016). "Procedure to estimate the seismic settlement of partially saturated soils." *Indian Geotechnical Journal (Special Issue on Unsaturated Soil Mechanics)*. 46(3), 272–275. DOI: 10.1007/s40098-015-0176-0.
- Hardin, B.O. and Richart, F.E. (1963). "Elastic wave velocities in granular soils." *Journal of Soil Mechanics and Foundations Divisions, Proc. ASCE* 89, 33-65.
- Hardin, B.O. and Black, W. (1969). "Closure on vibration modulus of normally consolidated clay." *Journal of Soil Mechanics and Foundations Division. ASCE* 95, 1531-1537.
- Hardin, B.O. and Drnevich, V.P. (1972). "Shear modulus and damping in soil: design equations and curves," *Journal of the Soil Mechanics and Foundations Division*, 98(7), 667-692.
- Hoyos, L.R., Suescún-Florez, E.A., and Puppala, A.J. (2015). "Stiffness of intermediate unsaturated soil from simultaneous suction-controlled resonant column and bender element testing." *Engineering Geology*, 188, 10-28.
- Ishihara, K., Tatsuoka, F., and Yasuda, S. (1975). "Undrained deformation and liquefaction of sand under cyclic stresses." *Soils and Foundations*, 15(1), 29-44.
- Ishihara, K. and Yoshimine, M. (1992). "Evaluation of settlements in sand deposits following liquefaction during earthquakes." *Soils and Foundations*, 32(1), 173-188.

- Ishihara, K. (2001). "Recent studies on liquefaction resistance of sand-effect of saturation." In 4th International Conference on Recent Advances in Geotechnical Earthquake Engineering and Soil Dynamics, San Diego. 1-7.
- Khalili, N., Habte, M.A., and Valliappan, S. (2005). "A bounding surface plasticity model for cyclic loading of granular soils." International Journal for Numerical Methods in Engineering. 63, 1939–1960.
- Khosravi, A., Ghayoomi, M., McCartney, J.S., and Ko, H.Y. (2010). "Impact of effective stress on the dynamic shear modulus of unsaturated sand." GeoFlorida 2010, 410-419.
- Khosravi, A. and McCartney, J.S. (2009). "Impact of stress state on the dynamic shear moduli of unsaturated, compacted soils." 4th Asia-Pacific Conf. on Unsat. Soils, Newcastle. 1-6.
- Khosravi, A. and McCartney, J.S. (2012). "Impact of hydraulic hysteresis on the small-strain shear modulus of unsaturated soils." J. of Geotech. and Geoenv. Eng., 138(11), 1326–1333.
- Kimoto, S., Oka, F., Fukutani, J., Yabuki, T., and Nakashima, K. (2011). "Monotonic and cyclic behavior of unsaturated sandy soil under drained and fully undrained conditions." Soils and Foundations, 51(4), 663-681.
- Konagai, K., Kiyota, T., Suyama, S., Asakura, T., Shibuya, K., and Eto, C. (2013). "Maps of soil subsidence for Tokyo bay shore areas liquefied in the March 11th, 2011 off the Pacific Coast of Tohoku Earthquake." Soil Dynamics and Earthquake Engineering, 53, 240-253.
- Lu, N. (2016). Generalized soil water retention equation for adsorption and capillarity. J. Geotech. Geoenviron. Eng., 1-15.
- Lu, N. (2020). Unsaturated soil mechanics: Fundamental challenges, breakthroughs, and opportunities. J. of Geotech. and Geoenv. Eng., 146(5), 1-9.
- Lu, N. and Likos, W.J. (2004). Unsaturated Soil Mechanics. Wiley and Sons. New York.
- Lu, N., Godt, J.W., and Wu, D.T. (2010). "A closed form equation for effective stress in unsaturated soil." Water Resources Research, 46(5), 55-65.
- Le, K.N. and Ghayoomi, M. (2017). "Cyclic direct simple shear test to measure strain-dependent dynamic properties of unsaturated sand." Geotechnical Testing Journal, 40(3), 381-395.
- Martin, G.R., Finn, W.L., and Seed, H.B. (1975). "Fundamentals of liquefaction under cyclic loading." J. of Geotech. and Geoenv. Eng., 101(5), 423-438.
- McCartney, J.S. and Parks, J. (2009). "Uncertainty in predicted hydraulic conductivity functions of unsaturated soils." Proc. 17th International Conference on Soil Mechanics and Geotechnical Engineering: The Academia and Practice of Geotechnical Engineering, Alexandria, Egypt, 5-9 October 2009, Volume 2, 1618-1621.
- Menq, F.Y. (2003). Dynamic properties of sandy and gravelly soils (Doctoral dissertation).

- Milatz, M. and Grabe, J. (2015). "A new simple shear apparatus and testing method for unsaturated sands." *Geotechnical Testing Journal*, 38(1), 9-22.
- Mele, L., Tian, J.T., Lirer, S., Flora, A., and Koseki, J. (2019). "Liquefaction resistance of unsaturated sands: experimental evidence and theoretical interpretation." *Géotechnique*, 69(6), 541-553.
- Naesgaard, E., (2011) "A hybrid effective stress-total stress procedure for analyzing soil embankment subjected to potential liquefaction and flooding" The University of British Columbia. 1-213.
- Naesgaard, E., and Byrne, P.M., (2005). "Flow liquefaction due to mixing of layered deposits", *Proc. of ICSMGE TC4 Satellite conf. on Recent Developments in Earthquake Engineering*, Osaka, Japan, Sept., pp. 103-108.
- Naesgaard, E., Byrne, P.M., Seid-Karbasi, M., and Park, S.S., (2005). "Modeling flow liquefaction, its mitigation, and comparison with centrifuge tests", *Proc. of ICSMGE TC4 Satellite conf. on Recent Developments in Earthquake Engineering*, Osaka, Japan, Sept. pp. 95-103.
- Naesgaard, E., Byrne, P.M., and Seid-Karbasi, (2006). "Modeling flow liquefaction and pore water redistribution mechanisms," *In Proc. of 8th U.S. National Conf. Earthquake Engineering*, EERI, San Francisco.
- Nuth, M. and Laloui, L. (2008). "Effective stress concept in unsaturated soils: Clarification and validation of a unified framework." *Int. J. for Num. and An. Meth. in Geo.*, 32(7), 771-801.
- Ng, C.W.W. and Xu, J. (2012). "Effects of current suction ratio and recent suction history on small-strain behavior of an unsaturated soil." *Canadian Geotechnical Journal*, 49(2), 226-243.
- Okamura, M. and Soga, Y. (2006). "Effects of pore fluid compressibility on liquefaction resistance of partially saturated sand." *Soils and Foundations*, 46(5), 695-700.
- Okamura, M. and Noguchi, K. (2009). "Liquefaction resistances of unsaturated non-plastic silt." *Soils and Foundations*, 49(2), 221-229.
- Oka, F., Kodaka, T., Suzuki, H., Kim, Y.S., Nishimatsu, N., and Kimoto, S. (2010). "Experimental study on the behavior of unsaturated compacted silt under triaxial compression." *Soils and Foundations*, 50(1), 27-44.
- Pasha, A.Y., Khoshghalb, A., and Khalili, N. (2015). "Pitfalls in interpretation of gravimetric water content-based soil-water characteristic curve for deformable porous media." *International Journal of Geomechanics*, 16(6), D4015004.
- Pasha, A.Y., Khoshghalb, A., and Khalili, N. (2019). "Can degree of saturation decrease during constant suction compression of an unsaturated soil?" *Comp. and Geotechnics*, 106, 199-204.

- Puebla, H., Byrne, P.M., and Phillips, R. (1997). "Analysis of CANLEX liquefaction embankments: prototype and centrifuge models." *Canadian Geotechnical Journal*, 34(5), 641-657.
- Rong, W. and McCartney, J.S. (2019). "Effect of suction on the drained seismic compression of unsaturated sand." In *E3S Web of Conferences*. EDP Sciences. Vol. 92, 08004.
- Rong, W. and McCartney, J.S. (2020a). "Drained seismic compression of unsaturated sand." *ASCE Journal of Geotechnical and Geoenvironmental Engineering*. 10.1061/(ASCE)GT.1943-5606.0002251.
- Rong, W. and McCartney, J.S. (2020b). "Undrained seismic compression of unsaturated sand." *ASCE Journal of Geotechnical and Geoenvironmental Engineering*. 10.1061/(ASCE)GT.1943-5606.0002420.
- Rong, W. and McCartney, J.S. (2020c). "Seismic compression of unsaturated sand under undrained conditions." In *Geo-Congress 2020: Geo-Systems, Sustainability, Geoenvironmental Engineering, and Unsaturated Soil Mechanics*. ASCE, Reston, VA. 299-308.
- Rong, W. and McCartney, J.S. (2021a). "Methodology to characterize the seismic compression of unsaturated sands under different drainage conditions." *ASTM Geotechnical Testing Journal*. 44(2), 440-461.
- Rong, W. and McCartney, J.S. (2021b). "Effect of relative density on the drained seismic compression of unsaturated backfills." *4th International Conference on Transportation Geotechnics*. Chicago, IL. May 24-27. pp. 277-288. DOI: 10.1007/978-3-030-77238-3_21.
- Rowe, P.W. 1962. The stress-dilatancy relation for static equilibrium of an assembly of particles in contact. *Proceedings of the Royal Society of London, Mathematical and Physical Sciences, Series A*, 269:500–527.
- Seed, H.B. and Idriss, I.M. (1971). "Simplified procedure for evaluating soil liquefaction potential." *Journal of Soil Mechanics and Foundations Div.* 97(9), 1249-1273.
- Seid-Karbasi M. and Byrne, P.M. (2006) "Seismic liquefaction, lateral spreading and flow slides: a numerical investigation into void redistribution. *Can. Geotech. J.* 44: (873-890)
- Seid-Karbasi M. and Byrne, P.M. (2007) "Effects of partial saturation on liquefiable ground response." *GeoCongress* (1-6)
- Sheng, D., and Zhou, A.N. (2011). "Coupling hydraulic with mechanical models for unsaturated soils." *Can. Geotech. J.* 48(5), 826-840.
- Silver, M.L. and Seed, H.B. (1971). "Deformation characteristics of sands under cyclic loading." *Journal of Soil Mechanics and Foundations Division*, 97(8), 1081-1098.

- Stewart, J.P., Chang, S.W., Bray, J.D., Seed, R.B., Sitar, N., and Riemer, M.F. (1995). "A report on geotechnical aspects of the January 17, 1994 Northridge earthquake." *Seismological Research Letters*, 66(3), 7-19.
- Stewart, J.P., Bray, J.D., McMahon, D.J., Smith, P.M., and Kropp, A.L. (2001). "Seismic performance of hillside fills." *J. of Geotech. and Geoenv. Eng.*, 127(11), 905-919.
- Stewart, J.P., Smith, P.M., Whang, D.H., and Bray, J.D. (2004). "Seismic compression of two compacted earth fills shaken by the 1994 Northridge earthquake." *J. of Geotech. and Geoenv. Eng.*, 130(5), 461-476.
- Stokoe, K. H., A. Kutulus, and F-Y. Menq (2004). "SASW measurements at the NEES Garner Valley test site, California." University of Texas at Austin, College of Engineering Data Report.
- Sawada, S., Tsukamoto, Y., and Ishihara, K. (2006). "Residual deformation characteristics of partially saturated sandy soils subjected to seismic excitation." *Soil Dynamics and Earthquake Engineering*, 26(2-4), 175-182.
- Tatsuoka, F. and Ishihara, K. (1974). "Drained deformation of sand under cyclic stresses reversing direction." *Soils and foundations*, 14(3), 51-65.
- Tatsuoka, F., Iwasaki, T., Yoshida, S., Fukushima, S., and Sudo, H. (1979). "Shear modulus and damping by drained tests on clean sand specimens reconstituted by various methods." *Soils and Foundations*, 19(1), 39-54.
- Tokimatsu, K. and Seed, H.B. (1987). "Evaluation of settlements in sands due to earthquake shaking." *Journal of Geotechnical Engineering*, 113(8), 861-878.
- Tsukamoto, Y., Ishihara, K., Nakazawa, H., Kamada, K., and Huang, Y. (2002). "Resistance of partly saturated sand to liquefaction with reference to longitudinal and shear wave velocities." *Soils and Foundations*, 42(6), 93-104.
- Unno, T., Kazama, M., Uzuoka, R., and Sento, N. (2008). "Liquefaction of unsaturated sand considering the pore air pressure and volume compressibility of the soil particle skeleton." *Soils and Foundations*, 48(1), 87-99.
- van Genuchten, M.T. (1980). "A closed-form equation for predicting the hydraulic conductivity of unsaturated soils." *Soil Science Society of America Journal*, 44(5), 892-898.
- Vucetic, M., Lanzo, G., and Doroudian, M. (1998). "Damping at small strains in cyclic simple shear test." *J. of Geotech. and Geoenv. Eng.*, 124(7), 585-594.
- Vucetic, M. and Mortezaie, A. (2015). "Cyclic secant shear modulus versus pore water pressure in sands at small cyclic strains." *Soil Dynamics and Earthquake Engineering*, 70, 60-72.

- Whang, D., Riemer, M.F., Bray, J.D., Stewart, J.P., and Smith, P.M. (2000). "Characterization of seismic compression of some compacted fills." In *Advances in Unsaturated Geotechnics*. 180-194.
- Whang, D.H., Stewart, J.P., and Bray, J.D. (2004). "Effect of compaction conditions on the seismic compression of compacted fill soils." *Geotechnical Testing Journal*, 27(4), 1-9.
- Whang, D.H., Moynour, M.S., Duku, P., and Stewart, J.P. (2005). "Seismic compression behavior of non-plastic silty sands." In *Advanced Experimental Unsaturated Soil Mechanics: Proceedings of the International Symposium on Advanced Experimental Unsaturated Soil Mechanics*. Eds. A. Tarantino, E. Romero, Y.J. Cui. CRC Press, Boca Raton. 257-263.
- Wheeler, S. J., Sharma, R. S., and Buisson, M. S. R. (2003). "Coupling of hysteresis and stress-strain behavior in unsaturated soil." *Geotechnique*, 53(1), 41-54.
- Youd, T.L. (1972). "Compaction of sands by repeated shear straining." *Journal of Soil Mechanics and Foundations Division*, 98(SM7), 709-725.
- Yee, E. and Stewart, J.P. (2011). *Nonlinear Site Response and Seismic Compression at Vertical Array Strongly Shaken by 2007 Niigata-ken Chuetsu-oki Earthquake*. Peer Report 2011/107.
- Yee, E., Stewart, J.P., and Tokimatsu, K. (2011). "Nonlinear site response and seismic compression at vertical array strongly shaken by 2007 Niigata-ken Chuetsu-oki Earthquake." Report PEER 2011/107. Pacific Earthquake Engineering Research Center. Berkeley, USA.
- Yee, E., Duku, P.M., and Stewart, J.P. (2014). "Cyclic volumetric strain behavior of sands with fines of low plasticity." *Journal of Geotechnical and Geoenvironmental Engineering*, 140(4), 04013042.
- Yoshimi, Y., Tanaka, K., and Tokimatsu, K. (1989). "Liquefaction resistance of a partially saturated sand." *Soils and Foundations*, 29(3), 157-162.
- Zheng, Y., Sander, A.C., Rong, W., Fox, P.J., Benson Shing, P., and McCartney, J.S. (2018). "Shaking table test of a half-scale geosynthetic-reinforced soil bridge abutment." *Geotechnical Testing Journal*, 41(1), 171-192.
- Zhou, C., and Ng, C.W.W. (2016). "Effects of temperature and suction on plastic deformation of unsaturated silt under cyclic loads." *Journal of Materials in Civil Engineering*, 28(12), 04016170.